

**Array Design for High-Resolution Beam Steering in Optical Phased  
Arrays Applications**

by

Ilyas Kandid

A thesis submitted to the Faculty of Graduate and Postdoctoral Affairs in  
partial fulfillment of the requirements for the degree of  
Master of Applied Science

Electrical and Computer Engineering

Carleton University

Ottawa, Ontario

© 2021, Ilyas Kandid

## Abstract

In Optical Phased Array (OPA) designs, there are often compromises between having a high beam resolution and a large steering range. Achieving an optimized result simultaneously is seldom found. The cause of this problem are the spacing constraints required for routing and element placements. A large element spacing in an array leads to the appearance of gratings lobes in the far field radiation pattern which are replicas of the main lobe formed by the periodicity of the array. Consequently, the main lobe is indistinguishable from the grating lobes which limits the performance of the OPA by restricting the steering range. New designs that break the periodicity of the array have shown to improve results by eliminating the grating lobes within the pattern. The main goal of this thesis is to investigate new array design methods which can enhance the resolution and steering range of the OPA.

The first array design we investigated was a planar sub-array design which undergoes a rotation method that rotates each sub-array, changing the location of the grating lobes. The second array design we investigated was a circular sub-array design which also undergoes rotation. We define the parameters that are responsible for the construction of each structure and study their effects on the sidelobe contrast and beamwidth performance. We also implemented an optimization procedure for further improvements. We were able to demonstrate an enlarged steering range with a narrow beam divergence using a large element spacing ( $5\lambda = 7.8 \mu m$ ) at  $\lambda = 1.55 \mu m$ .

## **Acknowledgments**

I would first like to extend my thanks and gratitude to my supervisor, Prof. Winnie Ye for the opportunity to work under her these past two years. I have learnt a tremendous number of things over this period and hope to continue learning with the same eagerness in the future.

Many thanks to each and every one in our research group for the aid you provided me regarding courses and my project. I would like to thank Fatin, Kevan and Sharhzad for the resources you've provided when I was initially starting my research. William and Xiaochen for the discussions we shared on our courses and studies. Vincent for the extensive assistance towards my project which I am extremely thankful for. And Ryan for the discussions around optimizations which were of big help for completing my project.

I would finally like to thank my family for their continuous support and kindness throughout my studies, especially during this time period.

# Table of Contents

## Contents

Abstract .....	ii
Acknowledgments.....	iii
Table of Contents .....	iv
List of Tables.....	vii
List of Figures .....	viii
List of Abbreviations .....	xiii
List of Symbols .....	xiii
Chapter 1 Introduction .....	1
<b>1.1</b> Silicon Photonics .....	1
<b>1.2</b> LiDAR and OPAs .....	1
<b>1.3</b> Thesis Objectives.....	3
Chapter 2 Literature Review.....	6
<b>2.1</b> Phased Array designs .....	6
<b>2.2</b> OPA designs .....	8
Chapter 3 Phased Array Theory.....	12
<b>3.1</b> Fundamental Parameters.....	12
<b>3.2</b> Array Geometries.....	14

<b>3.2.1</b> Linear Array .....	15
<b>3.2.2</b> Planar Array .....	19
<b>3.2.3</b> Circular Array .....	22
<b>Chapter 4</b> Planar Sub-Array Design .....	24
<b>4.1</b> Rectangular Planar Sub-Array .....	24
<b>4.1.1</b> Design Methodology.....	24
<b>4.1.2</b> Simulations .....	31
<b>4.2</b> Triangular Planar Sub-Array.....	40
<b>4.2.1</b> Design Methodology.....	40
<b>4.2.2</b> Simulations .....	41
<b>4.3</b> Uniform Rectangular Array and Rotated SA comparison .....	46
<b>4.4</b> Optimized Structure .....	49
<b>4.5</b> Summary .....	56
<b>Chapter 5</b> Circular Sub-Array Design .....	57
<b>5.1</b> Rectangular unit cell .....	57
<b>5.1.1</b> Design methodology .....	57
<b>5.1.2</b> Simulations .....	60
<b>5.1.3</b> Optimizations using the Genetic Algorithm .....	70
<b>5.2</b> Circular unit cell .....	75

<b>5.2.1</b> Design methodology .....	75
<b>5.2.2</b> Simulations .....	76
<b>5.2.3</b> Optimizations using the Genetic Algorithm .....	91
<b>5.3</b> Optimized structures .....	95
<b>5.3.1</b> Rectangular unit cell & Circular SA.....	95
<b>5.3.2</b> Circular unit cell & Circular SA.....	97
<b>5.4</b> Uniform Circular Array and Circular SA comparison.....	99
<b>5.5</b> Summary .....	102
Chapter 6 Conclusions and Future Works .....	103
<b>6.1</b> Future Work .....	104
References.....	106

## List of Tables

Table 4. 1: Measured SL contrast and BW for varying angles of $\theta_0$ (Rectangular SA lattice) .....	47
Table 4. 2: Comparisons with State-of-the-Art OPA Steering Ranges .....	48
Table 5. 1: Measured SL contrast and BW for varying angles of $\theta_0$ (Rectangular unit cell) .....	96
Table 5. 2: Measured SL contrast and BW for varying angles of $\theta_0$ (Circular unit cell) .....	99
Table 5. 3: SL contrast and BW performance for circular unit cell and circular SA designs.....	101

## List of Figures

Figure 2.1: Planar array with both rectangular and triangular shaped SAs. Implementation of small SA displacements [29].....	8
Figure 2. 2: Schematic of the OPA design. Reprinted from [6].....	9
Figure 2. 3: Illustration of the device structure with 5 channels for clarity. Reprinted from [33].....	10
Figure 2. 4: Illustration of both 4x4 uniform array and a 7x7 sparse. Reprinted from [36].....	11
Figure 3. 1: Coordinate system used for defining radiation patterns. Reprinted with permission from [37].....	13
Figure 3. 2: 2D pattern cut highlighting key points of a radiation pattern. Reprinted with permission from [37].....	14
Figure 3. 3: Linear array structure .....	15
Figure 3. 4: Array factor plotted for $N = 3, 5, 7$ .....	17
Figure 3. 5: AF with GLs due to spacing $d = \frac{3}{2}\lambda$ .....	18
Figure 3. 6: AF demonstrated beam steering .....	19
Figure 3. 7: Rectangular planar array .....	20
Figure 3. 8: Triangular grid.....	21
Figure 3. 9: Circular array geometry.....	22
Figure 4. 1: 4x4 rectangular and triangular lattice unit cells .....	24
Figure 4. 2: 4x4 rectangular unit cell lattice organized into a 2x2 rectangular SA lattice .....	25
Figure 4. 3: Rectangular SA pattern.....	26
Figure 4. 4: GLs are introduced at $\theta = \pm 90^\circ$ due to element spacing.....	27
Figure 4. 5: SA pattern with many GLs due to the large spacing .....	27

Figure 4. 6: Illustration of Eq. (4.4).....	28
Figure 4. 7: Unit cell, SA, and Final pattern.....	29
Figure 4. 8: SA structure after rotation where $\alpha = 10^\circ$ .....	30
Figure 4. 9: GL rotation due to lattice rotation.....	31
Figure 4. 10: Impact of $N_r$ on the SL contrast and BW.....	33
Figure 4. 11: Impact of $N_c$ on the SL contrast and BW.....	33
Figure 4. 12: Array Structure for $N_r = 1$ and 20 @ $D_x$ and $D_y = 35 \mu m$ .....	34
Figure 4. 13: Impact of $N_{SA_r}$ on the SL contrast and BW.....	35
Figure 4. 14: Impact of $N_{SA_c}$ on the SL contrast and BW.....	35
Figure 4. 15: Impact of $d_x$ and $d_y$ on the SL contrast and BW.....	36
Figure 4. 16: Array structure for $d_x = 1 * \frac{2}{3} \lambda$ and $d_x = 8 * \frac{2}{3} \lambda$ .....	36
Figure 4. 17: Impact of $D_x$ and $D_y$ on the SL contrast and BW.....	37
Figure 4. 18: Impact of $\alpha$ on SL contrast.....	37
Figure 4. 19: Equivalent GL locations between a rectangular unit cell with rotation angle $\alpha = 0^\circ$ and $90^\circ$ .....	38
Figure 4. 20: Equivalent GL locations between a triangular unit cell with rotation angle $\alpha = 0^\circ$ and $60^\circ$ .....	39
Figure 4. 21: 3x3 triangular SA lattice with 4x4 triangular unit cells.....	40
Figure 4. 22: Impact of $N_r$ on the SL contrast and BW (Triangular SA).....	42
Figure 4. 23: Impact of $N_c$ on the SL contrast and BW (Triangular SA).....	42
Figure 4. 24: Impact of $N_{SA_r}$ on the SL contrast and BW (Triangular SA).....	42
Figure 4. 25: Impact of $N_{SA_c}$ on the SL contrast and BW (Triangular SA).....	43
Figure 4. 26: Impact of $d_x$ and $d_y$ on the SL contrast and BW (Triangular SA).....	43
Figure 4. 27: Impact of $D_x$ and $D_y$ on the SL contrast and BW (Triangular SA).....	44
Figure 4. 28: Impact of $\alpha$ on SL contrast (Triangular SA).....	44
Figure 4. 29: Radiation pattern plotted in $uv$ space for a Rectangular SA.....	45
Figure 4. 30: Radiation pattern plotted in $uv$ space for a Triangular SA.....	45
Figure 4. 31: 16x16 URA with pattern cut demonstrating GLs.....	46

Figure 4. 32: Rotated rectangular SA with corresponding pattern cut.....	46
Figure 4. 33: 2D pattern cuts for $\theta_0 = 15^\circ, 30^\circ, 45^\circ, 60^\circ, \text{ and } 80^\circ$ (Rectangular SA) .....	48
Figure 4. 34: Theta cut for the rotated rectangular SA structure. There are always two SL peaks near the ML. ....	49
Figure 4. 35: GA process .....	50
Figure 4. 36: Non-optimized structure with pattern cut.....	51
Figure 4. 37: GA run for 100 and 200 generations respectively (Rectangular SA).....	52
Figure 4. 38: Non-optimized and optimized pattern cuts (Rectangular SA) .....	53
Figure 4. 39: GA run for 100 and 200 generations respectively (Rectangular SA).....	54
Figure 4. 40: Non-optimized and optimized pattern cuts (Triangular SA).....	55
Figure 5. 1: 4x4 rectangular unit cell lattice .....	57
Figure 5. 2: A circular SA design consisting of $N_r = 4, N_c = 4, M_{SA} = 8 \text{ and } N_{SA} = 2$ .....	58
Figure 5. 3: A circular SA design using rotation method #1 .....	59
Figure 5. 4: A circular SA design using rotation method #2.....	59
Figure 5. 5: Impact of $N_r$ on the SL contrast and BW .....	61
Figure 5. 6: Impact of $N_c$ on the SL contrast and BW .....	61
Figure 5. 7: Array Structure for $N_r = 1 \text{ and } 20 @ R_{SA} = 75 \mu\text{m} \text{ and } dr_{SA} = 60 \mu\text{m}$ .....	62
Figure 5. 8: Impact of $N_{SA}$ on the SL contrast and BW for $M_{SA} = 9$ .....	63
Figure 5. 9: Impact of $N_{SA}$ on the SL contrast and BW for $M_{SA} = 15$ .....	63
Figure 5. 10: Impact of $M_{SA}$ on the SL contrast and BW.....	64
Figure 5. 11: Impact of $d_x \text{ and } d_y$ on the SL contrast and BW .....	64
Figure 5. 12: Array structure for $R_{SA} = 110 \mu\text{m} \text{ and } dr_{SA} = 90 \mu\text{m}$ when $d_x = 1 * \frac{2}{3} \lambda$ ( $1.79 \mu\text{m}$ ) and $d_x = 8 * \frac{2}{3} \lambda$ ( $14.36 \mu\text{m}$ ) .....	65
Figure 5. 13: Impact of $R_{SA}$ on the SL contrast and BW .....	65

Figure 5. 14: Larger SA spacing due to the increased ring radius, $R_{SA}$ .....	66
Figure 5. 15: Impact of $dr_{SA}$ on the SL contrast and BW .....	66
Figure 5. 16: Impact of $dr$ on a single circular unit cell.....	67
Figure 5. 17: Radiation pattern when $\alpha = 0^\circ$ and $10^\circ$ respectively .....	67
Figure 5. 18: Impact of $\alpha$ on SL contrast.....	68
Figure 5. 19: 2D UV pattern for Rot #1 and #2 respectively for $N_r = 15$ .....	69
Figure 5. 20: Array structure for Rot #1 and #2 respectively for $N_r = 15$ .....	69
Figure 5. 21: 2D UV pattern for Rot #2 when $N_r = 15$ and $N_c = 15$ respectively ...	70
Figure 5. 22: Array structure $N_r = 15$ and $N_c = 15$ respectively .....	70
Figure 5. 23: Generation plot for Run 1 .....	72
Figure 5. 24: Generation plot for 100 generations and 200 generations.....	73
Figure 5. 25: Generation plot for the 1000 element threshold.....	74
Figure 5. 26: Generation plot for 200 generations (1000 element threshold).....	75
Figure 5. 27: Circular unit cell lattice with $M = 9, N = 3$ .....	75
Figure 5. 28: Circular SA lattice with $M = 9, N = 3, M_{SA} = 7$ and $N_{SA} = 3$ .....	76
Figure 5. 29: Impact of $M$ on the SL contrast and BW .....	77
Figure 5. 30: Pattern cut for $M = 5$ .....	78
Figure 5. 31: Pattern cut for $M = 7$ .....	78
Figure 5. 32: Impact of $N$ on the SL contrast and BW .....	79
Figure 5. 33: Impact of $M_{SA}$ on the SL contrast and BW.....	80
Figure 5. 34: Impact of $N_{SA}$ on the SL contrast and BW for $M_{SA} = 7$ .....	80
Figure 5. 35: Impact of $N_{SA}$ on the SL contrast and BW for $M_{SA} = 15$ .....	81
Figure 5. 36: Impact of $R_{unit}$ on the SL contrast and BW.....	81
Figure 5. 37: Impact of $dr_{unit}$ on the SL contrast and BW .....	82
Figure 5. 38: Impact of $R_{SA}$ on the SL contrast and BW .....	82
Figure 5. 39: Impact of $dr_{SA}$ on the SL contrast and BW .....	83
Figure 5. 40: Impact of $\alpha$ on the SL contrast .....	84
Figure 5. 41: Impact of $\alpha$ and $N$ on the SL contrast where $N = 1, 2$ and $3$ .....	85
Figure 5. 42: Identical orientations with $\alpha = 0^\circ$ and $72^\circ$ .....	86

Figure 5. 43: Pattern cuts for $N = 3 @ \alpha = 0^\circ$ .....	86
Figure 5. 44: Pattern cuts for $N = 3 @ \alpha = 10^\circ$ .....	87
Figure 5. 45: Pattern cuts for $N = 3 @ \alpha = 30^\circ$ .....	87
Figure 5. 46: Pattern cuts for $R_{SA} = 35 \mu m$ .....	88
Figure 5. 47: Pattern cuts for $R_{SA} = 65 \mu m$ .....	89
Figure 5. 48: Impact of $R$ on SL contrast for a single ring array .....	90
Figure 5. 49: Generation plot for Run 1 .....	92
Figure 5. 50: Second GA run with 100 generations .....	93
Figure 5. 51: 1000 element threshold with 50 generations .....	94
Figure 5. 52: 1000 element threshold with 100 generations and 50 independent runs	94
Figure 5. 53: 3D radiation pattern plotted in $uv$ space (Rectangular unit cell) .....	95
Figure 5. 54: 2D pattern cuts for $\theta_0 = 0^\circ, 30^\circ, 60^\circ$ and $80^\circ$ (Rectangular unit cell).	96
Figure 5. 55: 3D radiation pattern plotted in $uv$ space (Rectangular unit cell) .....	97
Figure 5. 56: 2D pattern cuts for $\theta_0 = 0^\circ, 30^\circ, 60^\circ$ and $80^\circ$ (Circular unit cell) .....	98
Figure 5. 57: Circular unit and Circular SA with respective pattern cut.....	100
Figure 5. 58: Pattern cut at $\theta_0 = 30^\circ$ for circular unit cell and circular SA respectively .....	101

## List of Abbreviations

**OPA:** Optical Phased Array

**LIDAR:** Light Detection and Ranging

**SiP:** Silicon Photonics

**ML:** Main Lobe

**GL:** Grating Lobe

**SL:** Side Lobe

**BW:** Beamwidth

**FOV:** Field-of-view

**SA:** Sub-array

**URA:** Uniform Rectangular Array

**GA:** Genetic Algorithm

## List of Symbols

$k$ : Wavenumber

$\lambda$ : Wavelength

$d$ : Spacing

$\phi$ : Phi Angle

$\theta$ : Theta Angle

$\psi$ : Psi Angle

$\vec{E}$ : Electric field vector

$AF$ : Array Factor

$I_n$ : Excitation amplitude

$EF$ : Element factor

$\beta_n$ : Progressive phase between each element

$N_r$ : Number of rows

$N_c$ : Number of columns

$N_{SA_r}$ : Number of sub-array rows

$N_{SA_c}$ : Number of sub-array columns

$D_x$ : Sub-array spacing along x

$D_y$ : Sub-array spacing along y

$\alpha$ : Rotation angle for unit cells

$M$ : Number of elements per ring

$N$ : Number of rings

$M_{SA}$ : Number of unit cells in each ring

$N_{SA}$ : Number of sub-array rings

$R$ : Radius

$dr$ : Incremental radius

# Chapter 1 Introduction

## 1.1 Silicon Photonics

Due to the inherent limitations of silicon's molecular structure, many thought that silicon is an ineffective element for photonic applications due to its poor light detection and amplification properties. Most photonic functions rely heavily on III-V materials like indium phosphide (InP) or gallium arsenide (GaAs). However, advances in time and research have transformed this notion around silicon for photonics, particularly from the rise in silicon photonics (SiP). There are a few reasons for this turn around; One reason for this is that silicon is transparent to wavelengths commonly used for optical transport ( $1.3 \mu\text{m}$  to  $1.6 \mu\text{m}$ ). However, the most important reason is that silicon is widely used in electronics for the design of integrated circuits; by leveraging the existing complementary metal-oxide semiconductor (CMOS) foundries to create photonic integrated circuits (PICs), inexpensive and smaller optical devices can be fabricated, which has opened new possibilities in photonic design [1]. In addition, the large index contrast shared between silicon and silicon dioxide allows for high light confinement, making the device footprint ultracompact and ideal for dense integration. The top layer of silicon can be etched and doped to create different active and passive devices ranging from waveguides, power splitters/combiners, optical modulators and grating couplers [2].

Many applications have been demonstrated using SiP including data transmission, biomedical sensors, signal processing in telecommunication, and renewable energy [3-5]. One important application that has made use of SiP recently are optical phased arrays (OPAs), which is largely attributed to the rising need for a cheaper Light Detection and Ranging (LiDAR) system. The first introduction of SiP in OPAs was demonstrated in 2009 [6] and over the past decade, many new OPA designs would go on to use SiP to meet the future goal of building a single-chip OPA system.

## 1.2 LiDAR and OPAs

LiDAR is a ranging technology that uses light for high resolution image sensing. LiDAR works by transmitting light which is then reflected off objects in the area of illumination; once the light returns to the transmitter, a detailed reconstruction of the area can be made. There are a lot of similarities between LiDAR and its radio wave counterpart, RADAR but the higher optical frequency allows LiDAR to generate

images of higher resolution. The main application of LiDAR involves 3D sensing, which is commonly used in remote sensing applications to capture the information on a landscape like the height of vegetation or the density of land [7]. More recent applications like robotics and autonomous vehicles have already made use of LiDAR systems for their high-resolution capabilities [8]. These traditional LiDAR systems rely on using mechanical parts to scan the beam of light. Using mechanical rotation limits the scan speeds and increases the overall size of the system; these glaring issues let alone the huge costs make their wide deployment onto the commercial market very difficult [9].

Even with the significant advances made in LiDAR systems, it is widely understood that new solutions for LiDAR must be made for it to be a practical device for autonomous vehicles. In addition to providing autonomy to cars, inexpensive LiDARs will benefit numerous other applications like drones used for 3D mapping, high-risk monitoring where deploying a human isn't feasible and search-rescue missions [10]. A fast-growing platform for LiDAR design involves PICs which has the promise to be a viable pathway to making LiDAR affordable. The elimination of moving parts by developing on a PIC would drastically reduce the size of the system, bringing down costs of each piece. One heavily researched topic is Optical Phased Arrays (OPAs) which is seen as a viable option for precise beam steering without using any moving parts.

OPAs are the optical sibling of the more commonly known phased arrays developed in the past for radio and microwave range frequencies. The general principle of a phased array is to control the radiation patterns shape and direction by manipulating the relative amplitudes and phases of each element within the array. Through this process, points of interference will change, resulting in different beam shapes and locations. Phased arrays were originally designed for military applications, particularly for target detection but slowly over time, the technology has transitioned into many different applications like weather detection or air-traffic control [11]. One notable technology used today, 5G communication, is heavily dependent on phased arrays for high-speed communication.

One of the first OPA designs dates to 1972 where one-dimensional beam steering was demonstrated using a lithium tantalite crystal to modulate the phase of light [12]. A plethora of research followed through in investigating electro-optic beam

steering in waveguides [13-15]. It was reported that many of these designs were overly optimistic, citing common difficulties such as maintaining low power consumptions with a high bandwidth or poor light coupling [16]. Moreover, these designs are passive arrays, so they are incapable of generating arbitrary patterns. Over time, most research on OPAs have been using the SOI platform due to the large advancements made in SiP which have enabled large-scale integration designs at lower costs.

The first introduction of OPAs with SiP occurred in 2009, where a 1D OPA is fabricated on SOI and demonstrated off-chip beam steering using the thermo-optic effect and wavelength tuning [6]. Many common procedures and methods used within this paper are reflected in future works by different authors; the phase-steering methods used, the use of long gratings as antennas and the organization of optical components to direct light have all been utilized. The two main system requirements that most designs strive to improve are the resolution and steering range. These two design metrics are always at the forefront of most designs as they are what will constitute if a design can ensure high-resolution beam scanning [17]. This is also the main goal of this thesis where the application of array design in OPA applications will be studied to improve the resolution and scanning capabilities for OPAs.

### 1.3 Thesis Objectives

The design of phased arrays in the optical domain have posed constraints that have made it difficult for designers to fulfill the performance expectations for an efficient LiDAR OPA. Many OPA designs have either demonstrated a large steering range or high-resolutions but not simultaneously [18]. Generally, the most important parameters of phased array are the number of elements and the spacing between elements. These two parameters effect numerous properties related to the radiation pattern such as the steering range, beamwidth, sidelobe (SL) contrast, etc. One important requirement tied to the spacing is the  $\lambda/2$  requirement. If the spacing,  $d$  becomes larger than  $\lambda/2$ , aliasing occur which replicates our main signal at other angles. This occurs due to the periodicity of the array. Aliasing is commonly referred to as grating lobes (GLs) which are lobes of similar intensity to the main lobe (ML). This means that the ML is indistinguishable from the GLs, limiting the systems performance. This design constraint poses less difficult for 1D OPAs as the long narrow grating elements can be grouped closer together [15]. However, 1D phased arrays cannot steer in both directions so different means of controlling the upwards refraction of light is necessary. One

common method is to utilize wavelength steering but this requires a tunable laser, increasing the complexity and cost. Eventually, 2D OPAs were designed to demonstrate 2D beam steering by only controlling the phases of each element within the array. But more challenges arise in 2D design due to the array size and spacing. A large area is required for optical routing and the antenna size is usually much larger than the optical wavelength. There are also cross-talk considerations that limit the ability to have compact spacing. All these requirements inevitably introduce GLs which is why so many 2D designs have only demonstrated very limited field-of-views (FOV).

The goal of this thesis is to study array design methods that have not been applied to the design of OPAs. Implementing these designs would help overcome the strict design requirements that many 2D OPAs face when trying to balance the compactness of the device and the available steering range within the FOV.

Chapter 2 will consist of a literature review, divided into two main sections. The first section is composed of conventional phased array design works from the past, mainly focusing on non-uniform array structures. The second section focuses more on OPA designs within the previous decade, looking at the different array configurations and performance results achieved by a collection of groups.

Chapter 3 will review the basics of phased array theory, where background is given into the fundamental parameters of an antenna array, such as the main lobe, sidelobes, beamwidth, etc. The array geometries that will be studied within most of the thesis will be introduced and their respective array factor equations are derived. The array geometry is a key factor in the design of phased arrays because the element placements is largely responsible for affecting the radiation pattern of the array. The three main geometries that are highlighted in the chapter are linear, planar, and circular arrays. The formulation of each array factor will demonstrate the key differences that each array possesses.

Both Chapter 4 and 5 cover the study behind the sub-array design for OPA applications. The beginning of both chapters presents an overview of the proposed design, specifying the structural parameters and formulation of each array geometry. Chapter 4 is geared specifically to planar sub-arrays (rectangular and triangular lattices) while Chapter 5 is catered towards the circular sub-array design. After the design methodology, the simulation process is detailed and explained where each respective

structures design parameters are studied to understand the effect that they have on the fundamental parameters explained in Chapter 3.

The last chapter, Chapter 6, presents a summary of the results and includes a dialogue on future advancements that can be made to the design.

## Chapter 2 Literature Review

Over the past decade, numerous array designs utilizing SiP have been proposed for OPAs. However, most designs still leverage common design methods that have been extensively studied around the 1950s and onwards when early research in conventional phased arrays was beginning [19]. For this reason, we divide this chapter into two main parts. The first part will discuss array design methods studied for radio frequency/mm-wave phased arrays. The second part will cover array designs used in OPAs, particularly non-uniform methods.

### 2.1 Phased Array designs

Most array design methods involve manipulating the design parameters of the structure in unorthodox manners to achieve a desired result whether that outcome would be lower SLs, an increased steering range, or a narrower BW. Conventional phased array designs consisted of utilizing basic structures such as linear arrays where the element spacing, and excitation amplitudes are all uniform. However, there are many undesirable properties inherent to these uniform structures when the spacing,  $d > \lambda/2$ , which results in GLs. This issue has inspired many works over the decades to find new solutions for this problem. One area of research involving nonuniformly spaced arrays has seen a plethora of work published. The interest was largely created to make cost savings by reducing the number of elements while achieving similar performance to standard uniform arrays. Furthermore, the steering range can be increased to be larger than possible, even with an array of spacing  $d > \lambda/2$ . Non-uniform phased arrays were first studied in 1960 by Unz [20] where a linear array with arbitrarily distributed elements is designed. A general mathematical formulation is demonstrated between the element distribution and the far field pattern. Other works have followed this paper discussing non-uniform arrangements [21-23]. The main objectives of these papers were to demonstrate that with a fewer number of elements, a comparable BW to a uniform arrangement can be achieved. Also, it is commonly shown that GLs can be eliminated and replaced with SLs of unequal amplitudes that are smaller than the ML [21].

Follow up work that kept the same design philosophy of utilizing non-uniform arrangements but through different methods. One work involved perturbing the inter-element spacings (i.e., making the spacing nonuniform between each element) but

keeping the same overall structure intact. More unconventional designs later followed which still incorporated the same goal in eliminating the GLs. One area of interest was the use of sub-arrays (SAs) and rotations to reduce the strength of GLs in the far field. This was first shown in 1978 by Agrawal [24] where a procedure to lower the GL power of a uniform planar array is explained. The uniform planar array is divided into 4 SAs where each SA is rotated by a specified angle with respect to each other. The purpose of the rotation is to align each GL on a point of lower radiation power which will constructively interfere, lowering the overall GL power. Many papers have followed suit in using SAs in different forms for GL suppression [25-27] by either making translation shifts or rotations with different shapes and sizes of SAs.

One work by Krivosheev et.al [28] demonstrated a comprehensive study of several GL suppression methods using SAs. These methods include using a relative shift between adjacent SAs, using gaps between each SA, using different inter-element spacings within in each SA, using rotation of SAs, and incorporating all methods at once. The methods studied achieved a GL suppression ranging from -2.6 dB to -11 dB. The best performing method utilized SA rotation to lower the GL levels. Incorporating small SA displacements was found to improve performance but only by a small amount. One advantage of using rotation is that the SAs periodicity is kept intact, so large scale implementations are easier to fabricate in comparison to other suppression methods that add great complexity to the array design. These other methods usually rely on randomizing the element location to find a favorable result, but this results in additional difficulties in fabricating their designs.

A further work by the same group [29] advances their prior work by extending the concept of SA manipulation for GL suppression. More examples are considered using the prior methods like with both rectangular and triangular grids. Previously, only SAs of identical shapes and sizes were considered. Now, different SA shapes and orientations are studied simultaneously, like arrays that have SAs shaped like rectangles and triangles as shown in Fig. 2.1. Other factors like amplitude tapering or using different element radiation patterns are considered. The array performance under scanning is studied at the end of the report. One example involved a rectangular grid array with uniform SAs that has an element spacing of  $d = 20\lambda$  which achieved a GL level of -19.3 dB and a SLL of -16.6 dB at broadside.

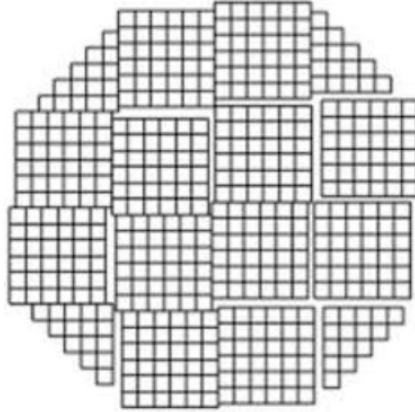


**Figure 2.1: Planar array with both rectangular and triangular shaped SAs. Implementation of small SA displacements [29]**

## 2.2 OPA designs

The first phased array approach for optical beam steering by Acoleyen et.al [6], utilized a 1x16 linear array where 16 grating couplers are spaced at a distance of  $d = 2 \mu m$ . Many concepts within the design were replicated in future OPA designs like the use of long gratings as antennas or the phase shifting schemes used like thermos-optic and wavelength steering. The advantage of long grating antennas is that they can leverage wavelength tuning to steer light on the principal of the grating equation while the other direction can be steered by using the phased array principal. However, this requires a tunable laser which adds great cost and complexity. The design demonstrated a steering of  $2.3^\circ$  and  $14.1^\circ$  along  $\phi$  and  $\theta$  respectively, using thermos-optic steering and wavelength steering respectively. The definitions of  $\phi$  and  $\theta$  are shown in Fig. 2.2.

Following [6], Acoleyen et.al in [30] demonstrated the first 2D OPA on SOI with a 4x4 passive array with  $60 \mu m$  spacing. The design can steer  $0.24^\circ/nm$  but the spacing between GL and ML is only  $1.5^\circ$ . The design didn't demonstrate full 2D beam steering but still provided an introduction into 2D OPA designs. A large-scale 2D OPA design was demonstrated by Sun et.al [31] where both active and passive phased arrays were shown. Two passive arrays with 32x32 and 64x64 were designed to perform complex pattern generation while an 8x8 active array was able to generate various radiation patterns as the phase was changed. A thermo-optic phase shifter is used where the heater is directly attached to the waveguide through doping. The direct integration

of the heater improves the efficiency of the heater to achieve a thermo-optic efficiency of 8.5 mW per  $\pi$  phase shift.

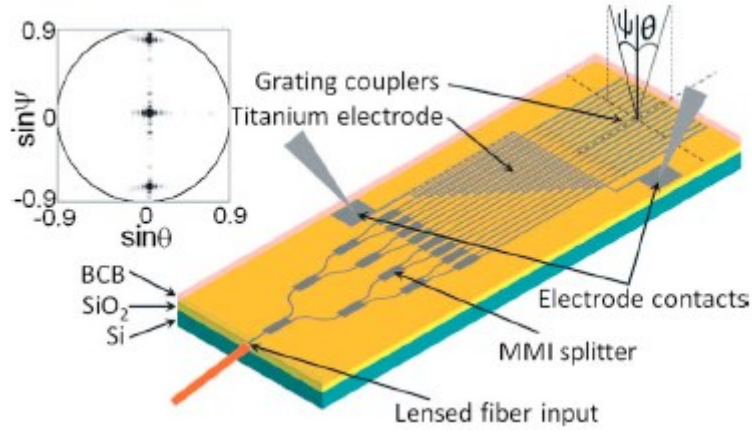


**Figure 2. 2: Schematic of the OPA design. Reprinted from [6]**

To not have strong coupling between adjacent waveguides and a large steering range, non-uniform arrangements for OPAs are explored. The first demonstration of a non-uniform array design for OPA applications was done by Kwong et.al [32]. Most OPA designs prior to this work utilized uniform spacings which severely limits the steering range. The design by Kwong consists of three uniform SAs that have non-overlapping GLs by adjusting the inter-element spacing of each SA. Each SA contains 4 elements where the spacing is equal to  $2\lambda$ ,  $2.5\lambda$ , and  $3.5\lambda$  ( $@ \lambda = 1.5 \mu m$ ) respectively, giving a total array length of  $46.5 \mu m$ . A large array size is desirable since it results in a narrower beam profile, giving higher resolutions. To modulate the phase, thermal phase shifting is used. Each element in the array has an independent phase modulator, giving more control for beam steering. The design reported a steering range of  $31.9^\circ$  along  $\phi$ .

Later works on non-uniform array design followed. One was shown in 2016 by Hutchinson et.al [33] where a large scale implementation using a non-uniform emitter spacing is shown. The design of the OPA can be seen in Fig. 2.3. The main objective of this work is to demonstrate an OPA that can perform high resolution beam steering with little to no aliasing. Most prior designs before this paper's publication have not demonstrated a design with both a large steering range and a narrow BW. Most works were often limited by the effects of aliasing due to the large emitter spacing required. One design demonstrated the widest steering range of  $51^\circ$  but with a relatively poor BW of  $3.3^\circ$  [34]. Another design achieved the smallest BW of  $0.3^\circ$  but the steering

range was very small at  $0.9^\circ$  [35]. To improve on both the steering range and BW, the design by Hutchinson made use of several design choices. Aliasing is reduced by breaking the periodicity of the emitter spacing; thus, the light will no longer exhibit constructive interference at certain angles of  $\psi$ , increasing the total steering range but at the cost of higher SLs. The BW is minimized by ensuring the total length of the emitters is elongated along the beam steering axis; this is achieved by splitting the light into 128 channels. The OPA in [33] achieved a wide steering range of  $80^\circ$  and a BW of  $0.14^\circ$  along  $\psi$ .

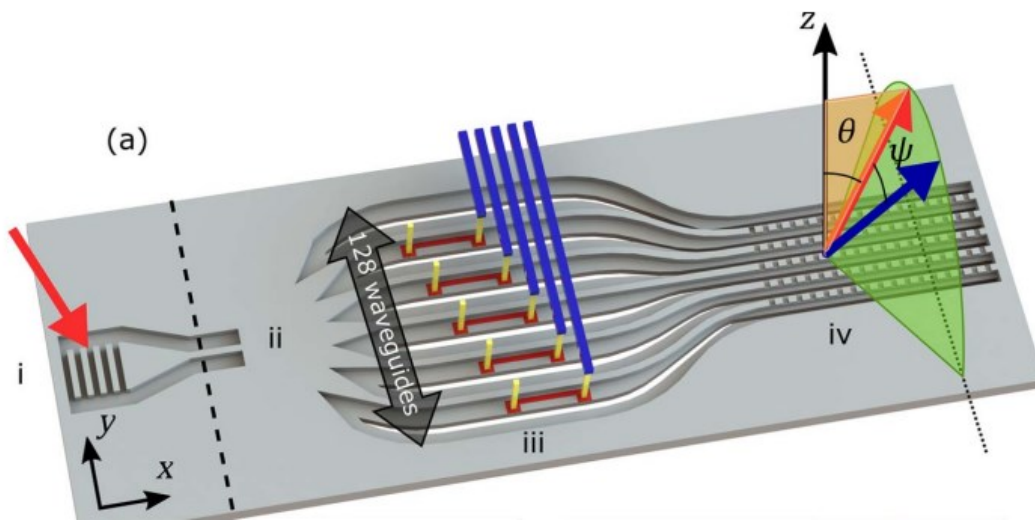


**Figure 2. 3: Illustration of the device structure with 5 channels for clarity.**  
**Reprinted from [33]**

Another form of non-uniform array design involves the use of eliminating elements from the total array, thus changing the periodicity of the element spacing. These arrays are commonly referred to as sparse arrays. The first 2D sparse OPA was demonstrated in 2019 by Fatemi et.al [36]. One promising aspect of a sparse array is that it can alleviate the routing issues encountered in many OPA designs that limit their large-scale implementation. The design also implements a compact nano-antenna with a footprint of  $2 \mu\text{m} \times 5 \mu\text{m}$ . Most OPA designs have used conventional long gratings as emitters, but this is not feasible for large designs due to the footprint required by long gratings. This raises a need for implementing a more compact nano-antenna when designing a 2D OPA. The structure can be seen in Fig. 2.3 where the design of a sparse array is contrasted with a uniform array. The sparse array demonstrates more flexibility for routing. Due to increased choice in selection for element removal, there are many

possibilities in achieving a desired optimum result for keeping the side lobe level and BW below a required threshold. The sparse array is optimized by using a genetic algorithm to find the best element locations for specified requirements. These requirements include the feasibility of the design network (i.e., is there enough space between elements and components), the average SLL and the BW of each array. The design in [36] reported that the best design solution consisted of 128 elements which achieved a steering range of  $16^\circ$  with a BW of  $0.8^\circ$  along  $\theta$ , which was the highest reported GL free field of view -to- BW ratio for an OPA.

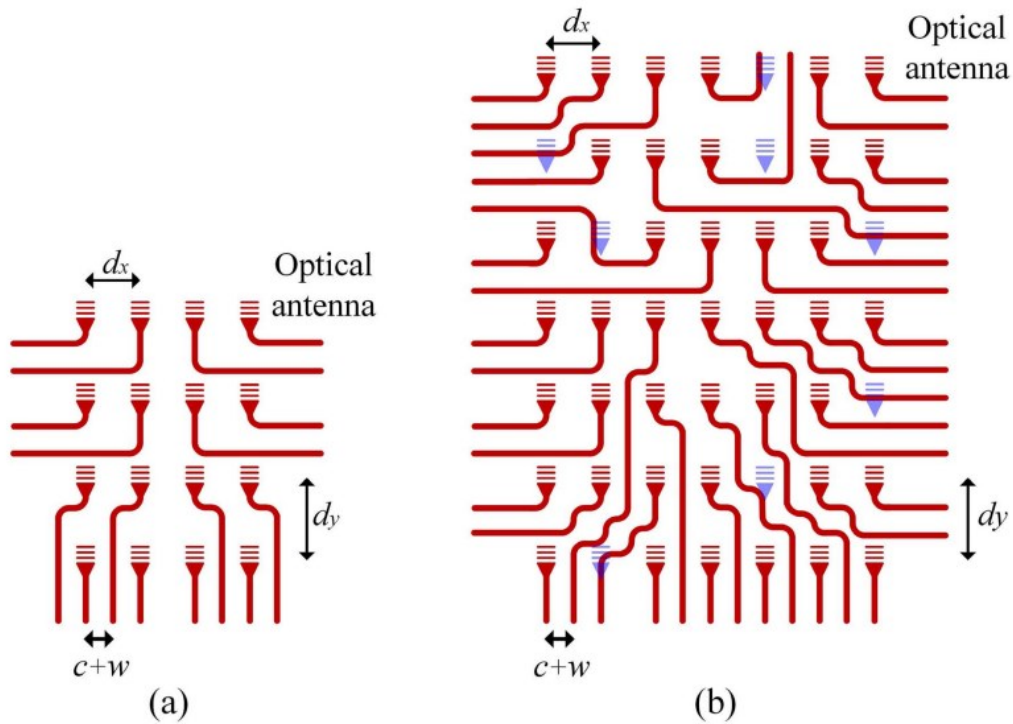


**Figure 2. 4: Illustration of both 4x4 uniform array and a 7x7 sparse. Reprinted from [36]**

## Chapter 3 Phased Array Theory

### 3.1 Fundamental Parameters

The power an antenna can radiate or receive is dependent on many design parameters, ranging from the antenna's size, configuration (horn, dipole, or dish antenna), and the elements arrangement. Arranging antenna elements into different geometries can yield new far field radiation patterns, giving designers flexibility to change and improve system performance. Designers make use of the new design variables which include

- Array geometry
- Element spacing
- Element excitation amplitude and phase

One of the most defining features to describe an antennas performance is by describing the radiation pattern. The radiation pattern is defined as the angular plot of the radiation of an antenna [37]. By altering the design of a phased array, it is possible to significantly alter the radiation pattern in numerous ways.

The most distinct parts seen in the radiation pattern are referred to as the lobes, which can be classified into either the main lobe (ML) or side lobes (SLs). Radiation lobes are regions of the pattern that are surrounded by relatively weak areas of intensity. Fig. 3.1 demonstrates not only the coordinate system that is used in antenna analysis, but it also illustrates a three-dimensional representation typically radiated by an antenna element. Here theta ( $\theta$ ) represents the angle span starting from the z-axis into the direction of the x-y plane while phi ( $\phi$ ) represents the angle span starting from the x-axis towards the direction of the y-axis. The ML (or major lobe in Fig. 3.1) is defined to point along the z axis @  $\theta = 0^\circ$  while lobes that are not pointing in the direction of interest are denoted as SLs. There are more specific classifications like grating lobes (GLs) which will be touched upon later in the chapter which arise when the element spacing is too large.

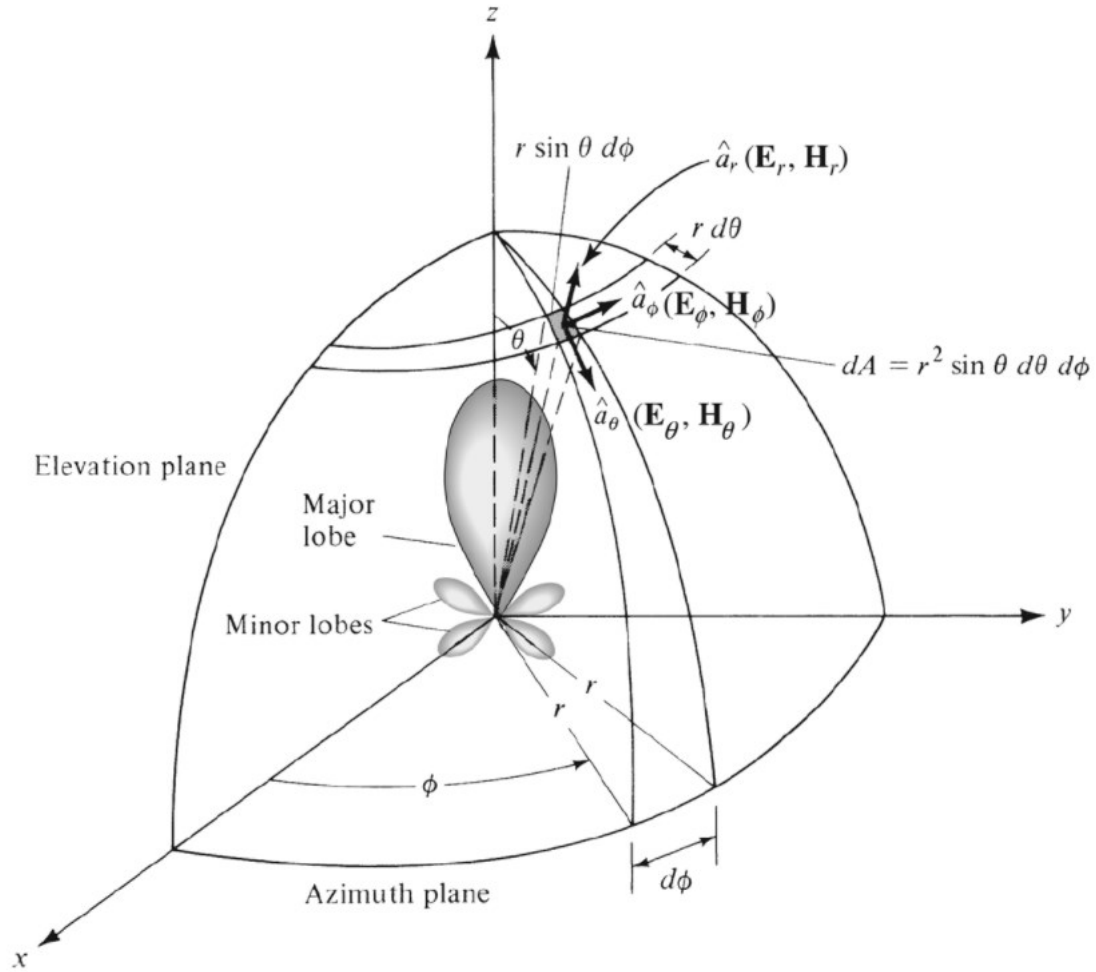


**Figure 3. 1: Coordinate system used for defining radiation patterns. Reprinted with permission from [37]**

Typically, the radiation pattern is discussed in terms of the normalized electric field,  $|E|$  or the normalized power,  $|E|^2$ . The field patterns can be expressed in linear or dB scale, but the latter is more common for the extra details provided about the radiation pattern. We can see in Fig. 3.2, the two-dimensional cut of the radiation pattern which gives a more thorough picture of the pattern characteristics. The most common points extracted from a field pattern in dB are the half-power points where the magnitude of the radiation pattern decreases by 50%, and the highest SLs, which are the SLs closest to 0 dB. The half-power beamwidth (HPBW) is the angular separation where the radiation pattern is equal to  $-3\text{ dB}$  from the peak of the main beam. Similarly, the FNBW is the angular separation between the nulls of the ML. The SL contrast will be defined as the range between the peak of the ML and the highest SL within the radiation pattern. The SL contrast is always considered a magnitude. We will refer to the HPBW as just the BW throughout Ch.4 and Ch.5.

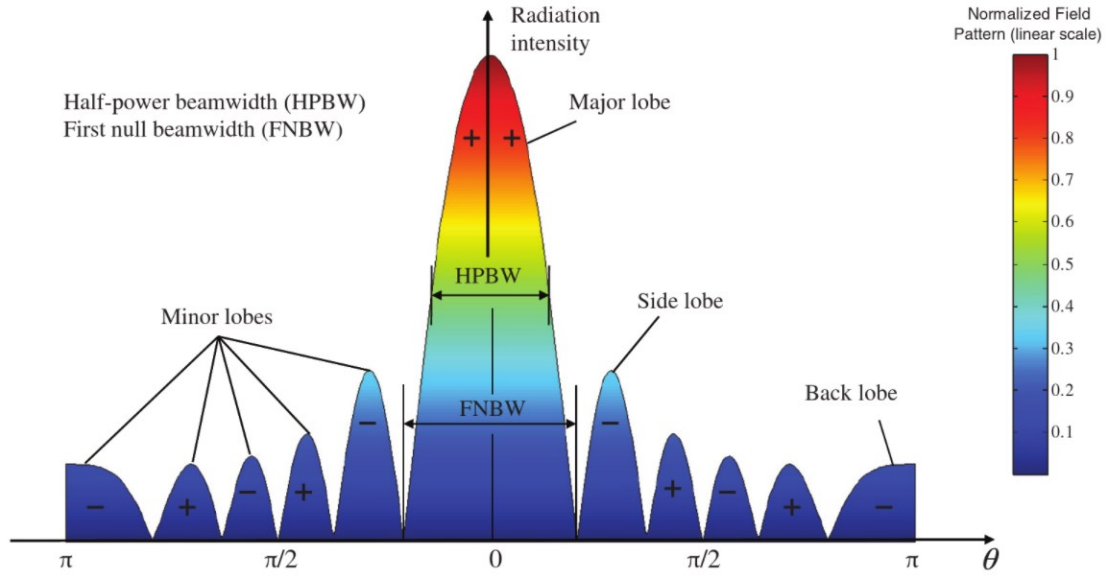


**Figure 3. 2: 2D pattern cut highlighting key points of a radiation pattern.**

Reprinted with permission from [37]

### 3.2 Array Geometries

One of the most important parts of an antenna array is its geometrical configuration. The array geometry is largely responsible for controlling the radiation pattern; a change in the array geometry can dramatically change the patterns shape. The SL contrast and BW can undergo significant changes with small changes to the element spacing or count. Within this section, three main geometries will be introduced which will be used throughout the thesis.

The main defining function of an antenna array geometry is known as the array factor (AF). The array factor represents the complex value far-field radiation pattern of an array of isotropic radiating elements. The AF is dependent on many different factors including the number of elements, their geometrical arrangement, the excitation amplitudes, the excitation phases, and the element spacing. A general formulation of the AF is [37],

$$AF(\hat{r}) = \sum_{n=1}^N I_n e^{jk\hat{r} \cdot \vec{r}_n} \quad (3.1)$$

where  $I_n$  represents the excitation amplitude,  $k$  is the wavevector ( $k = \frac{2\pi}{\lambda}$ ),  $\vec{r}_n$  represents the coordinates of each element and  $\hat{r}$  is the direction unit vector.

The important distinction to make is that the AF is only a function of the geometry of the array and the excitation phase while the total radiation pattern emitted by the array is the product of the field of a single radiating element, denoted as the element factor (EF) and the AF [37]. That is

$$\text{Total pattern} = EF \times AF \quad (3.2)$$

### 3.2.1 Linear Array

A linear array is composed of antenna elements aligned along a single axis as seen in Fig 3.3. The main parameters defining a linear array is the element count  $N$  and the spacing,  $d$ .

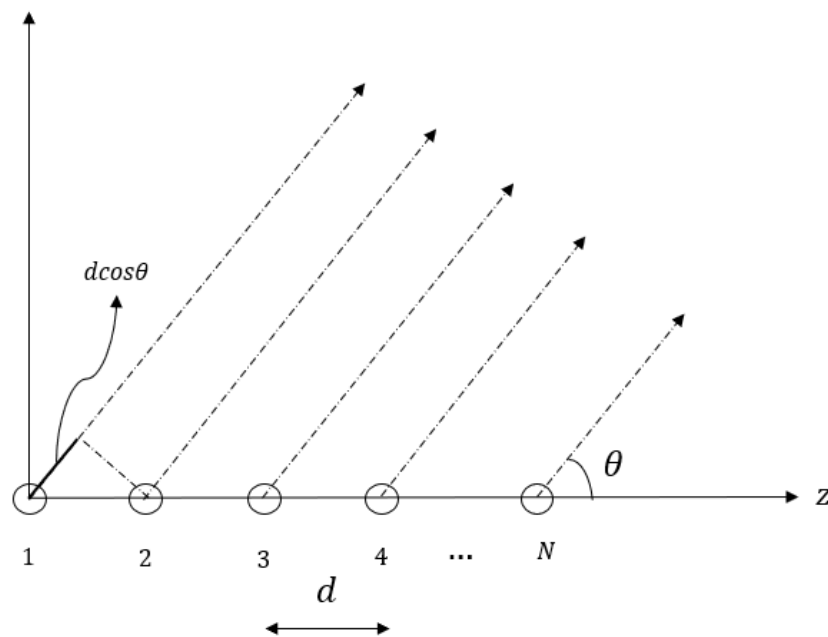


**Figure 3. 3: Linear array structure**

If each element has an excitation amplitude of 1, the summation of all elements can be written as

$$AF = e^{j\epsilon_1} + e^{j\epsilon_2} + e^{j\epsilon_3} + \dots + e^{j\epsilon_N} \quad (3.3)$$

where  $\epsilon_n$  represents the phases of the received signal at each element location from  $n = 1, 2, 3, \dots, N$

When a signal is being received at an angle of  $\theta$ , the phase difference between each element is  $dcos\theta$ . By setting the reference of the array at the origin, the AF can now be written as

$$AF = \sum_{n=1}^N e^{j(n-1)kdcos\theta} = 1 + e^{jkdcos\theta} + e^{j2kdcos\theta} + \dots + e^{jNkdcos\theta} \quad (3.4)$$

One addition to be made to the AF is the inclusion of a progressive phase onto each subsequent element. We will let  $\beta$  represent the progressive phase so each succeeding element will have a phase greater than the preceding element by a factor of  $\beta$ . The AF can now be given by

$$AF = \sum_{n=1}^N e^{j(n-1)(kdcos\theta + \beta)} = \sum_{n=1}^N e^{j(n-1)\varphi} \quad (3.5)$$

$$\varphi = kdcos\theta + \beta \quad (3.5a)$$

$$\beta = -kdcos\theta_0 \quad (3.5b)$$

$\theta_0$  represents the scan angle where the ML is directed to. To understand what the radiation pattern looks like for this AF and to understand the effects of the arguments, some manipulation to Eq (3.5) is necessary [38]. With some changes to Eq (3.5), we get

$$AF = e^{\frac{j\varphi}{2}(N-1)} \frac{\sin(N\frac{\varphi}{2})}{\sin(\frac{\varphi}{2})} \quad (3.6)$$

The maximum of the array factor will occur when  $\varphi = 0$  and the normalized array factor will be:

$$AF_{norm} = \frac{\sin(N\frac{\varphi}{2})}{N\sin(\frac{\varphi}{2})} \quad (3.7)$$

Now it is easier to identify how changing the arguments within the AF change the overall radiation pattern. In Fig. 3.4, we can see the effect of changing the element count for  $N = 3, 5, \text{ and } 7$ . The BW of the ML shrinks and the SL contrast increases as  $N$  increases.

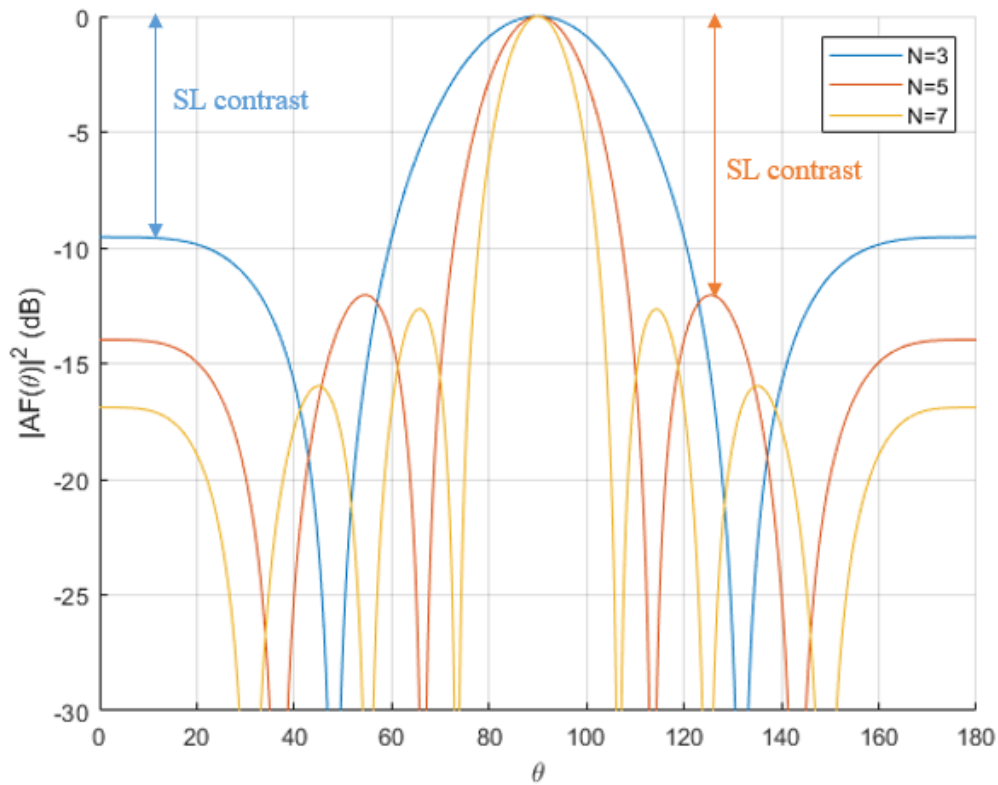


**Figure 3. 4: Array factor plotted for  $N = 3, 5, 7$**

The element spacing chosen for Fig 3.4 was  $d = \frac{\lambda}{2}$ . The significance of this deals with the problem of GLs. GLs are lobes of identical intensity to the ML which limits the capabilities of the array. Due to the periodic nature of the array configuration, element spacings with  $d > \frac{\lambda}{2}$  will slowly introduce GLs in the visible region. Fig. 3.5 demonstrates the inclusion of GLs for a linear array with  $d = \frac{3}{2}\lambda$  and  $N = 5$ . We can also see that the steering range is the angular separation between the ML and adjacent GLs within the pattern.

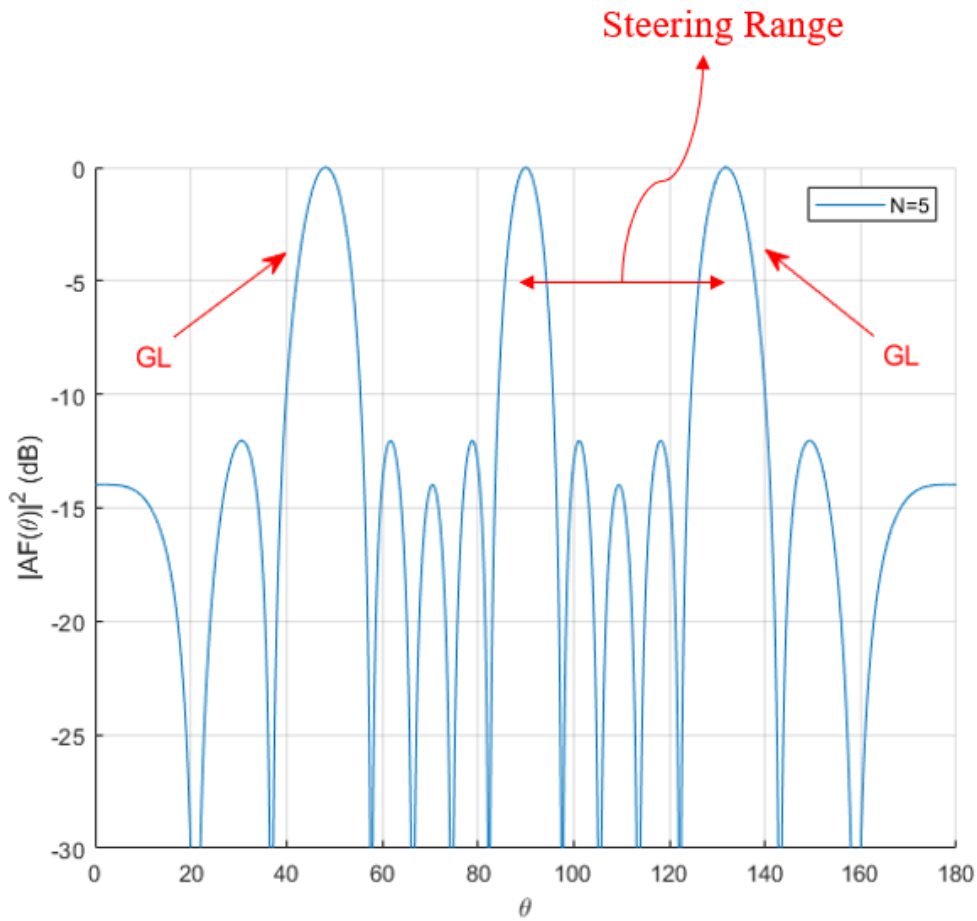


**Figure 3. 5: AF with GLs due to spacing  $d = \frac{3}{2}\lambda$**

Finally, the effect of changing the progressive phase  $\beta$  is demonstrated in Fig. 3.6. We know from Eq. (3.7), that the maximum depends on  $\varphi/2 = (kdcos\theta + \beta)/2$ .

Therefore, by changing  $\beta$ ,  $\varphi$  will change, thus creating a new location where the ML will form. We can also see that this changes the whole radiation pattern as the directions where the SLs were pointing also change.

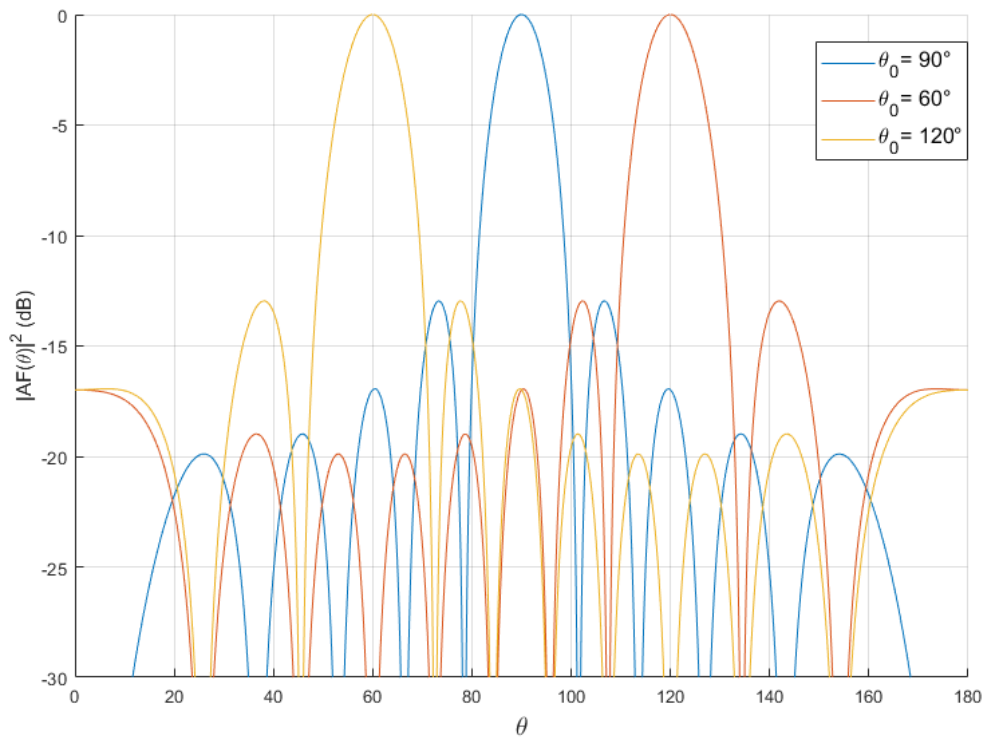


**Figure 3. 6: AF demonstrated beam steering**

### 3.2.2 Planar Array

The re-construction of a linear array to two dimensions can form a planar array. Planar arrays provide additional variables which can be used to manipulate the radiation pattern of the array. Planar arrays allow for beam steering in both  $\theta$  and  $\phi$  directions, which is not possible with a conventional linear array. The two most common planar arrays are rectangular and triangular arrays, seen in Fig. 3.7 and Fig. 3.8.

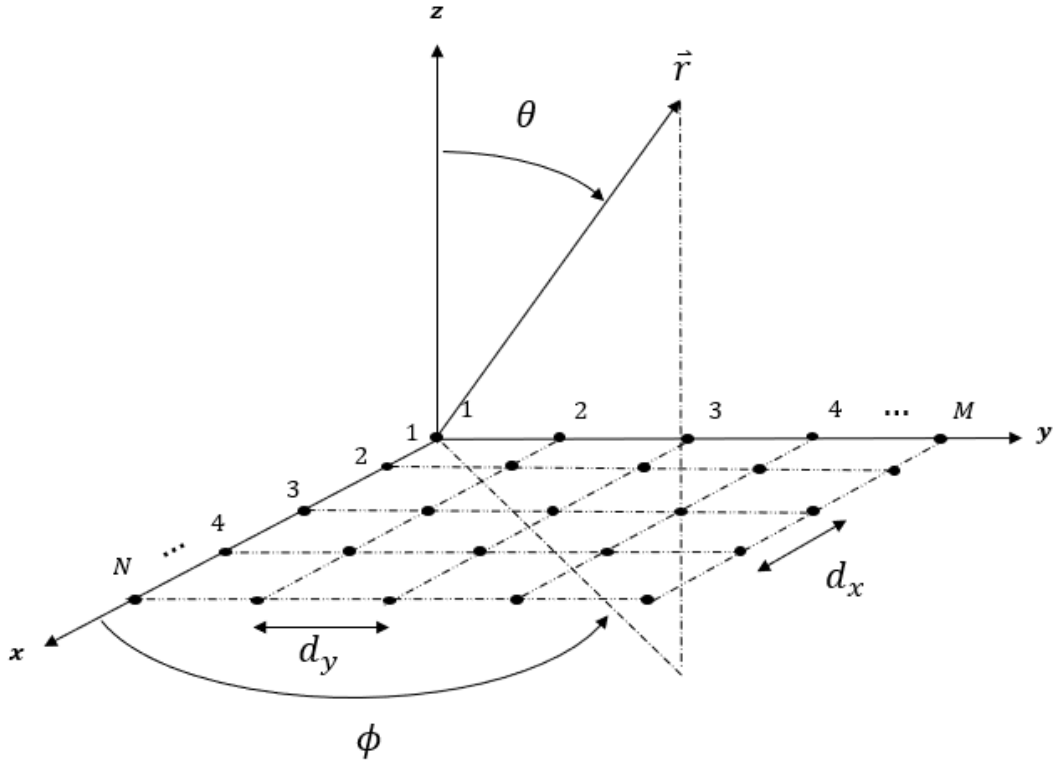


**Figure 3. 7: Rectangular planar array**

The AF of a rectangular planar array can be obtained by using the same formulation for the linear AF [37]. A linear array located along the x-axis has the following AF

$$AF_x = \sum_{n=1}^N I_n e^{j(n-1)(kd_x \sin\theta \cos\phi + \beta_x)} \quad (3.8)$$

Where new subscripts are attached to  $d_x$  and  $\beta_x$  to represent the x-axis elements.

Similarly, the AF of a linear array along the y-axis is defined as

$$AF_y = \sum_{m=1}^M I_m e^{j(m-1)(kd_y \sin\theta \sin\phi + \beta_y)} \quad (3.9)$$

Now the AF for the planar array located in the x-y plane can be written as

$$AF = \sum_{n=1}^N I_n e^{j(n-1)(kd_x \sin\theta \cos\phi + \beta_x)} \sum_{m=1}^M I_m e^{j(m-1)(kd_y \sin\theta \sin\phi + \beta_y)} \quad (3.10)$$

$$\beta_x = -kd_x \sin\theta_0 \cos\phi_0 \quad (3.10a)$$

$$\beta_y = -kd_y \sin\theta_0 \sin\phi_0 \quad (3.10b)$$

or

$$AF = (AF_x)(AF_y) \quad (3.11)$$

Eq (3.11) shows us that the AF for a rectangular array is equivalent to the product of the two AF along each axis. And similarly with Eq. (3.5), we have our phase terms  $\beta_x$  and  $\beta_y$ , each with the respective scan angles  $\theta_0$  and  $\phi_0$ .

The triangular phased array has been demonstrated in numerous works [39-41] to achieve the same scan limits as a rectangular phased array but with fewer elements. The AF of a triangular planar array can be found in a similar fashion to its rectangular counterpart. The triangular lattice is composed of two rectangular lattices, where one of the lattices is displaced by a distance of  $d_x/2$  and  $d_y/2$  as shown in Fig. 3.6. Each lattice has elements spaced at a distance of  $d_x$  and  $d_y$  respectively. The AF can be expressed as [42]

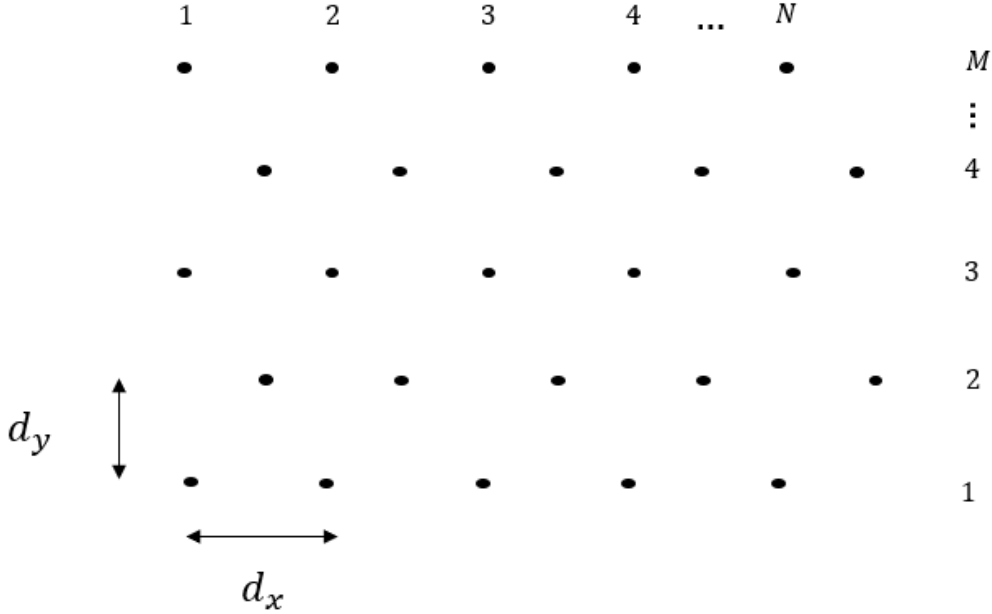


**Figure 3. 8: Triangular grid**

$$AF = \sum_{n=1}^N e^{j(n-1)kd_x(u-u_0)} \sum_{m=1}^M e^{j(m-1)kd_y(v-v_0)} + e^{jkd_x/2(u-u_0)} \cdot e^{jkd_y/2(v-v_0)} \sum_{n=1}^N e^{j(n-1)kd_x(u-u_0)} \sum_{m=1}^M e^{j(m-1)kd_y(v-v_0)} \quad (3.12)$$

$$AF = \left[ 1 + e^{jk\frac{d_x}{2}(u-u_0)} \cdot e^{jk\frac{d_y}{2}(v-v_0)} \right] \cdot \sum_{n=1}^N e^{jnk d_x(u-u_0)} \sum_{m=1}^M e^{jmk d_y(v-v_0)} \quad (3.13)$$

$$u = \sin \theta \cos \phi, v = \sin \theta \sin \phi, u_0 = \sin \theta_0 \cos \phi_0 \text{ and } v_0 = \sin \theta_0 \sin \phi_0 \quad (3.13a)$$

### 3.2.3 Circular Array

Circular arrays have been extensively studied in the past [43-45]. When full  $360^\circ$  scanning is desired without distorting the shape of the radiation pattern, circular arrays are the most appropriate choice compared to other phased arrays that struggle with distortion when scanning.

A circular array consists of  $M$  elements placed along the circumference of a circle with radius  $R$  as seen in Fig 3.9. The angle between elements is uniform and can be represented by

$$\phi = \frac{2\pi}{M} \quad (3.14)$$

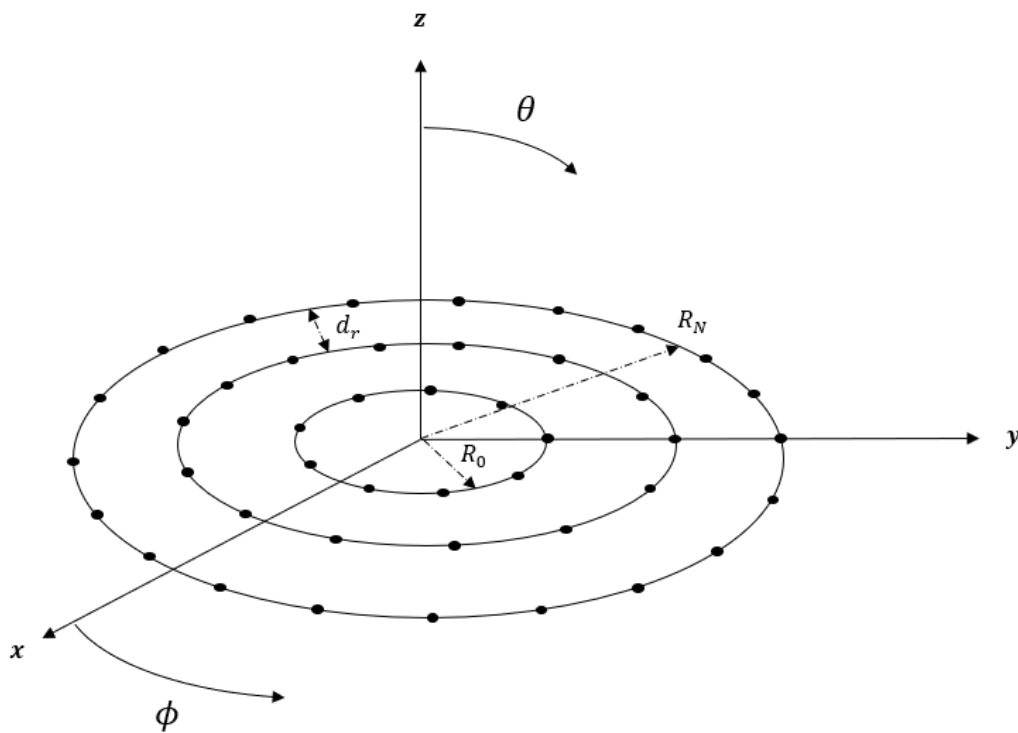


**Figure 3. 9: Circular array geometry**

We can define the  $n$ th position vector as [37]

$$\vec{r}_n = R \cos \phi_m \hat{x} + R \sin \phi_m \hat{y} \quad (3.15)$$

where  $\phi_m = \frac{2\pi}{M} m$ . Now, the AF can be defined as [37]

$$AF(\theta, \phi) = \sum_{m=1}^M I_m e^{jkR(\cos \phi_m \sin \theta \cos \phi + \sin \phi_m \sin \theta \sin \phi)} \quad (3.16)$$

Eq. (3.16) can be reduced to

$$AF(\theta, \phi) = \sum_{m=1}^M I_m e^{jkR(\sin\theta \cos(\phi - \phi_m) + \beta_m)} \quad (3.17)$$

where  $\beta_m = -\sin\theta_0 \cos(\phi_0 - \phi_m)$  and  $\theta_0$  and  $\phi_0$  is the theta and phi scan angles respectively.

To define the AF for concentric ring array, some additions must be included to the definition of the structure to account more rings. We will introduce the parameter  $N$ , the number of circular rings,  $R_0$ , the radius of the first center ring and  $dr$ , the incremental radius between each ring. Now, the radius can be represented as

$$R_n = R_0 + (N - 1)dr \quad (3.18)$$

The AF can now be expressed as

$$AF(\theta, \phi) = \sum_{m=1}^M \sum_{n=1}^N I_{mn} e^{jksin\theta \cos(\phi - \frac{2\pi(m-1)}{M})R_n} \quad (3.19)$$

Similarly, to the transformation made for the linear AF from Eq. (3.5) to (3.6), we can alter Eq. (3.17) to better understand the effect of each parameter belonging to the circular array. It has been shown in many past studies and discussions about circular arrays that the AF can be re-written in the following format if the excitation amplitudes are uniform [46].

$$AF(\theta, \phi) = MI_0 \sum_{n=-\infty}^{+\infty} J_{nM}(kR) e^{jnM(\pi/2 - \xi)} \quad (2.18)$$

where  $\xi = \tan^{-1}(\frac{v-v_0}{u-u_0})$  and  $u, u_0, v$ , and  $v_0$  are similarly defined in Eq. 3.13. Since the

Fourier transform of a circular symmetric function is also circular symmetric, we can represent the circular AF using Bessel functions. Eq. (3.18) demonstrates that the AF is dependent on the Bessel function  $J_{nM}$  which contains the argument  $kR$ . When  $M$  is large enough, the AF can be simplified to be only expressed using the principal term ( $n = 0$ ) [49, 50].

$$AF(\theta, \phi) = MJ_0(kR) \quad (3.19)$$

## Chapter 4 Planar Sub-Array Design

The content of this chapter comprises of the analysis of two planar array designs, one composed of a rectangular planar array and one triangular planar array. A SA design is used for each array style which will be detailed in the beginning of each array section. For each selected SA lattice, we will study the performance for both the rectangular and triangular unit cells simultaneously. Simulation results are obtained using MATLAB to calculate the SL contrast and BW which will be used to study the performance of each array.

### 4.1 Rectangular Planar Sub-Array

#### 4.1.1 Design Methodology

Both rectangular and triangular planar arrays are selected as the unit cell lattice as pictured in Fig. 4.1. The design parameters used to define the structure consists of the element spacing ( $d_x$  and  $d_y$ ) and the number of rows/columns ( $N_r$  and  $N_c$ ).

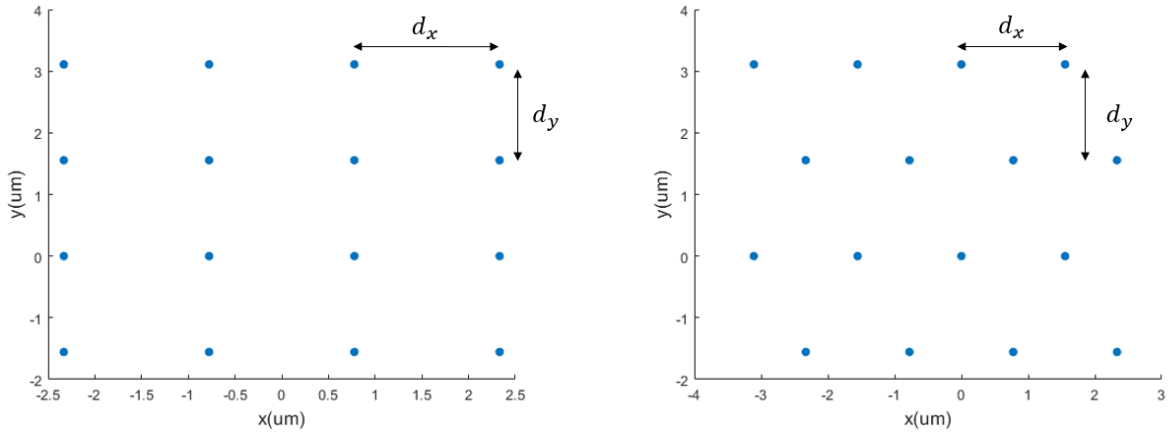


**Figure 4. 1: 4x4 rectangular and triangular lattice unit cells**

We now consider creating the rectangular SA structure. We introduce additional design parameters to define the SA structure including the number of SA rows/columns,  $N_{SA_r}$  and  $N_{SA_c}$ , the SA row/column spacing,  $D_x$  and  $D_y$ , which are defined from the center of each SA, and the rotation angle  $\alpha$ . To ensure no unit cells overlap,  $D_x$  and  $D_y$  must scale with any changes to the unit cell parameters. We introduce a new parameter,  $D_l$ , which represents the diagonal length of each unit cell.  $D_l$  is defined as

$$D_l = \sqrt{\Delta X^2 + \Delta Y^2} \quad (4.1)$$

where  $\Delta X$  and  $\Delta Y$  represent the unit cell length along  $x$  and  $y$  respectively. Now using Eq. (4.1),  $D_x$  and  $D_y$  can be defined as

$$D_x = D_I + d_x \text{ and } D_y = D_I + d_y \quad (4.2)$$

Once the structural parameters pertaining to the SA are defined, the structure can be created as pictured in Fig. 4.2. We can see that the structure consists of a unit cell with  $N_r$  and  $N_c = 4$  and a rectangular SA with  $N_{SA_r}$  and  $N_{SA_c} = 2$ .

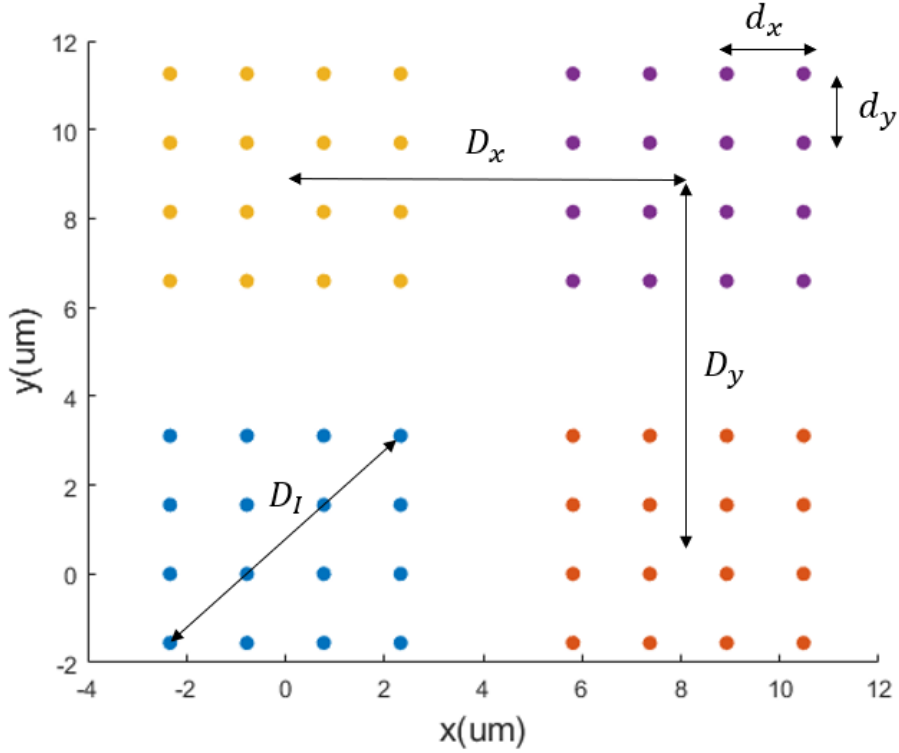


**Figure 4. 2: 4x4 rectangular unit cell lattice organized into a 2x2 rectangular SA lattice**

The pattern corresponding to a rectangular SA lattice is visualized in Fig. 4.3. To understand the formation of this pattern, we make use of Eq. (3.2) which stated that the final pattern is constructed by taking the product of the EF and AF. However, when using SAs, the final array pattern has an additional argument which is the SA AF. We can understand this with the following formulation:

$$Final \ Array \ Pattern = EF * AF_{unit} * AF_{SA} \quad (4.3)$$

where  $EF$  is the element factor described in Eq. (3.2) and  $AF_{unit}$  and  $AF_{SA}$  represent

the AFs of the unit cell and SA respectively.

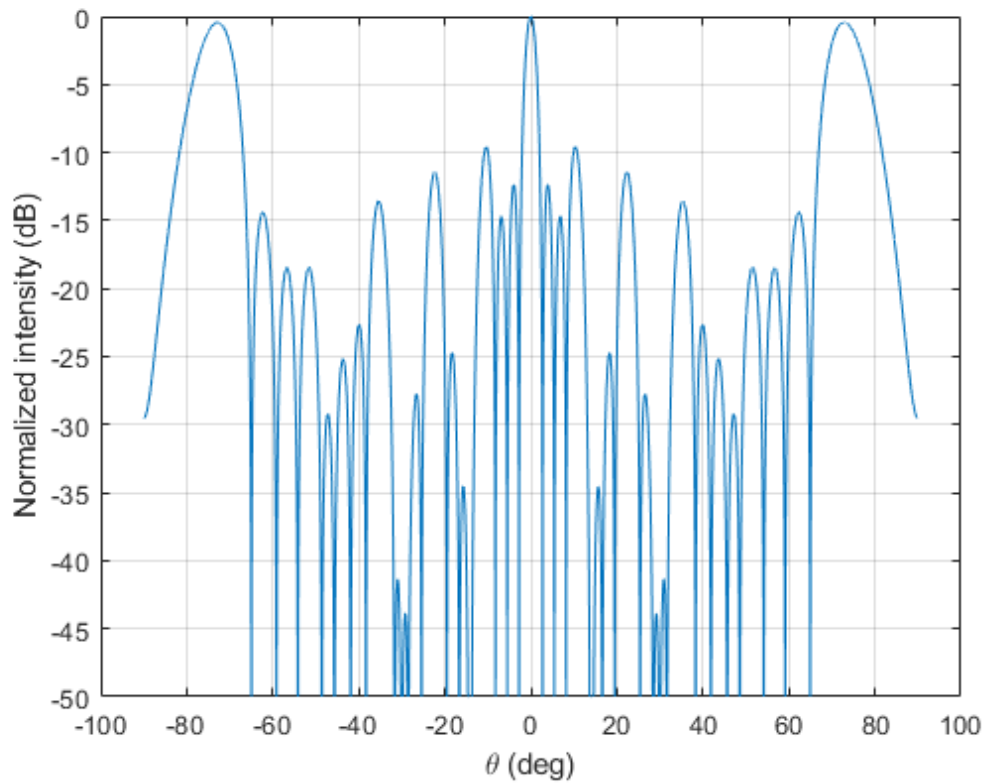


**Figure 4. 3: Rectangular SA pattern**

Here we consider the use of an isotropic antenna, which results in the  $EF = 1$ . Therefore, we only need to consider the latter two factors in Eq. (4.3). We can illustrate the formation of the final array pattern by using a rectangular unit cell with a rectangular SA geometry. The unit cell has a spacing of  $d_x = d_y = 1 * \lambda$  which introduces GLs at  $\theta = \pm 90^\circ$  as seen in in Fig. 4.4.

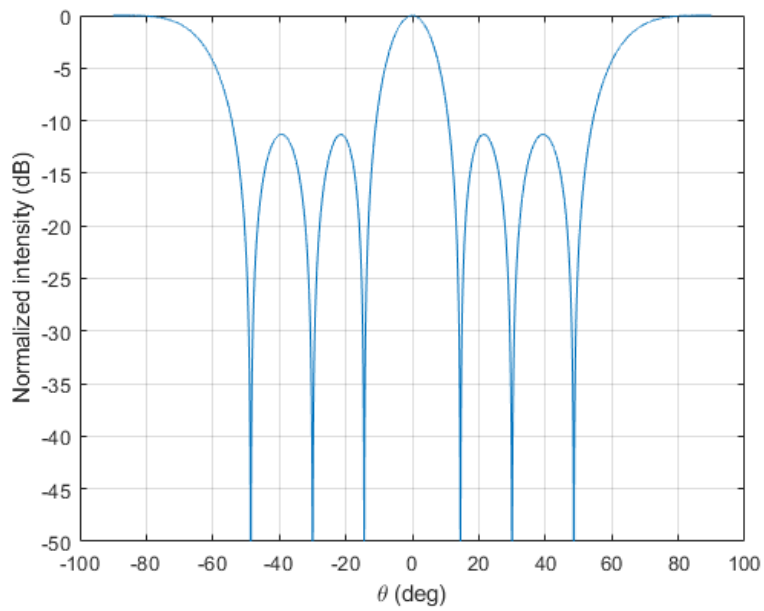


**Figure 4. 4: GLs are introduced at  $\theta = \pm 90^\circ$  due to element spacing**

The SA spacing can be found from Eq. (4.2) which gives  $D_x = D_y = 8.15 \mu m$ . Simulating the  $AF_{SA}$  at this spacing will introduce many GLs in the visible region as seen in Fig. 4.5.

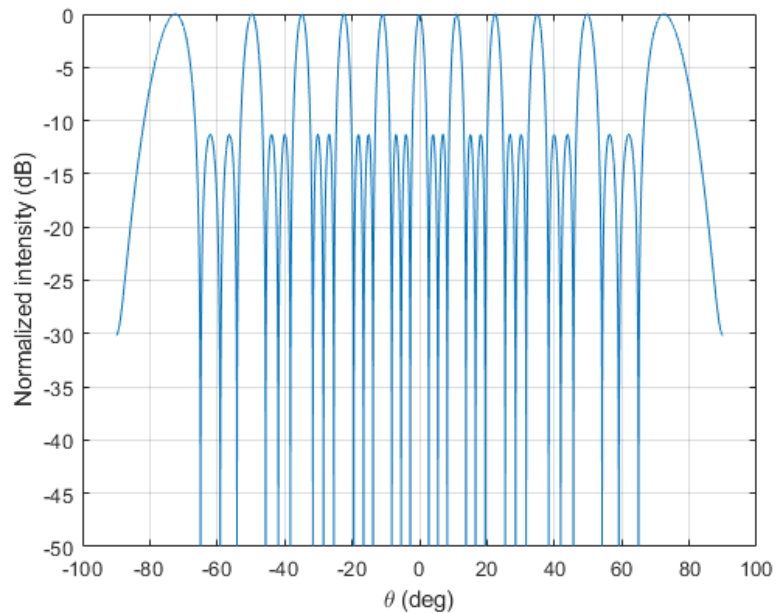


**Figure 4. 5: SA pattern with many GLs due to the large spacing**

The final array pattern can now be formed with both definitions. It is shown in Fig. 4.6 that by taking the product of the two patterns, the final array pattern can be formalized. Most of the GLs in the SA pattern are reduced by the unit cell pattern while the GLs at the edges of the visible region are still at a relatively high power due to both patterns exhibiting GLs at those locations.

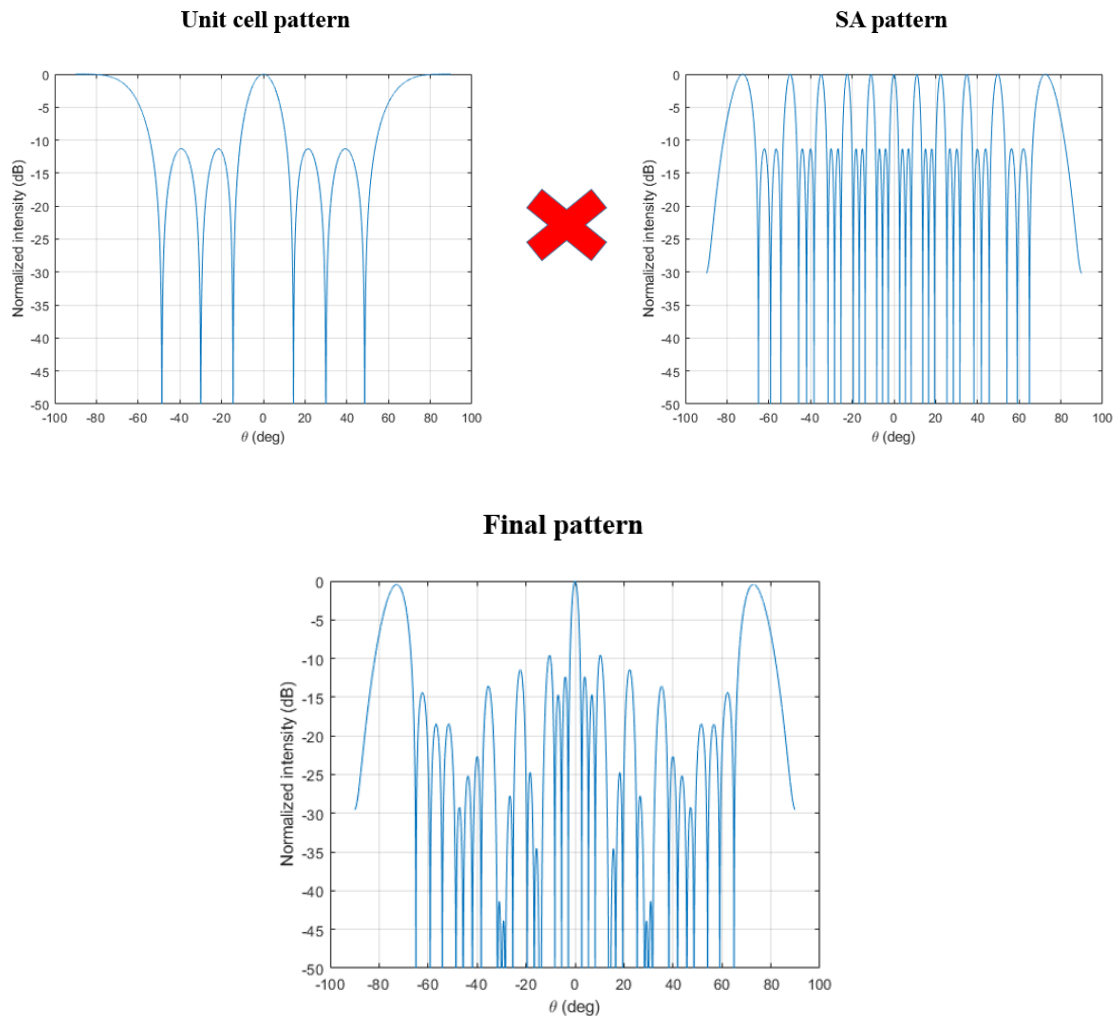


**Figure 4. 6: Illustration of Eq. (4.3)**

We can see in Fig. 4.7 a clearer formation of the final array pattern. By superimposing all three patterns, it is easy to see how the final array pattern is formed.

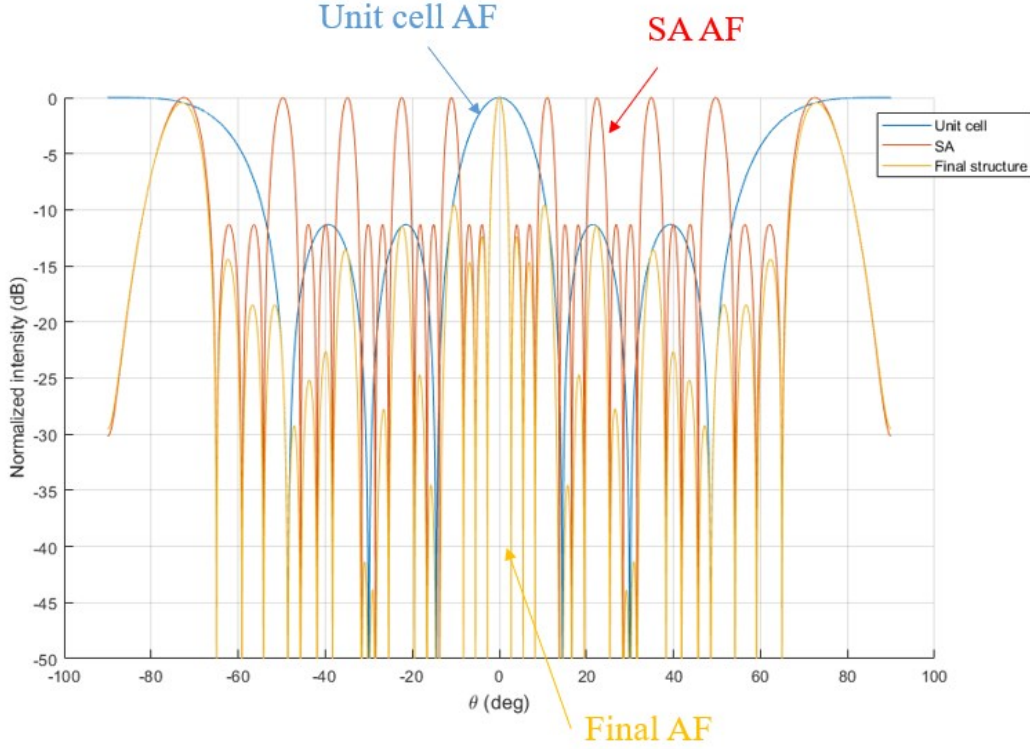


**Figure 4. 7: Unit cell, SA, and Final pattern**

Once the SA positions are formed, the rotation method can be applied to each unit cell. The rotation angle  $\alpha$  is chosen to suppress the grating lobes that would normally appear in a periodic lattice. The rotation method used is chosen from a paper by V. D. Agrawal [24]. In this paper, a method of rotation is defined that can effectively reduce the power of each grating lobe (GL) by positioning the location of each SAs GL on the nulls of an adjacent SA.

To apply the rotation method, we define the rotation angle for each unit cell as  $\alpha$ . Once  $\alpha$  is chosen, we can rotate each unit cell in the following manner,

$$\alpha_n = 0 * \alpha, \pm 1 * \alpha, \pm 2 * \alpha, \pm 3 * \alpha, \dots (4.4)$$

To apply  $\alpha_n$ , we start with the leftmost unit cell and progress right until the last unit cell in each row. Then we continue to the next row until every unit cell is rotated. We can see how the structure appears after rotation in Fig. 4.8. We can see the first unit cell in the left-most corner has a rotation angle of  $\alpha_1 = 0^\circ$  and then each subsequent unit cell follows the definition in Eq. (4.4). One important fact to note about the rotation scheme is the orientation of the unit cells once  $\alpha_n > 90^\circ$ . Due to the lattice's rectangular

symmetry, all unit cells past  $90^\circ$  will have a similar orientation to the unit cells between  $\alpha_1 = 0^\circ$  till  $\alpha_n = 90^\circ$  where  $\alpha_n$  is the represents the unit cell that undergoes a  $90^\circ$  rotation. We will comment in the results portion of this chapter what effect this phenomenon has.

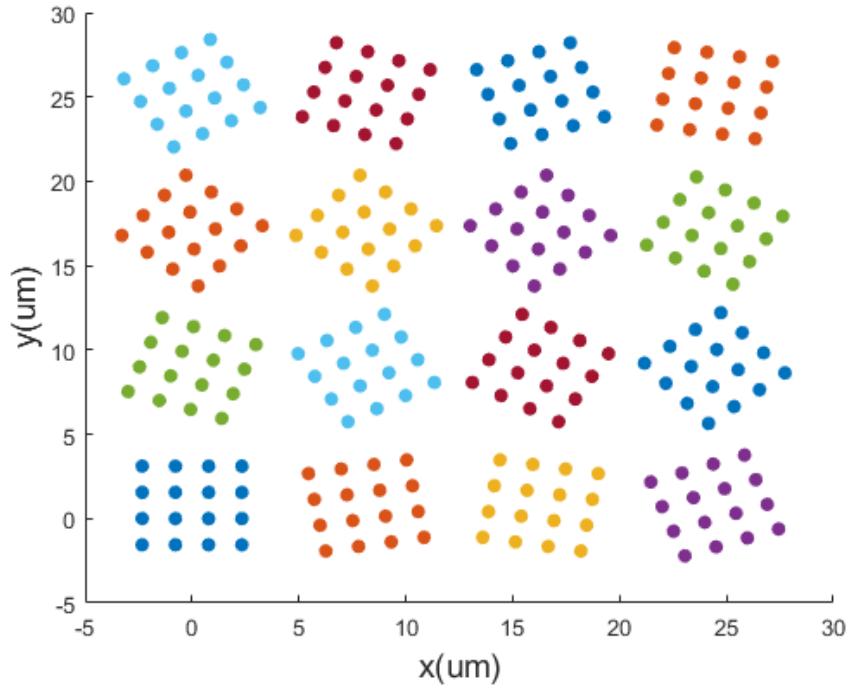


**Figure 4. 8: SA structure after rotation where  $\alpha = 10^\circ$**

The effect of rotating each unit cell can be understood by observing the radiation pattern before and after rotation. Within Fig. 4.9, we contrast the difference between the locations of each GL as the unit cell is rotated by  $\alpha$ .

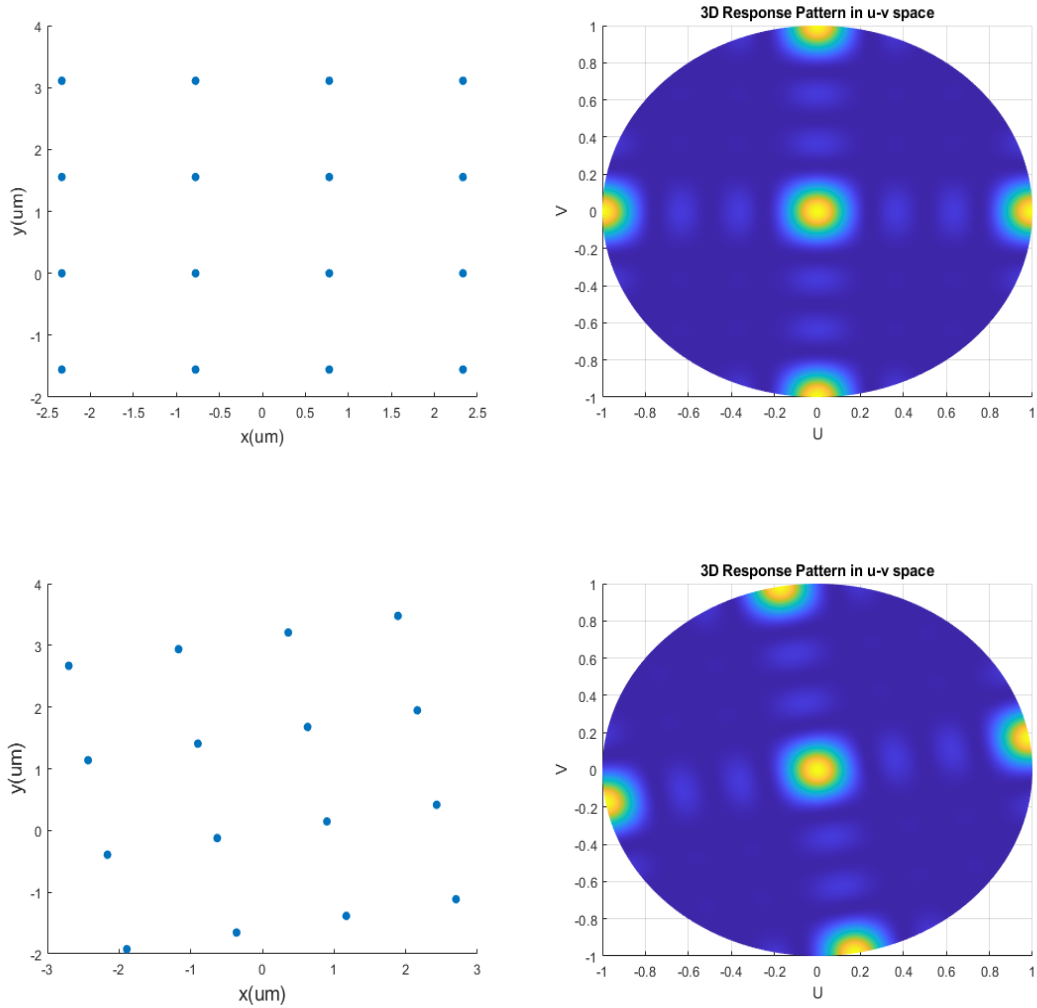


**Figure 4. 9: GL rotation due to lattice rotation**

This type of non-uniform array arrangement has not been explored yet for OPA design and would be a great benefit since one main issue is the spacing constraints imposed on the OPA which heavily limit the FOV due to aliasing. The design also retains the periodicity within the unit cell, lowering the complexities that would arise in non-uniform arrays that rely on randomization to eliminate GLs.

### 4.1.2 Simulations

Within this work, it is assumed that all elements are identical, equally spaced, and are fed in phase so that the contribution of all element's points in the direction of the ML. Using these elements, all calculations of the AF are done at a wavelength of  $1.5 \mu\text{m}$ . Because we are studying the far field radiation patterns, the elements are ideal point sources.

We study the performance of the array by calculating the SL contrast and BW while varying each structural parameter individually. There are nine design parameters used to define the structure. Each unit cell is defined by the following four parameters,  $N_r, N_c, d_x$  and  $d_y$  while the SAs are defined by  $N_{SA_r}, N_{SA_c}, D_x, D_y$ , and  $\alpha$ . Two parameters,  $D_x$  and  $D_y$  are fixed at an appropriate value for parameters that affect it as described in Eq. (4.2). This will ensure that  $D_x$  and  $D_y$  do not change when we study the effect of changing  $N_r, N_c, d_x$  and  $d_y$ . Also, we will comment on the differences in performance between each unit cell at the end of the section.

The following design is selected for the study:

- $N_r$  and  $N_c = 4$
- $d_x$  and  $d_y = 1 * \frac{2}{\sqrt{3}}\lambda = 1.79 \mu m$  and  $1 * \lambda = 1.55 \mu m$
- $N_{SA_r} = N_{SA_c} = 4$
- $\alpha = 10^\circ$

The choice of the parameters can be explained through several reasons. Regarding the unit cell and SA sizes, 4x4 is selected to keep the size of the array uniform throughout and to have a sizable number of elements within the lattice (256 elements). The unit cell spacing,  $d_x$  and  $d_y = 1 * \frac{2}{\sqrt{3}}\lambda$  and  $1 * \lambda$ , is chosen to create an equilateral triangular unit cell which is commonly used when using a triangular lattice. We use the same spacing for the rectangular unit cell to keep the study consistent between the two unit cells. Finally, the rotation angle,  $\alpha = 10^\circ$ , is selected only to demonstrate the change in the GL power after rotation. Once we study the effect of  $\alpha$ , we will see how the performance is affected for a wide range of  $\alpha$ .

We first study the two unit cell parameters,  $N_r$  and  $N_c$ . In order to properly account for the whole trend range ( $N_r = 1:20$ ),  $D_x$  and  $D_y$  are fixed at  $35 \mu m$  and  $35 \mu m$  respectively for  $N_r = 20$  and  $D_x$  and  $D_y$  are fixed at  $40 \mu m$  and  $40 \mu m$  respectively for  $N_c = 20$ .

The impact on the SL contrast and BW when changing the two-unit cell parameters,  $N_r$  and  $N_c$  are demonstrated in Fig. 4.10 and Fig 4.11 respectively. Both  $N_r$  and  $N_c$  share a similar impact on the SL contrast and BW. Within the structure, the unit cell spacing and SA spacing is kept constant while  $N_r$  and  $N_c$  are increased individually to

20. The curves indicate that the SL contrast increases exponentially for an increasing unit cell size. The change in the structure as  $N_r$  increases is shown in Fig. 4.12.

The BW is virtually unaffected by the larger unit cell size. This is primarily due to  $D_x$  and  $D_y$  which at the constant value selected ( $D_x$  and  $D_y = 35 \mu m$ ) results in a beamwidth of  $0.58^\circ$ .

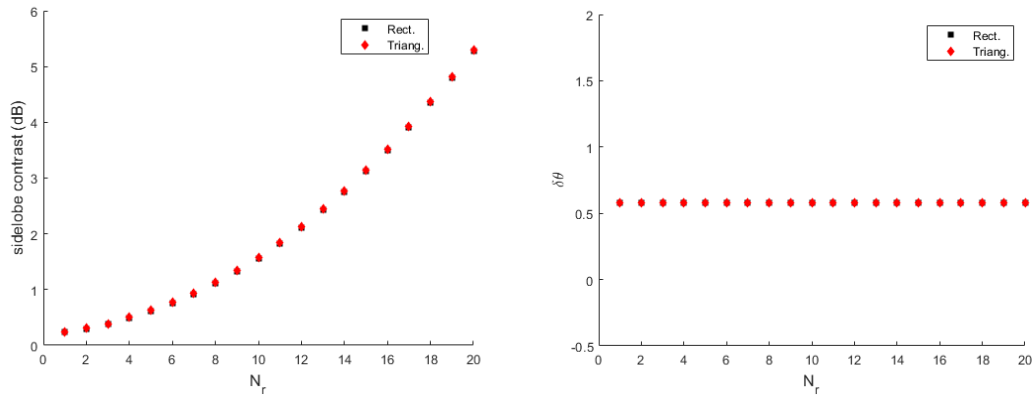


**Figure 4. 10: Impact of  $N_r$  on the SL contrast and BW**

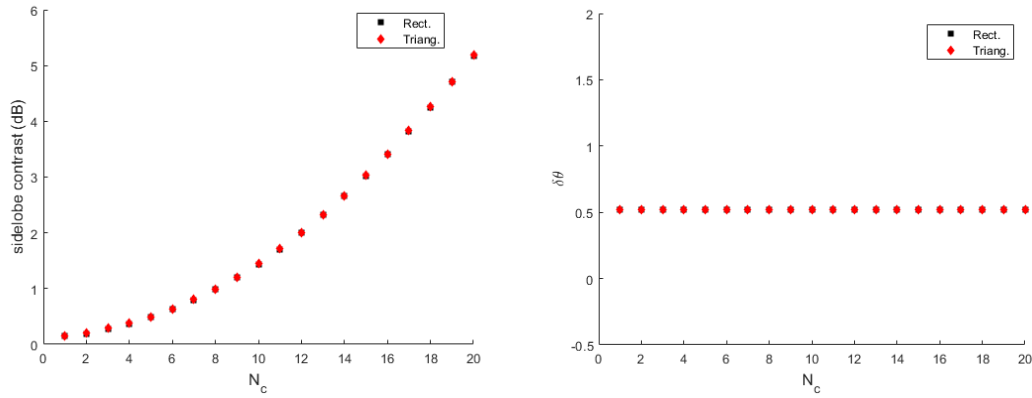


**Figure 4. 11: Impact of  $N_c$  on the SL contrast and BW**

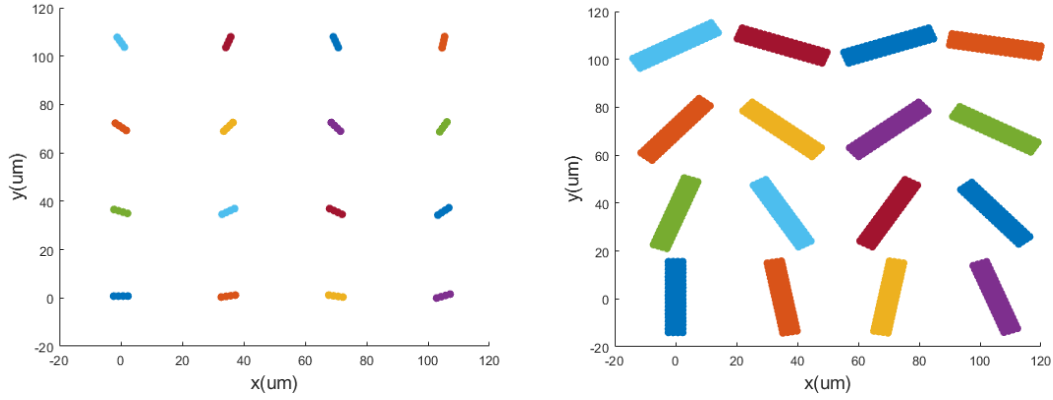


**Figure 4.12: Array Structure for  $N_r = 1$  and  $20$  @  $D_x$  and  $D_y = 35 \mu\text{m}$**

The next parameters of interest are  $N_{SA_r}$  and  $N_{SA_c}$ . The effect of increasing either  $N_{SA_r}$  and  $N_{SA_c}$  is demonstrated in Fig. 4.13 and Fig. 4.14. It is understood that  $N_{SA_r}$  or  $N_{SA_c}$  will have a considerable effect on the SL contrast and BW when either are made larger. Both parameters share an equal contribution in improving the SL contrast as seen in the trend lines. When both  $N_{SA_r}$  and  $N_{SA_c}$  are equal, the SL contrast is often at its highest or lies in the range of the highest point. This resembles uniform arrays where after a certain number of elements ( $N$ ), the SL contrast becomes independent of  $N$ . We can also make note of the orientation repetition created by the rotation scheme and the rectangular symmetry. If we look at the case of  $N_{SA_r} = 20$ , this structure will have 80 unit cells within the whole structure. This would mean that there would be many sets of unit cells with similar orientations. However, we do not see any large decreases in the SL contrast, so this phenomenon is not creating any deficiencies in the performance.

Increasing either  $N_{SA_r}$  or  $N_{SA_c}$  is seen to decrease the BW. This is expected since increasing the total length of the array along the axis reduces the BW along that direction.

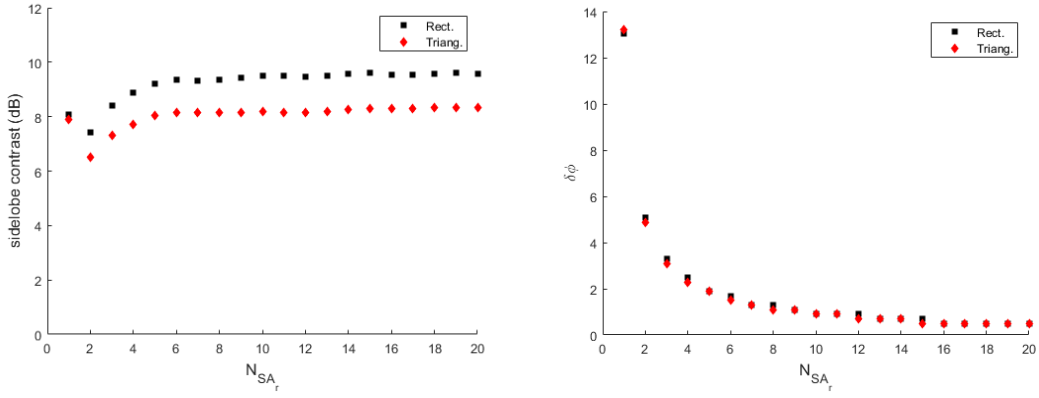


**Figure 4. 13: Impact of  $N_{SA_r}$  on the SL contrast and BW**

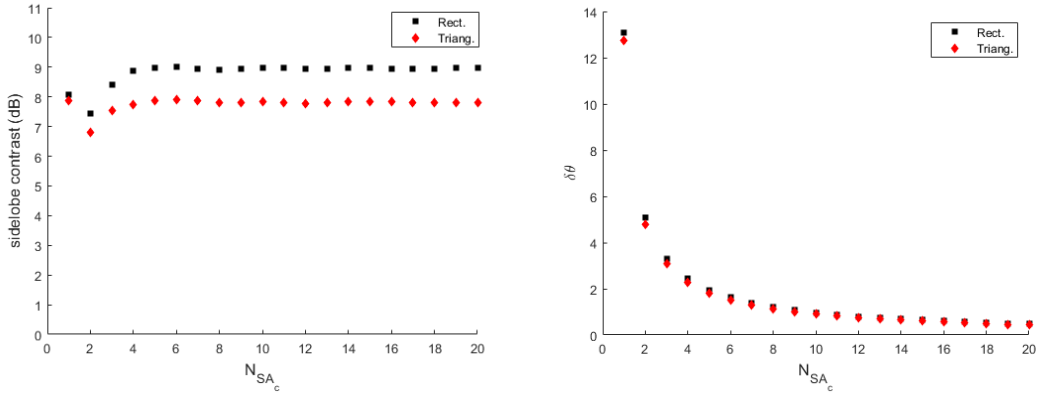


**Figure 4. 14: Impact of  $N_{SA_c}$  on the SL contrast and BW**

The next parameter of interest is the inter-element spacing  $d_x$  and  $d_y$  which increases from  $1 * \frac{2}{\sqrt{3}}\lambda = 1.79 \mu m$  to  $8 * \frac{2}{\sqrt{3}}\lambda = 14.4 \mu m$ . We can see in Fig. 4.15 that increasing both  $d_x$  and  $d_y$  increase the SL contrast exponentially. The constant SA spacing chosen here,  $D_x$  and  $D_y = 75 \mu m$ , reflects the largest unit cell spacing chosen where  $d_x = 8 * \frac{2}{\sqrt{3}}\lambda = 14.36 \mu m$ . This increase can now be understood from the unit cell size increasing which will make neighboring SAs closer to each other as seen in Fig. 4.16. We do not see any change in the BW due to the SA spacing. The BW stays consistent @  $0.28^\circ$ . Since the SA spacing is so large, the change in the size of the unit cell has little to no effect on changing the BW of the whole structure.

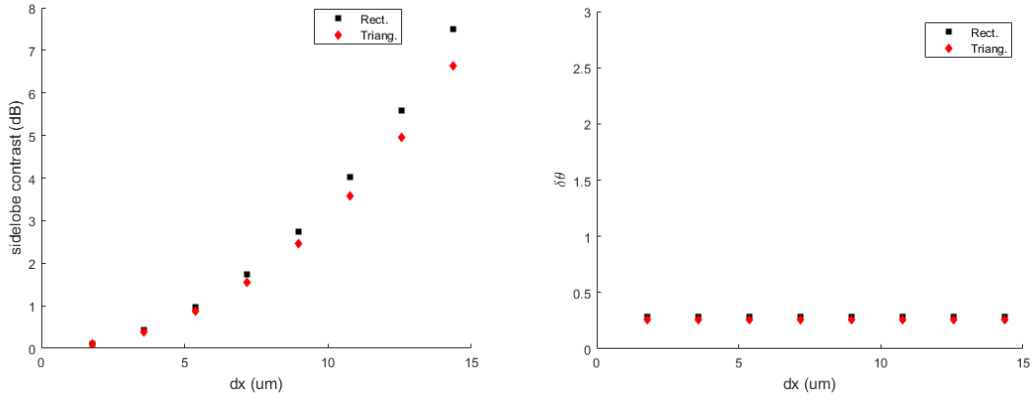


**Figure 4.15: Impact of  $d_x$  and  $d_y$  on the SL contrast and BW**

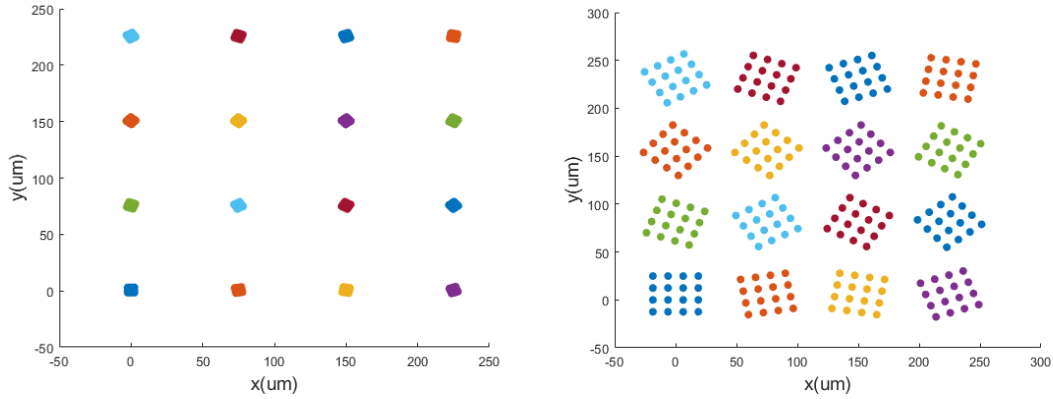


**Figure 4.16: Array structure for  $d_x = 1 * \frac{2}{\sqrt{3}} \lambda$  and  $d_x = 8 * \frac{2}{\sqrt{3}} \lambda$**

The next parameters of interest are  $D_x$  and  $D_y$ . We can see in Fig. 4.17 that increasing  $D_x$  and  $D_y$  has a large impact on the SL contrast. Increasing by just a few  $\mu m$  can greatly decrease the SL contrast. This can be understood by the principle in how the GLs are suppressed. When the spacing is made larger between each unit cell, more GLs are introduced and redistributed through rotation which consequently raises the total SL power.

We start the SA spacing for the triangular unit cell at a few  $\mu m$  higher than the rectangular unit cell due to the increased size of the triangular unit cell which results in a higher size from Eq. (4.2). Therefore, the SL contrast is lower for the triangular unit cell.

Again, the BW decreases due to the increased SA spacing.

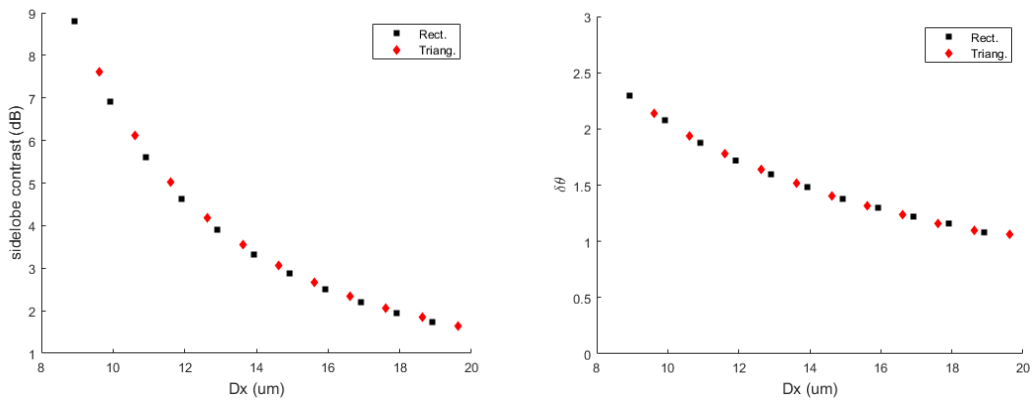


**Figure 4.17: Impact of  $D_x$  and  $D_y$  on the SL contrast and BW**

The final parameter of interest is the rotation angle  $\alpha$ . We can see in Fig. 4.18 that  $\alpha$  has a considerable effect on the SL contrast. For the inter-element spacing chosen, GLs can be seen in the pattern of both unit cell structures with a  $0^\circ$  rotation angle. After rotation, the GLs can be eliminated which improves the SL contrast considerably.

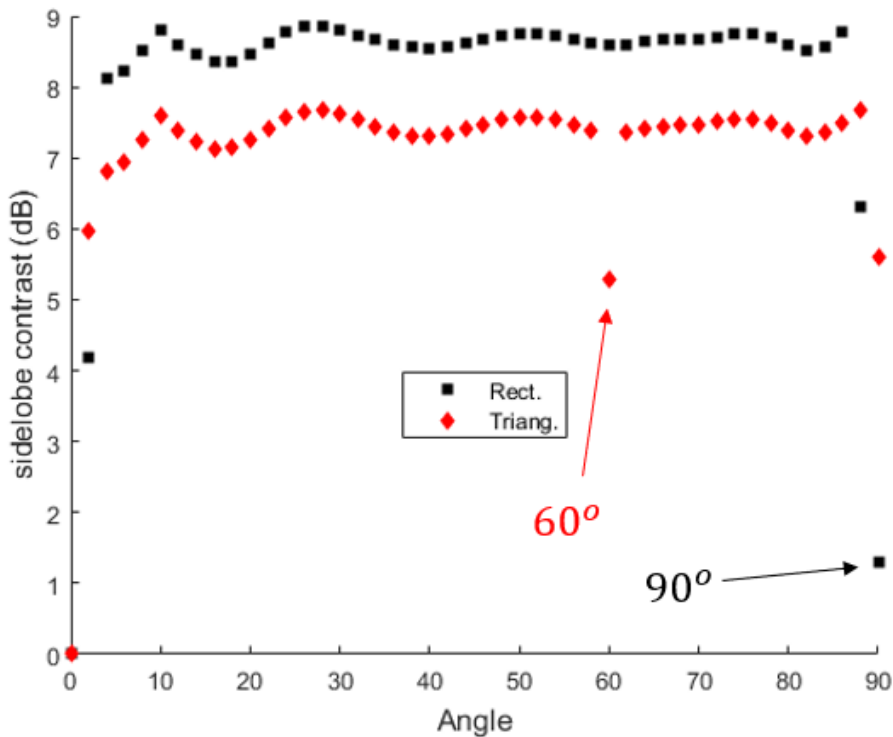


**Figure 4.18: Impact of  $\alpha$  on SL contrast**

There are some key points of interest within the figure, particularly at  $\alpha = 60^\circ$  and  $90^\circ$ . We can see that the SL contrast decreases significantly at these two points which can be attributed to the symmetry of each unit cell. For a rectangular unit cell, the decrease occurs at  $\alpha = 90^\circ$  which can be understood by observing the GL locations in Fig. 4.19.

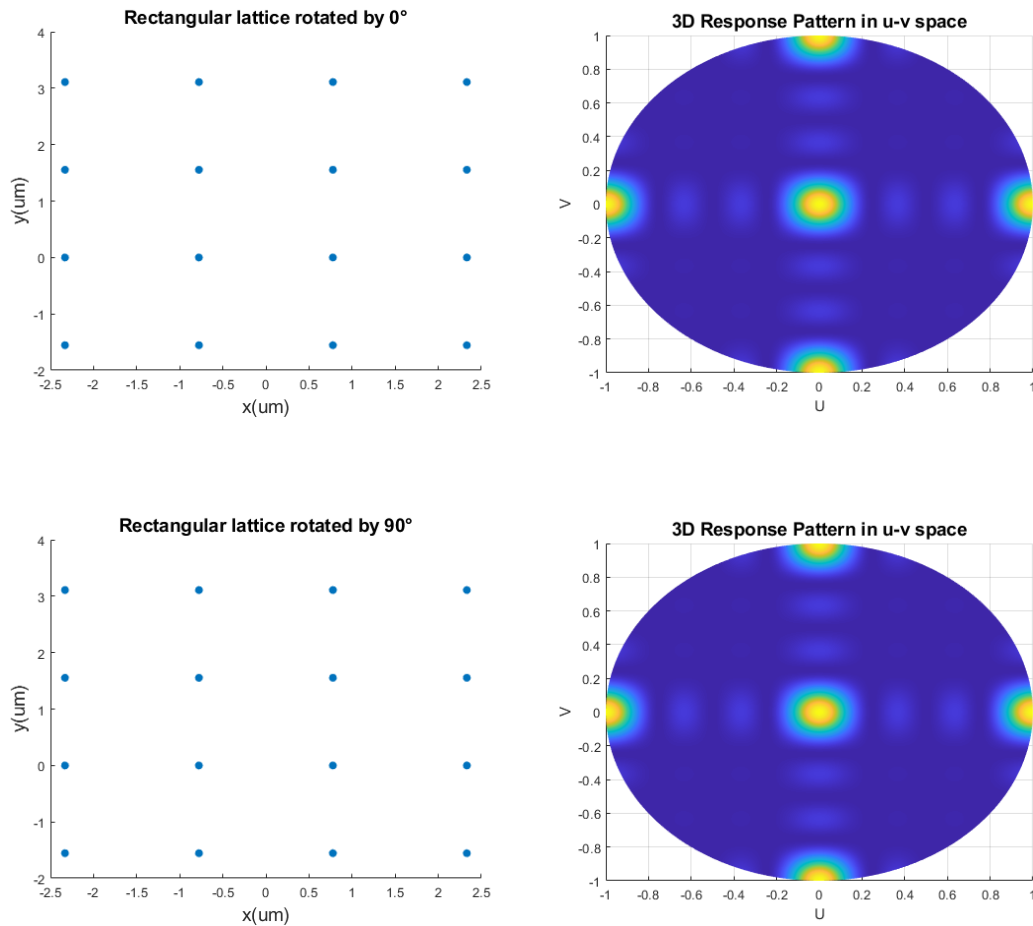


**Figure 4. 19: Equivalent GL locations between a rectangular unit cell with rotation angle  $\alpha = 0^\circ$  and  $90^\circ$**

The decrease at  $\alpha = 60^\circ$  in Fig. 4.18 for the triangular unit cell occurs for the same reasons. The triangular unit cell used has a rotation symmetry of  $60^\circ$ , so the GLs would experience a rotation that would make their locations equivalent to a unit cell with no rotation. We see this illustrated in Fig. 4.20.

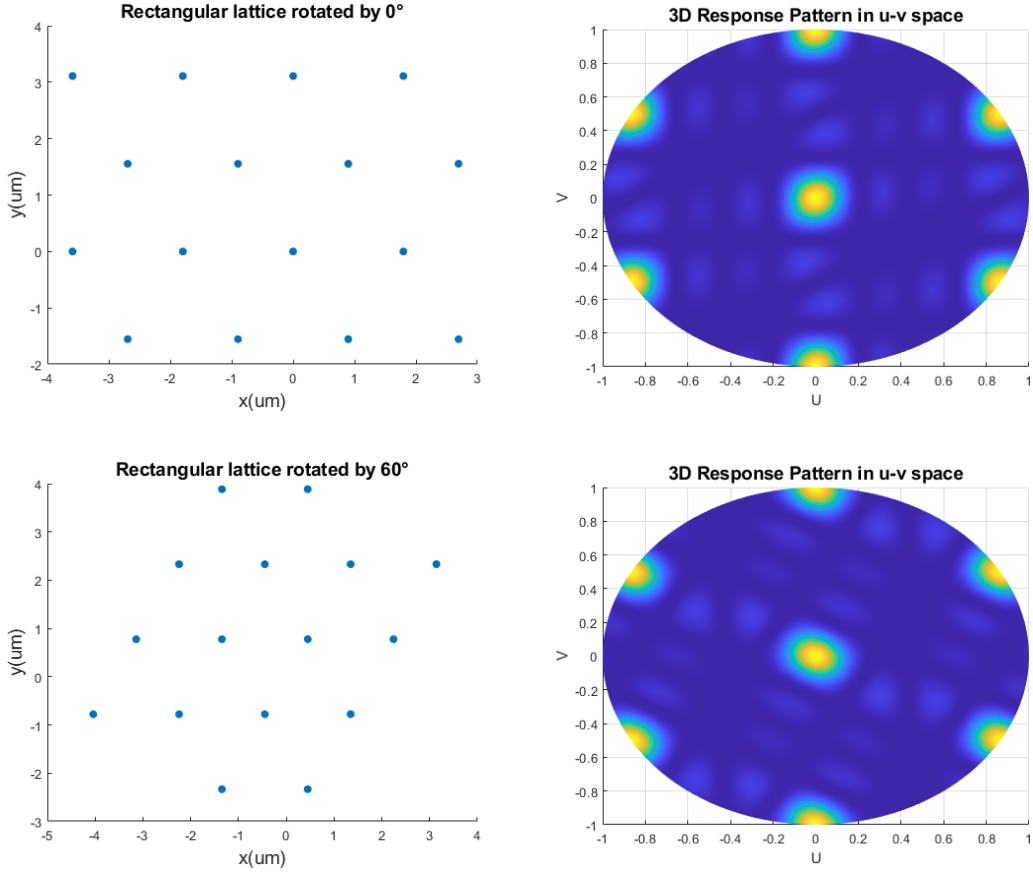


**Figure 4. 20: Equivalent GL locations between a triangular unit cell with rotation angle  $\alpha = 0^\circ$  and  $60^\circ$**

For most of the structural parameters, the trends identified were very similar between the rectangular and triangular unit cells. One stark contrast between the two-unit cells was the peak SL contrast. When using a rectangular unit cell, the peak SL contrast was very close to 9 dB while the triangular unit cell had a peak SL contrast close to 8 dB. The cause of this difference is due to the spacing  $D_x$  and  $D_y$  which is slightly smaller when using a rectangular unit cell as the total area of the rectangular unit cell is smaller. Thus, from Eq. (4.1) and Eq. (4.2), we should expect a smaller  $D_x$  and  $D_y$ . The benefit of the triangular unit cell where the lattice can delay the appearance of GLs is not as significant with our application as we are trying to reduce the strength of the GLs by redistributing their power through rotations.

## 4.2 Triangular Planar Sub-Array

### 4.2.1 Design Methodology

We again select both rectangular and triangular unit cells for this section. The same design parameters are used where we considered the element spacing as  $d_x$  and  $d_y$  and the number of rows/columns as  $N_r$  and  $N_c$ .

We now select a triangular SA structure which has minor differences to the rectangular SA structure. Like the triangular unit cell, the triangular SA lattice is constructed by shifting every second row by half the element spacing. For the SA lattice, the element spacing is now considered the SA spacing, denoted as  $D_x$  and  $D_y$ . Therefore, every unit cell within the second row is shifted by  $D_x/2$ . The triangular SA lattice is pictured in Fig. 4.21.

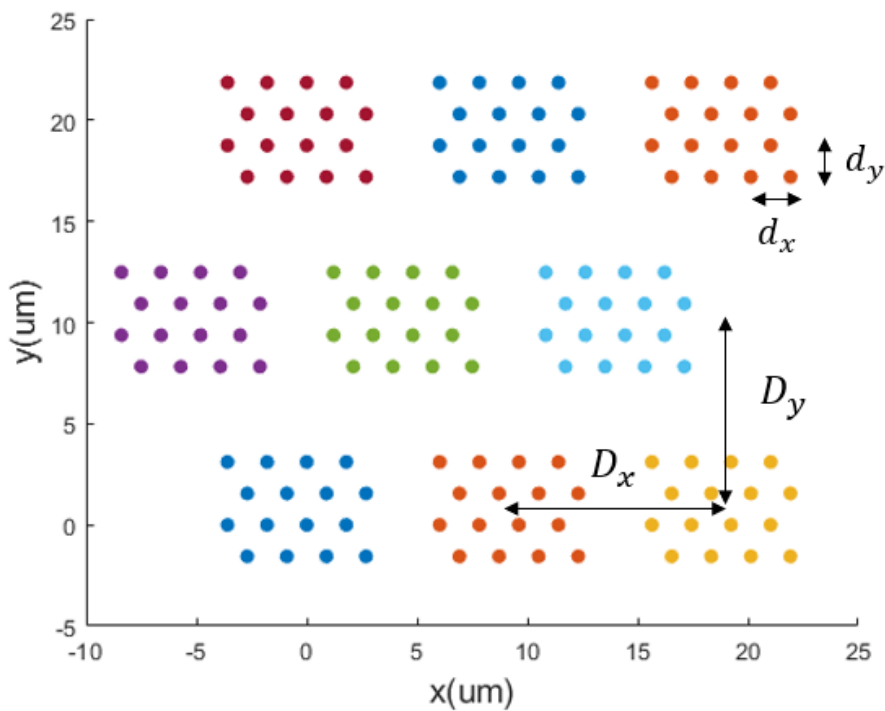


Figure 4. 21: 3x3 triangular SA lattice with 4x4 triangular unit cells

Again, we apply the same rotation method as section 4.1.1 to each unit cell to form the rotated SA lattice.

## 4.2.2 Simulations

We will use the exact same elements as in 4.1.2 with all the same specifications described previously.

The same nine design parameters are studied for the triangular SA lattice. To repeat, we will use four unit cell parameters,  $N_r, N_c, d_x$  and  $d_y$  and the five SA parameters,  $N_{SA_r}, N_{SA_c}, D_x, D_y$ , and  $\alpha$ .

The following design is selected for the study:

- $N_r$  and  $N_c = 4$
- $d_x$  and  $d_y = 1.79 \mu m$  and  $1.55 \mu m$
- $N_{SA_r} = N_{SA_c} = 4$
- $\alpha = 10^\circ$

We choose a similar design structure to the one used in the previous section for comparison reasons. The first parameters we study are the two unit cell parameters,  $N_r$  and  $N_c$ . In order to properly account for only these two parameters,  $D_x$  and  $D_y$  are fixed at  $35 \mu m$  and  $35 \mu m$  respectively for  $N_r = 20$  and  $D_x$  and  $D_y$  are fixed at  $40 \mu m$  and  $40 \mu m$  respectively for  $N_c = 20$ . We display the results of increasing  $N_r$  and  $N_c$  in Fig. 4.22 and Fig. 4.23 respectively. We can see a similar trend in both parameters where the SL contrast increases exponentially, and the BW remains constant. This is what we expected coming from the study of the rectangular SA lattice.

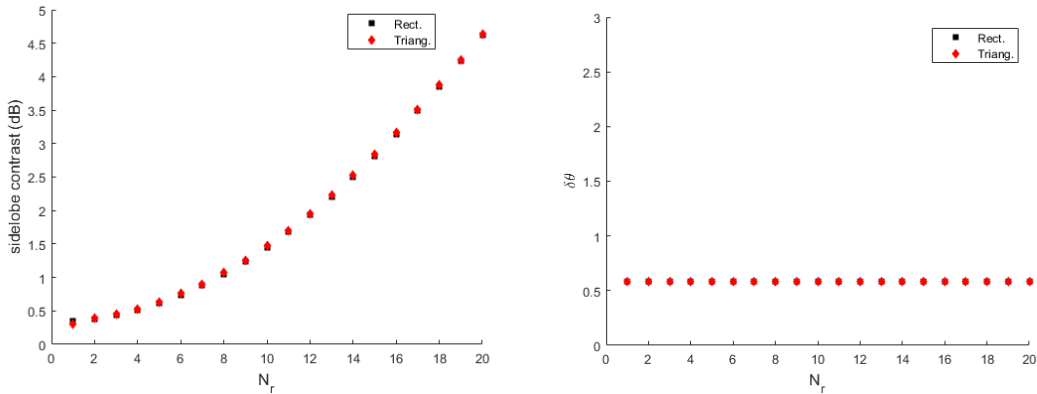


**Figure 4. 22: Impact of  $N_r$  on the SL contrast and BW (Triangular SA)**

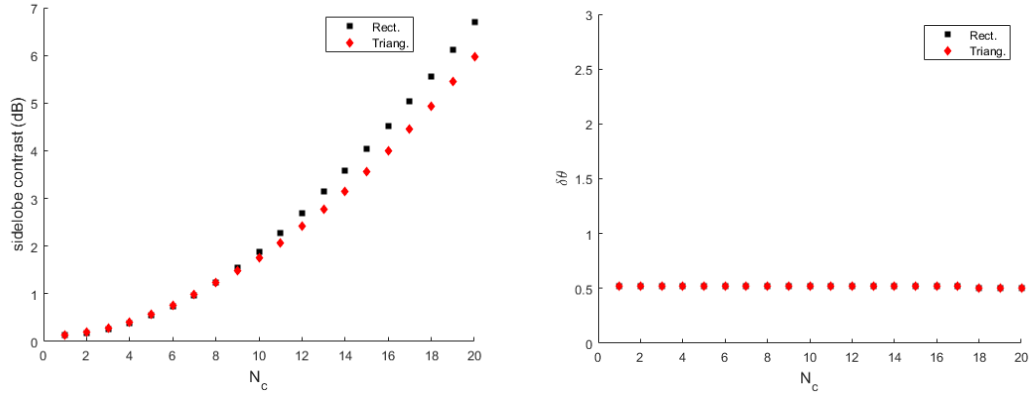


**Figure 4. 23: Impact of  $N_c$  on the SL contrast and BW (Triangular SA)**

The next parameters of interest are the SA rows/columns,  $N_{SA_r}$  and  $N_{SA_c}$  which are shown in Fig. 4.24 and Fig. 4.25 respectively. We can see that the SL contrast increases to near 10 dB while the BW exponentially decreases across the whole trend. This is similar to what we observed for the rectangular SA lattice, so the same explanations in 4.1.2 stand.

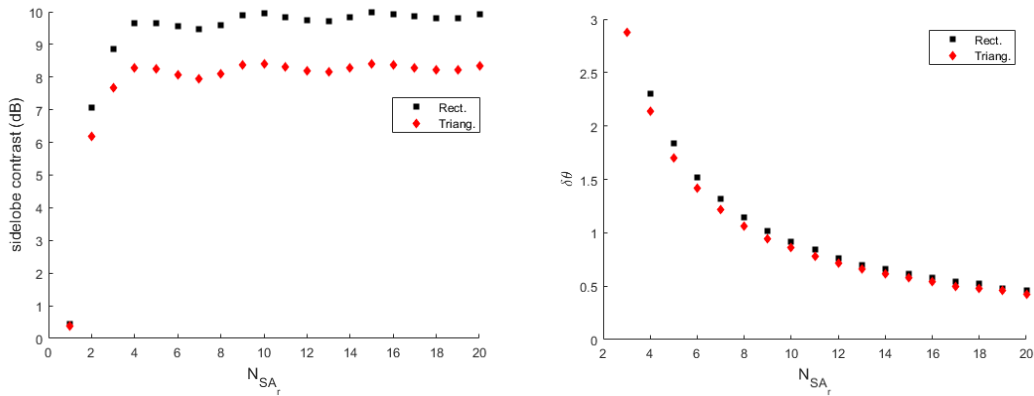


**Figure 4. 24: Impact of  $N_{SA_r}$  on the SL contrast and BW (Triangular SA)**

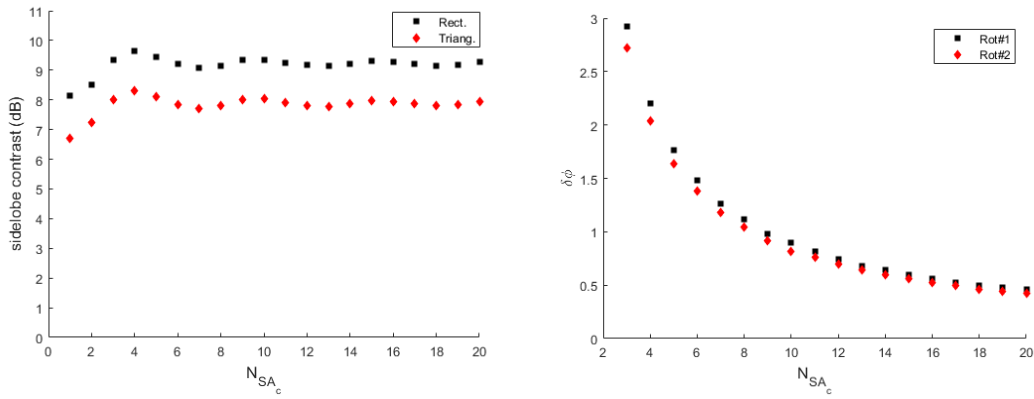


**Figure 4. 25: Impact of  $N_{SA_c}$  on the SL contrast and BW (Triangular SA)**

The unit cell element spacings,  $d_x$  and  $d_y$  demonstrate a similar trend as seen in section 4.1.2. For the triangular SA spacing, we choose  $D_x$  and  $D_y = 80 \mu m$  to reflect the design trend. We can see in Fig. 4.26 that the SL contrast exponentially increases as the unit cell spacing increases while the BW remains constant due to the large SA spacing chosen.

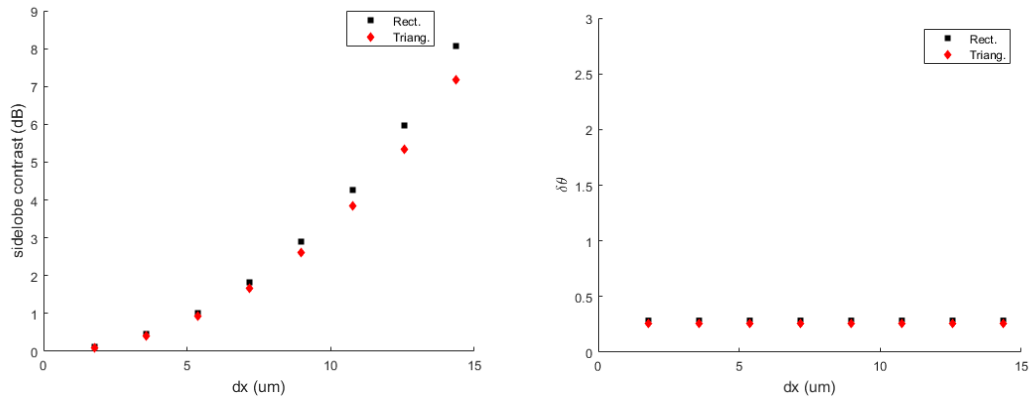


**Figure 4. 26: Impact of  $d_x$  and  $d_y$  on the SL contrast and BW (Triangular SA)**

We follow this with the SA spacing,  $D_x$  and  $D_y$ . We incrementally increase the SA spacing and observe a similar trend in Fig. 4.27 where both the SL contrast and BW exponentially decrease. It is apparent that both,  $D_x$  and  $D_y$  have the largest impact on the SL contrast and BW.

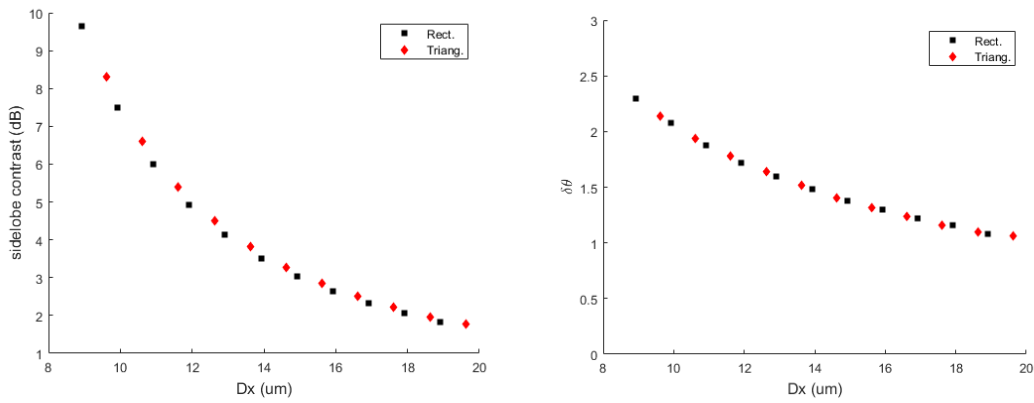


**Figure 4. 27: Impact of  $D_x$  and  $D_y$  on the SL contrast and BW (Triangular SA)**

The final parameter of interest is the rotation angle  $\alpha$ . We can see in Fig. 4.28 that  $\alpha$  has a considerable effect on the SL contrast. For the inter-element spacing chosen, GLs can be seen in the pattern of both unit cell structures with a  $0^\circ$  rotation angle. After rotation, these spurious beams can be eliminated which improves the SL contrast considerably. We can also observe the decreases in dB at the same two points where  $\alpha = 60^\circ$  and  $90^\circ$ . This is expected since the unit cells are still being rotated in the same manner. We do see a difference in dB between the rectangular and triangular SA lattices where the SL contrast appears to be higher for the triangular SA arrangement.

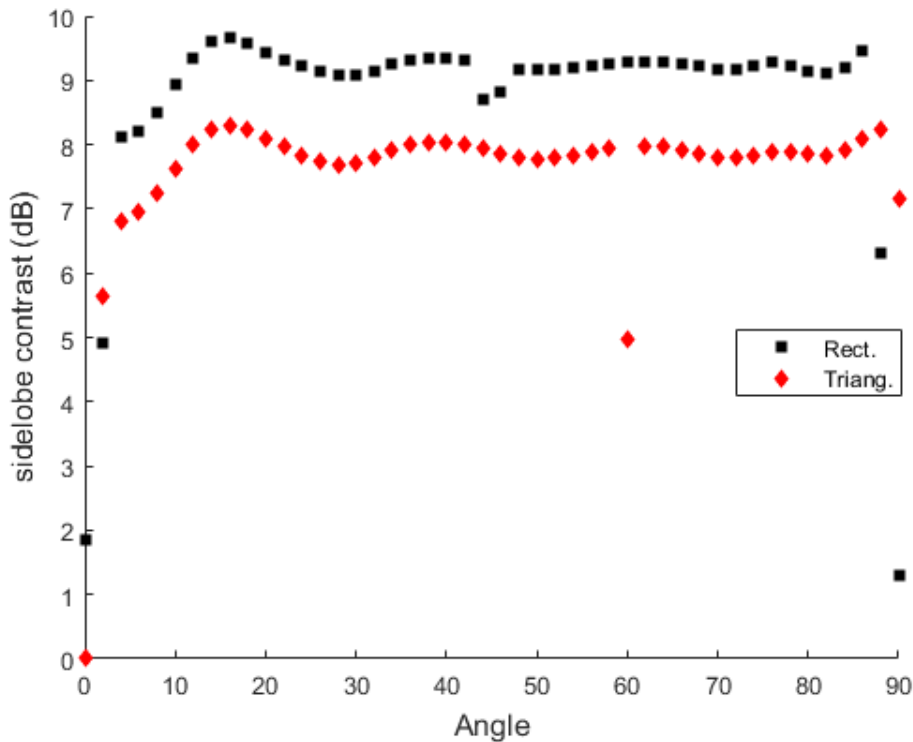


**Figure 4. 28: Impact of  $\alpha$  on SL contrast (Triangular SA)**

Repeating the same study for the triangular SA lattice has shown many key similarities between the two SA lattices. The trends we see in each parameter are nearly identical save for a few differences. The overall SL contrast is higher for the triangular SA lattice which is likely due to how the SA lattice changes the overall radiation pattern. We can see the radiation pattern of the rectangular and triangular SA lattices displayed in Fig. 4.29 and Fig. 4.30. We utilized a rectangular unit cell with  $N_r = N_c = 4$ , for each SA lattice but this does not have an effect on the differences we see in each figure.

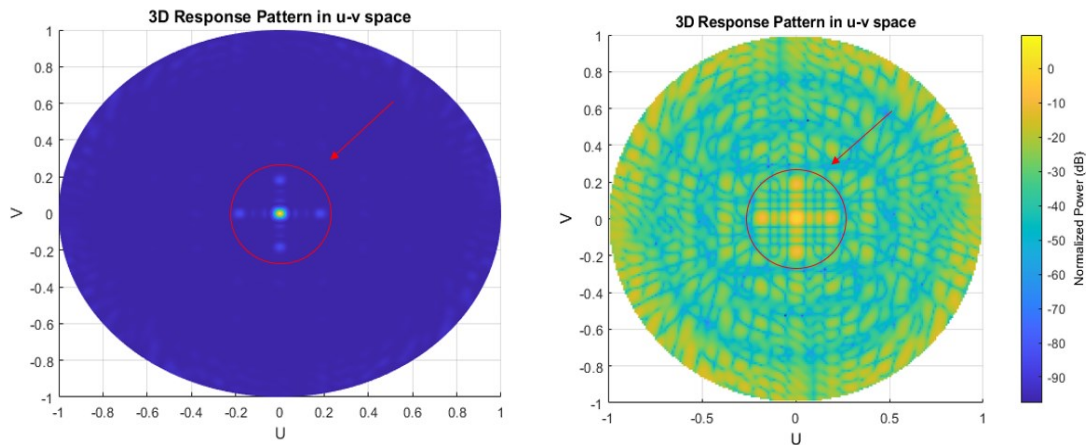


**Figure 4. 29: Radiation pattern plotted in  $uv$  space for a Rectangular SA**

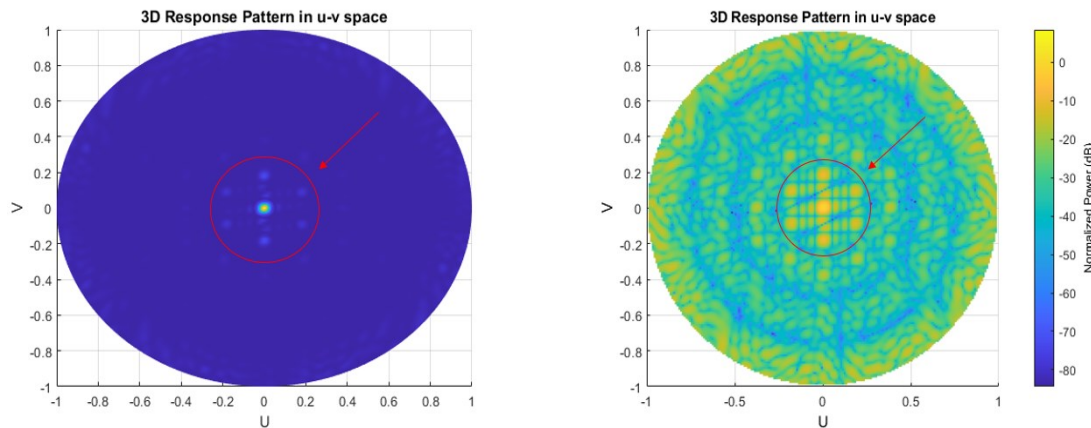


**Figure 4. 30: Radiation pattern plotted in  $uv$  space for a Triangular SA**

The differences between the two SA lattices lie in the redistribution of the SLs, particularly near the ML. We can see how the rectangular SA has 4 clear SLs situated around the ML while the Triangular SA has 6 SLs around the ML. Re-distributing the SLs from 4 to 6 slightly lowers the power in each SL which is why we see the triangular SA lattice have an overall higher SL contrast.

### 4.3 Uniform Rectangular Array and Rotated SA comparison

We produce the following comparison between the uniform rectangular array (URA) with a 16x16 lattice and a rectangular SA lattice with  $N_r = N_c = N_{SA_r} = N_{SA_c} = 4$ . Both lattices are rectangular and have an inter-element spacing of  $d_x = d_y = 5\lambda = 7.77 \mu\text{m}$ . We choose  $5\lambda$  for the inter-element spacing to demonstrate the impact of such a large element spacing within an OPA. It is clear from Fig. 4.31 that many GLs exist in the visible region due to the current spacing. This inhibits the available steering range of the ML, limiting the practicality of the OPA.

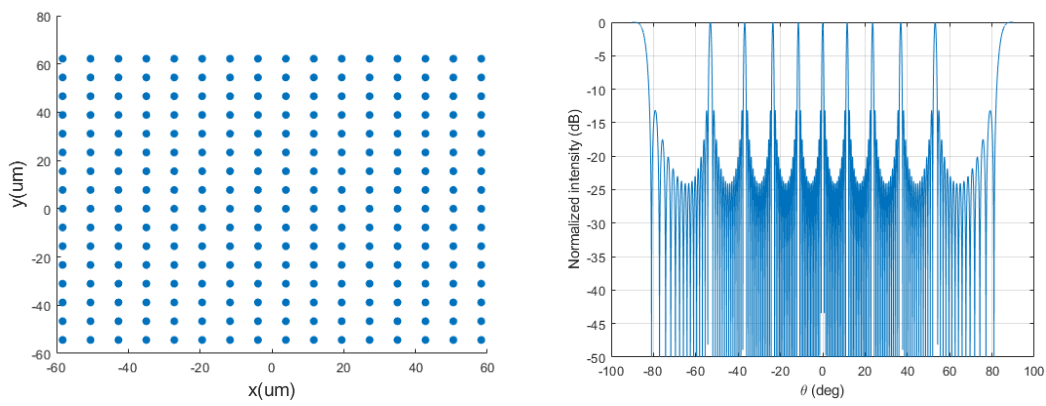


**Figure 4.31: 16x16 URA with pattern cut demonstrating GLs**

Introducing the rotated SA greatly changes the radiation pattern as seen in Fig. 4.32. Now the elements in each unit cell do not constructively interfere at the same angles of  $\theta$ , which breaks the limitation imposed by the spacing. The ability to suppress the GLs with a large element spacing is a desirable trait for OPAs.

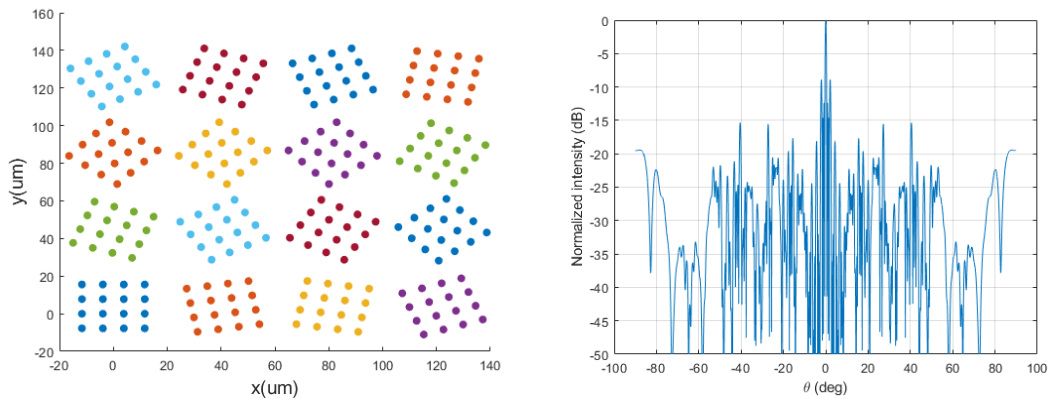
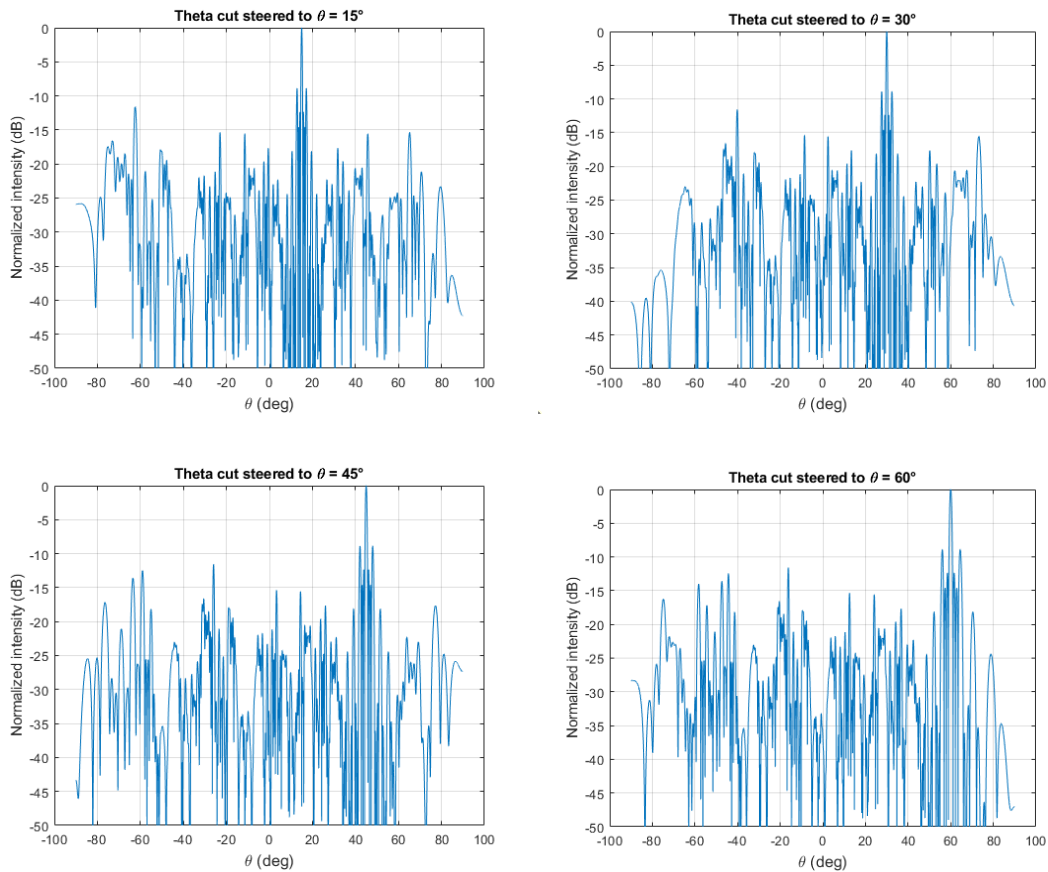


**Figure 4.32: Rotated rectangular SA with corresponding pattern cut**

To demonstrate the beam steering capabilities of the rotated SA, we steer the ML to various angles of  $\theta$  and measure the SL contrast and BW. The results are recorded in Table 4.1 and are illustrated in Fig. 4.33. The pattern cuts demonstrate that even with steering the main beam, no aliasing occurs even at angles as far as  $\theta_0 = 80^\circ$ .

**Table 4. 1: Measured SL contrast and BW for varying angles of  $\theta_0$  (Rectangular SA lattice)**

$\theta_0$	SL contrast (dB)	BW
$0^\circ$	8.89	$0.5^\circ$
$15^\circ$	8.89	$0.52^\circ$
$30^\circ$	8.89	$0.58^\circ$
$45^\circ$	8.89	$0.70^\circ$
$60^\circ$	8.89	$0.99^\circ$
$80^\circ$	8.89	$2.83^\circ$



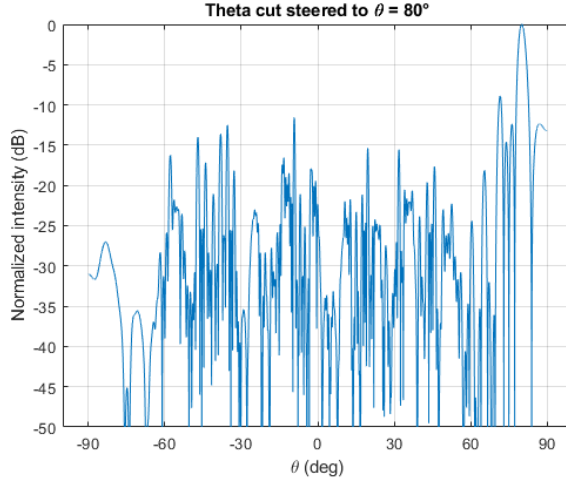


**Figure 4. 33: 2D pattern cuts for  $\theta_0 = 15^\circ, 30^\circ, 45^\circ, 60^\circ, \text{ and } 80^\circ$  (Rectangular SA)**

The BW gradually increases for larger angles of  $\theta_0$  but this can be compensated by increasing the element count or by making the element spacing larger. From our understanding, the steering range is virtually unaffected by aliasing, allowing for a  $\pm 80^\circ$  steering range. At angles past  $80^\circ$ , the ML starts to lose its shape, becoming undefinable. This is where we impose a limit on the steering range.

The performance of our planar SA design is compared with state-of-the-art integrated OPAs reported in the literature. Such designs include the works by D.Hutchinson et.al [33], Q.Wang et.al [18], and R.Fatemi et.al [36]. All these designs consist of planar array designs, mainly focused on increasing the steering range of the OPA. We categorize each work with the corresponding steering range found in each design within Table 4.2.

**Table 4. 2: Comparisons with State-of-the-Art OPA Steering Ranges**

	Steering Range
Hutchinson	$80^\circ$
Wang	$32.6^\circ$
Fatemi	$16^\circ$
Our work	$160^\circ$

## 4.4 Optimized Structure

From the previous sections, we can see that there is a ceiling imposed on the SL contrast at around 8-9 dB. These SLs can be seen in Fig. 4.34 near the ML. No matter which parameters change, their effect on the SL contrast at these two points is nil. To understand this phenomenon, we can recall the discuss had in Section 4.1.1 where we detailed how the final array pattern is formed. The two SL peaks near the ML are formed due to the overlapping of the ML of the unit cell over the GLs of the SA pattern.

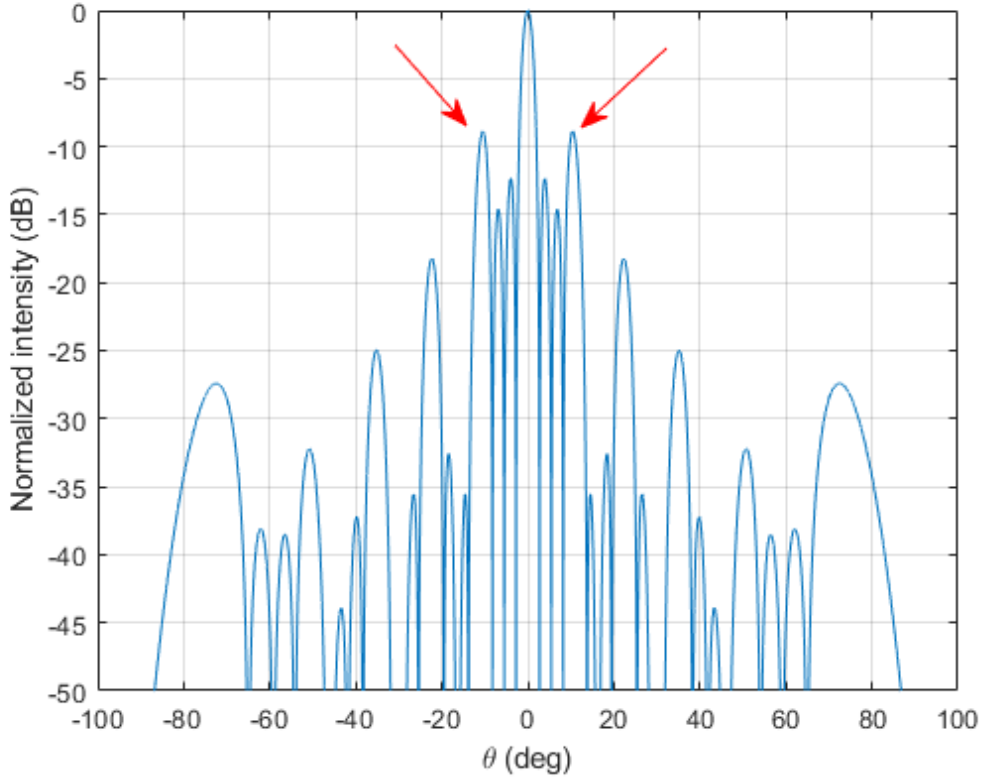


**Figure 4. 34: Theta cut for the rotated rectangular SA structure. There are always two SL peaks near the ML.**

Optimizing the structure by finding an optimal configuration of each unit cell parameter and SA parameter will not be done due to the limitations imposed by the SLs near the ML. Changing the elements after a certain point has little to no effect on decreasing those SLs. Instead, we will try to optimize the excitation amplitudes of each element,  $I_n$ , within the array.  $I_n$  can be seen in Eq. (3.1) and is normally equal to 1. However, now we will vary  $I_n$  from 0 to 1 to lower the overall SL contrast. Due to the complexity of this task, we will use the genetic algorithm (GA) which has been shown repeatedly to be very effective in finding an optimal solution.

The GA is a numerical optimization method that models evolution and genetic recombination to find an optimal solution. The working principle behind the GA lies in reconstructing the inputs of a problem into genes where the genes will be grouped into categories known as chromosomes. The GA then requires a function, here denoted as the cost function, to rank each chromosome. Natural selection will follow shortly after, with a condition to only select the best performing chromosomes. The natural selection process uses a probabilistic method where the highest probability is assigned to the most fit members. The surviving chromosomes then undergo a mating process which will share their DNA with their offspring's, continuing their lineage with the best performing genes. At the end of the mating process, mutations are induced within the population to help spread diversity. Then we continue into a new generation with the surviving population and repeat the same process for a desired number of generations. This whole process is illustrated in Fig. 4.35.

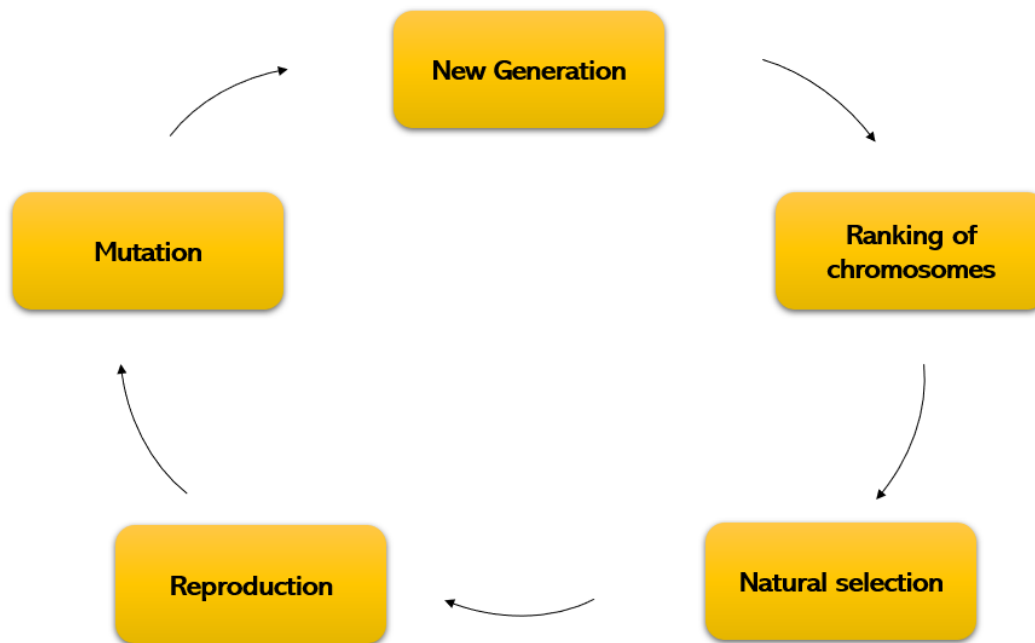


**Figure 4. 35: GA process**

Again, the main objective of the GA is to optimize  $I_n$ . Since the performance metric here is the SL contrast, we will represent the calculated SL contrast as our cost function to minimize. We will simulate a rectangular SA structure with  $N_r = N_c = 4 = N_{SA_r} = N_{SA_c} = 4$ ,  $d_x = d_y = 5\lambda = 7.77 \mu m$ , and  $\alpha = 10^\circ$ . We first choose to work with a structure that has a reasonable number of elements (256 elements) to see the

effectiveness in using the GA in this manner. We again select a larger element spacing to demonstrate the structures performance under large spacings. The structure and pattern cut are shown here in Fig. 4.36 to demonstrate how the pattern looks like without optimizing the element weights.

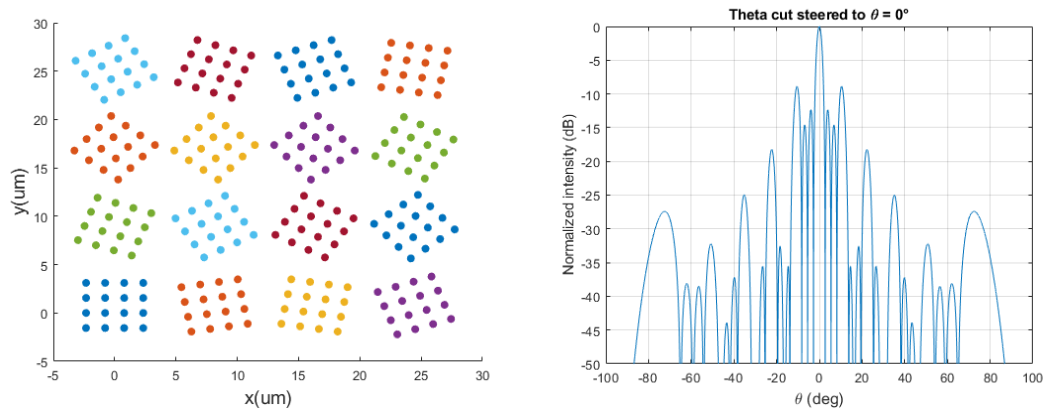


**Figure 4. 36: Non-optimized structure with pattern cut**

We run the GA for 100 generations, and we observe where the optimal solution lies by changing  $I_n$ . The cross-over rate of the GA here is equal to 1 and it represents the number of off-springs produced through crossover. We use the single-point crossover method which takes a slice from the gene of each parent and combines the two slices to form the offspring after crossover. The mutation rate of the GA is set to 0.1. We keep this low to ensure some diversity is present within the population but not too large where the GA would be on a random search.

We can see in the first plot of Fig. 4.37 that the GA is able to find a set of weights that gives a SL contrast near 12 dB. We can see that the trend is almost saturated by 100 generations, but we perform one more run with 200 generations to see if any more improvements can be found. The second plot of Fig. 4.37 demonstrates the run with 200 generations. We can see a very marginal improvement in dB from 100 to 200 generations, so we conclude the GA runs for the rectangular SA.

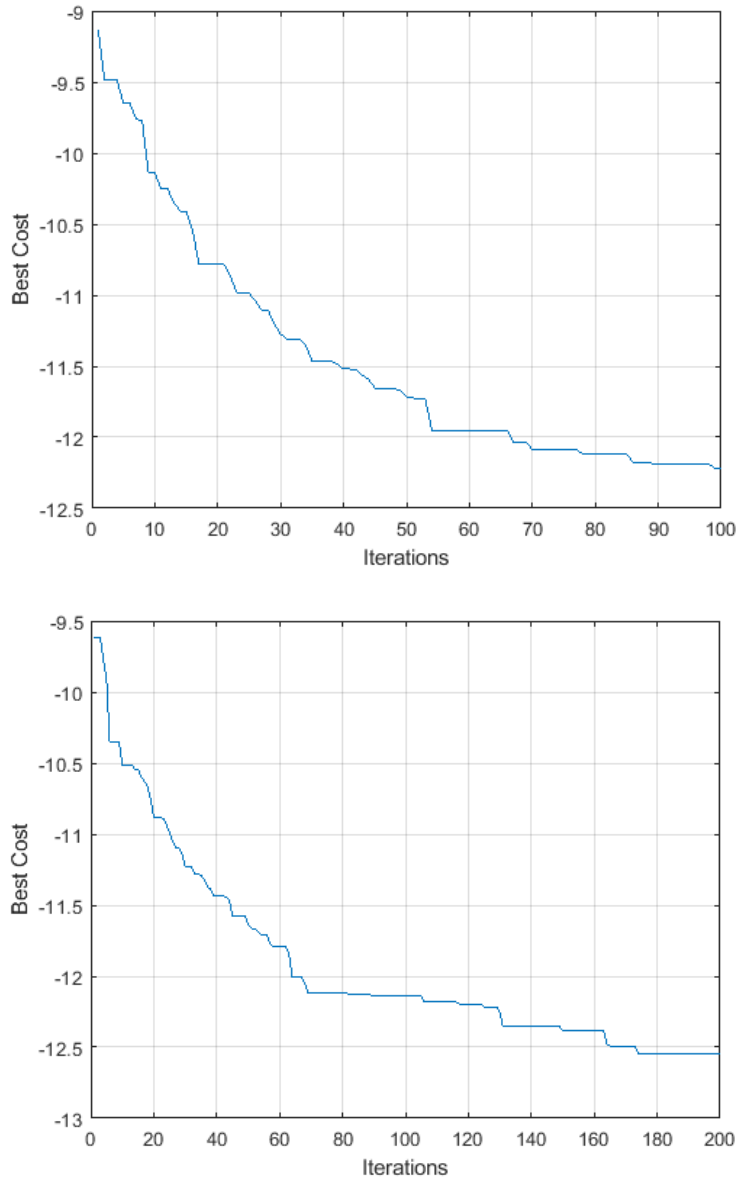


**Figure 4. 37: GA run for 100 and 200 generations respectively (Rectangular SA)**

Now using the weights found by the GA, we show the pattern cuts to demonstrate the difference between the non-optimized and optimized structures. We can see the two pattern cuts belonging to the non-optimized and optimized structures respectively in Fig. 4.38. The SLs near the ML have been lowered by close to 3dB without distorting the radiation pattern.

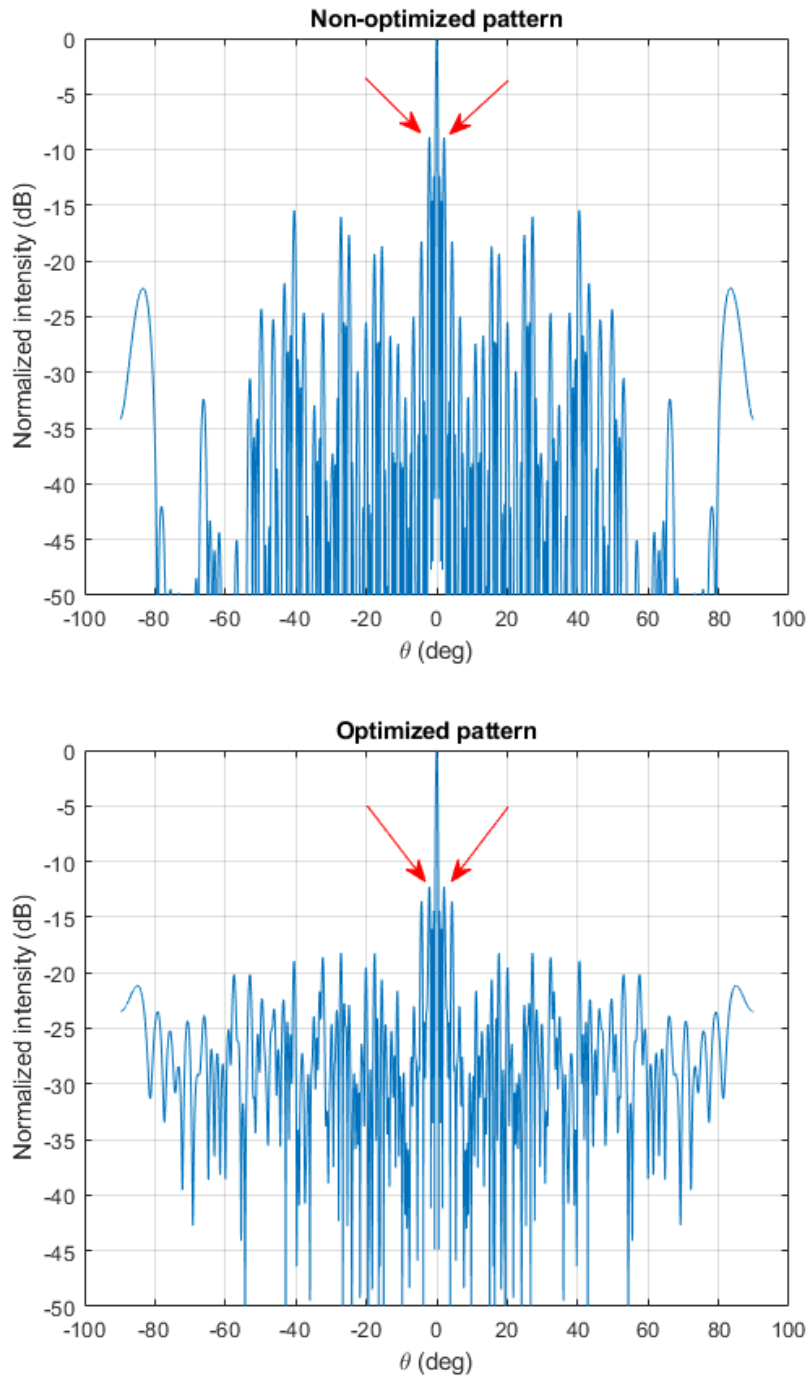


**Figure 4. 38: Non-optimized and optimized pattern cuts (Rectangular SA)**

The triangular SA lattice experienced the same issue of high SLs near the ML which was a consequence of the periodic SA spacing. We apply the same method of optimization on the triangular SA lattice to see what improvements can be made to the SL contrast by optimizing  $I_n$ . The same parameters used for the rectangular SA will be used for the triangular SA. Again, we start with 100 generations and see where the best solution lies at the end of the run. We can see the result of the 100 generation run in the

first plot of Fig. 4.39 where the best solution was near 13 dB. We simulate the GA once more, but now with 200 generation to see where the best solution is. We can see in the second plot of Fig. 4.39 that only a small improvement was found even though the number of generations was increased by two.

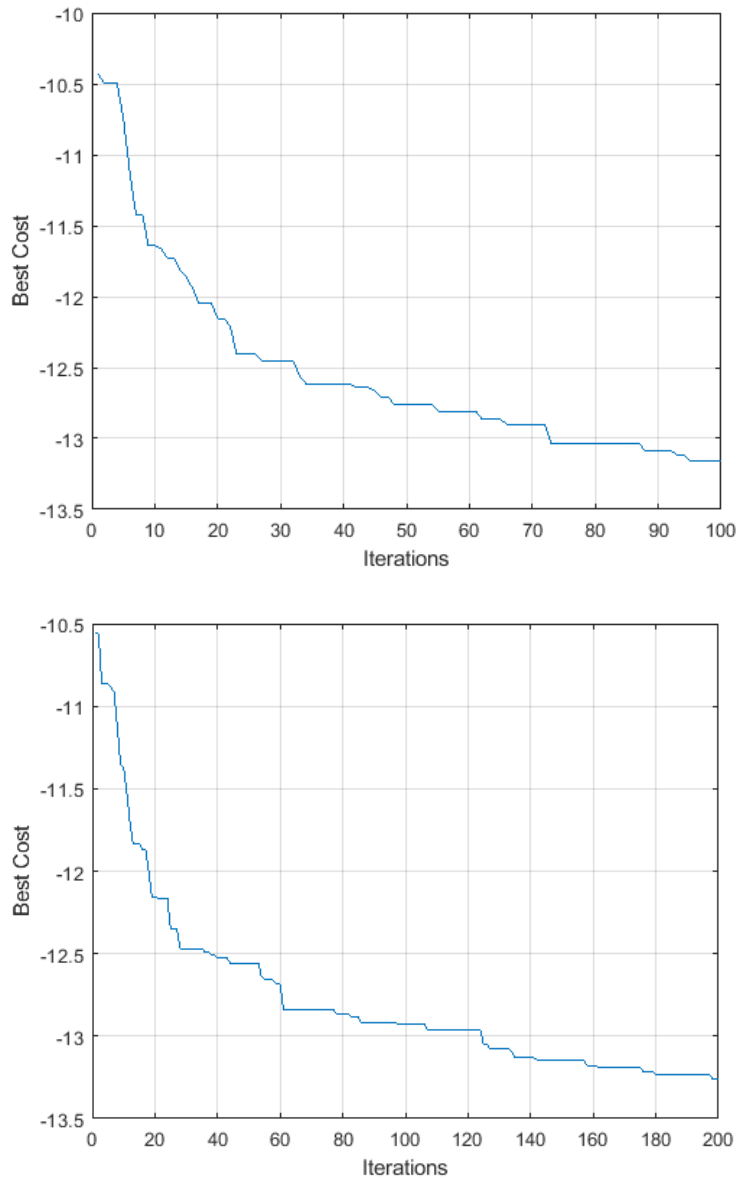


**Figure 4. 39: GA run for 100 and 200 generations respectively (Rectangular SA)**

The non-optimized and optimized pattern cuts are shown again to demonstrate the differences before and after applying the optimized weights. We can see both plotted in Fig. 4.40. One difference that was necessary is that the pattern cut was taken along  $\phi$  and not  $\theta$  due to how the SLs form around the ML. This is due to how the triangular symmetry arranges the SLs which was seen previously in Fig. 4.30.

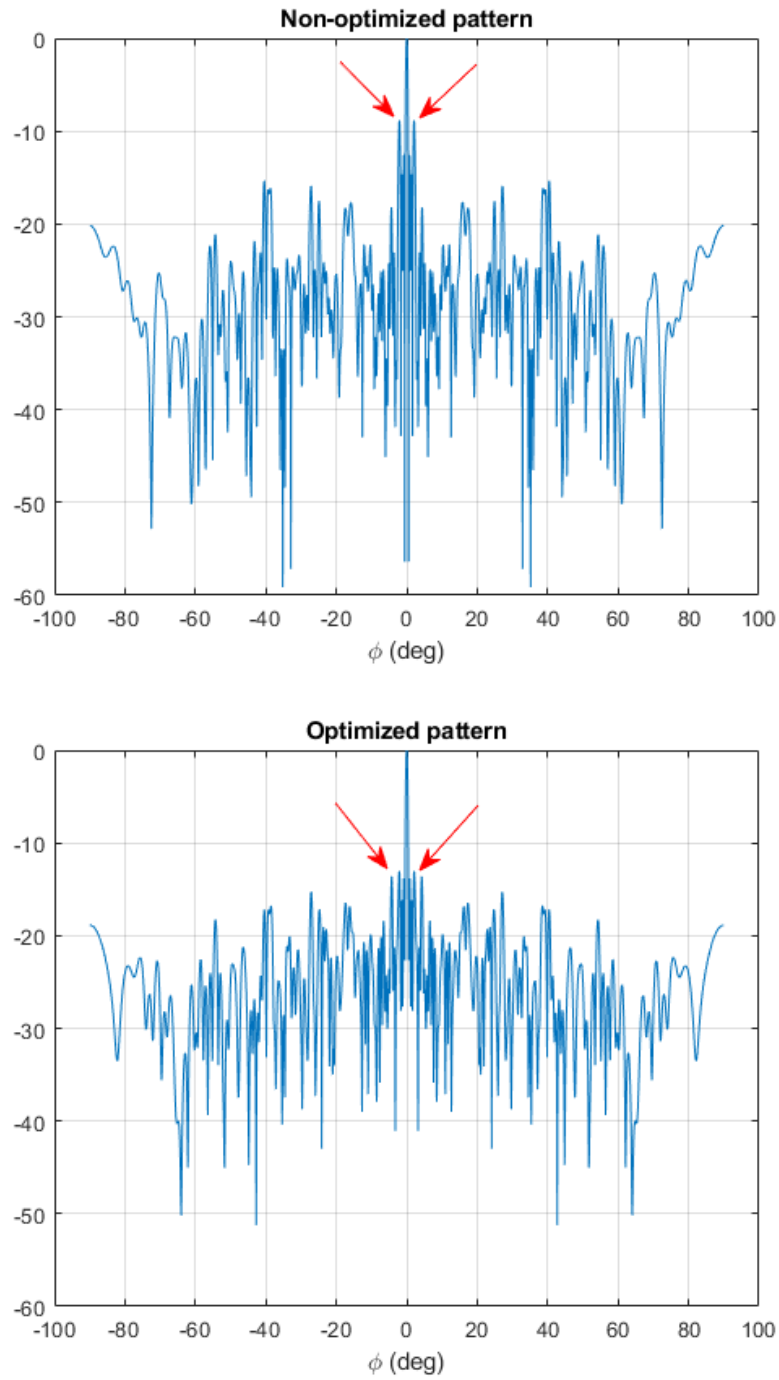


**Figure 4. 40: Non-optimized and optimized pattern cuts (Triangular SA)**

## 4.5 Summary

Within this chapter, we studied two planar SA designs which utilized two unit cells to see how their performance changed as we varied several of their design parameters. It was clear that several parameters, particular the SA spacing,  $D_x$  and  $D_y$ , and the rotation angle,  $\alpha$ , had the largest impact on controlling the SL contrast. The triangular SA lattice did achieve a slightly higher SL contrast, which was due how the lattice reconstructs the GL power into the SLs around the ML. We also compared a uniform rectangular array lattice with a rotated rectangular SA lattice to demonstrate the differences after rotation. It was clear that by using the rotated SA lattice, the problem of aliasing is nullified which greatly increases the steering range. To improve the SL contrast after rotation, we utilized the GA to optimize the element weights in each SA structure. This was shown to effectively reduce the SLs near the ML by a few dB. The rotated SA lattice has never seen an implementation within the optical domain. The findings within this chapter, particularly the greater element spacing allowed, show that the spacing limitations imposed on many OPA designs can be alleviated without sacrificing the steering range.

## Chapter 5 Circular Sub-Array Design

The content of this chapter comprises of the analysis of two circular sub-array designs, one composed of a rectangular unit cell array while the other uses a circular unit cell array. A circular SA arrangement is used for each unit cell which will be detailed in the beginning of each array section. Simulation results are obtained using MATLAB to calculate the SL contrast and BW which will be used to study the performance of each array. In the last section, a comparison will be conducted between the two unit cells to understand the differences between each array; another comparison will also be made between a single circular unit cell to the circular SA design.

### 5.1 Rectangular unit cell

#### 5.1.1 Design methodology

A rectangular planar array is selected as the unit cell lattice within this section as pictured in Fig. 5.1. The design parameters used to define the structure consists of the element spacing's ( $d_x$  and  $d_y$ ) and the number of rows/columns ( $N_r$  and  $N_c$ ).

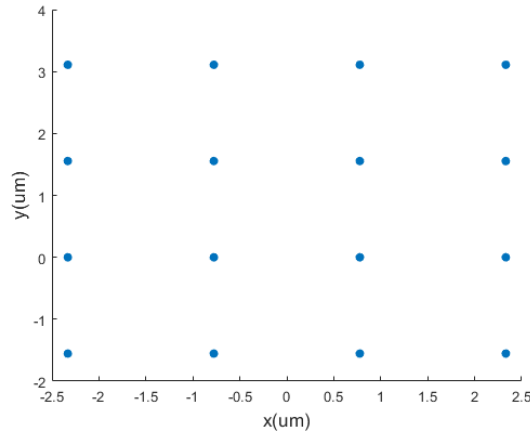


**Figure 5. 1: 4x4 rectangular unit cell lattice**

Now we consider the circular SA which rearranges the unit cells along the circumference of the SA ring. New design parameters are introduced including the radius of the ring ( $R_{SA}$ ), the number of unit cells in each ring ( $M_{SA}$ ), the number of SA rings ( $N_{SA}$ ), and the incremental radius between each SA ring ( $dr_{SA}$ ).  $R_{SA}$  and  $dr_{SA}$  are dependent on the unit cell parameters because they must accommodate the sizes of each unit cell to ensure no elements overlap. Using the rectangular unit cell,  $R_{SA}$  has the following definition

$$R_{SA} = M_{SA} * D_I / 2\pi + d_x + d_y \quad (5.1)$$

where  $D_l$  represents the diagonal length of the rectangular unit cell, as defined in Eq. (4.1). Similarly,  $dr_{SA}$  is defined as

$$dr_{SA} = 2 * l \quad (5.2)$$

where  $l$  represents the max length of the unit cell. If the length along one axis is greater, then that length will be chosen for Eq. (5.2). Once these parameters are defined, the SA structure can be established as seen in Fig. 5.2.

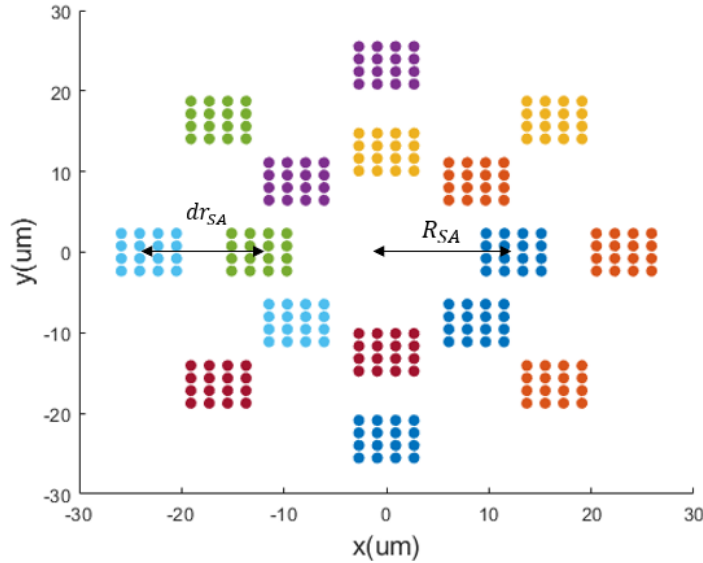


**Figure 5. 2: A circular SA design consisting of  $N_r = 4, N_c = 4, M_{SA} = 8$  and  $N_{SA} = 2$**

The next step of the design process involves applying the rotation method to the SA. Within this chapter, two rotation methods will be studied and compared to understand the affect each respective method has on the SL contrast and BW. The first rotation method used in this chapter is the rotation method studied in Ch.4; however, now each unit cell along the SA ring will have the following rotation angle ( $\alpha_n = 0 * \alpha, \pm 1 * \alpha, \pm 2 * \alpha, \pm 3 * \alpha, \dots$ ). The rotation angles,  $\alpha_n$ , are applied along the ring in a counterclockwise motion. This rotation method is reflected in Fig. 5.3.

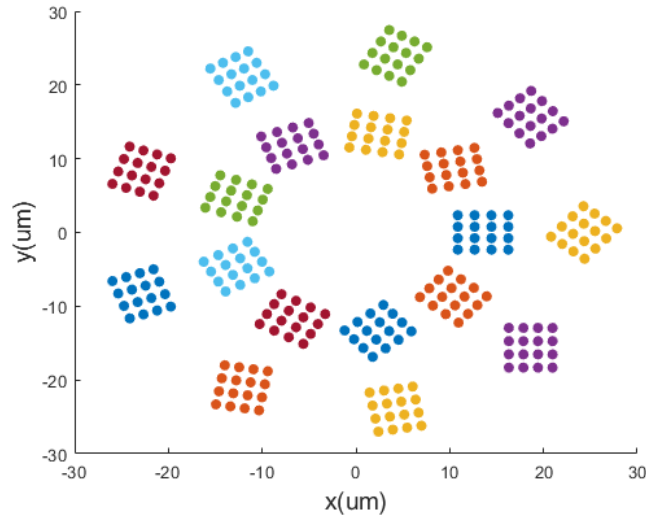


**Figure 5. 3: A circular SA design using rotation method #1**

The other rotation method used in this chapter will be denoted as the second rotation method. The main difference between this method involves the SA rings. The second rotation method follows similarly to the first rotation method where each unit cell along the SA ring has a rotation angle of angle ( $\alpha_n = 0 * \alpha, \pm 1 * \alpha, \pm 2 * \alpha, \pm 3 * \alpha, \dots$ ). Once the first SA ring is defined, each unit cell in all subsequent rings will have the exact rotation angle of the first ring. This rotation method is reflected in Fig. 5.4.

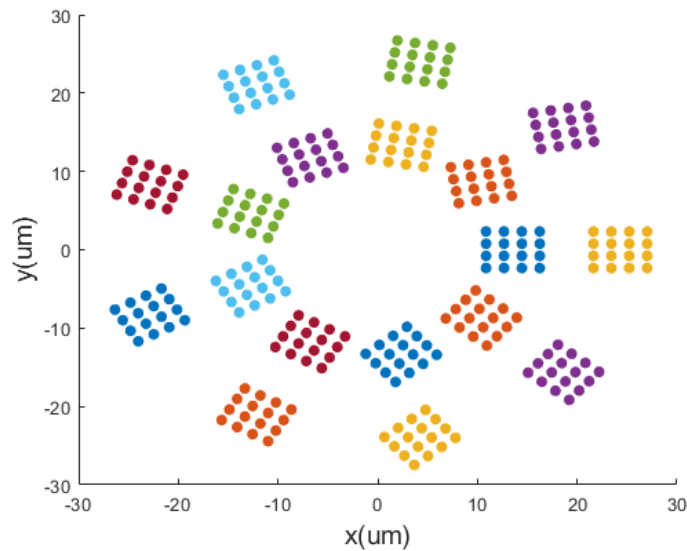


**Figure 5. 4: A circular SA design using rotation method #2**

## 5.1.2 Simulations

The elements used in this chapter have the same properties as in section 4.1.2. Using these elements, we will try to understand the impact of each design parameter on the array performance by calculating the SL contrast and BW. Both rotation methods will be studied to understand the differences each method imposes on the array performance. A comparison between the two will be highlighted at the end of this section, going over the major findings of each method.

There are seven main parameters that are studied for both rotation methods:  $N_r$ ,  $N_c$ ,  $d_y$  and  $d_z$  which define the unit cell and  $M_{SA}$ ,  $N_{SA}$ ,  $R_{SA}$ ,  $dr_{SA}$ , and  $\alpha$  which define the circular SA. To understand the effect of each parameter, we fix 5 of the 7 design parameters and study the impact of each parameter. The other two parameters,  $R_{SA}$  and  $dr_{SA}$ , are changed to an appropriate value to reflect the design trends. Some trends require  $R_{SA}$  and  $dr_{SA}$  to be at a fixed constant so that they don't change simultaneously with the parameter of interest. The parameters that change  $R_{SA}$  and  $dr_{SA}$  include  $N_r$ ,  $N_c$ ,  $d_x$ ,  $d_y$  and  $M_{SA}$ .

The following design is selected for the study:

- $N_r$  and  $N_c = 4$
- $d_x$  and  $d_y = 1 * \frac{2}{\sqrt{3}}\lambda = 1.79 \mu m$  and  $1 * \lambda = 1.55 \mu m$
- $M_{SA} = 9$
- $N_{SA} = 2$
- $\alpha = 10^\circ$

We first choose similar unit cell parameters as in Ch.4 to keep the study consistent. We choose to have  $M_{SA} = 9$  to ensure there are enough SAs along each ring to resemble a circular array and  $N_{SA} = 2$  to study the performance of a concentric circular SA. Finally, we choose a rotation angle  $\alpha$  for the same reasons in Ch.4.

We first study the two unit cell parameters,  $N_r$  and  $N_c$ . To properly account for only these two parameters,  $R_{SA}$  and  $dr_{SA}$  are fixed at  $75 \mu m$  and  $60 \mu m$  respectively. The impact of the two-unit cell parameters,  $N_r$  and  $N_c$  have on the SL contrast and BW are demonstrated in Fig. 5.5 and Fig 5.6 respectively. Both share a similar effect on the two parameters where the SL contrast increases sharply, and the BW remains constant. The

SL contrast trend can be understood by the impact of the relative positions of each SA to their respective neighbors. As the size of the SA increases by increasing  $N_r$  or  $N_c$ , the elements become closer which has a considerable impact in improving the SL contrast.

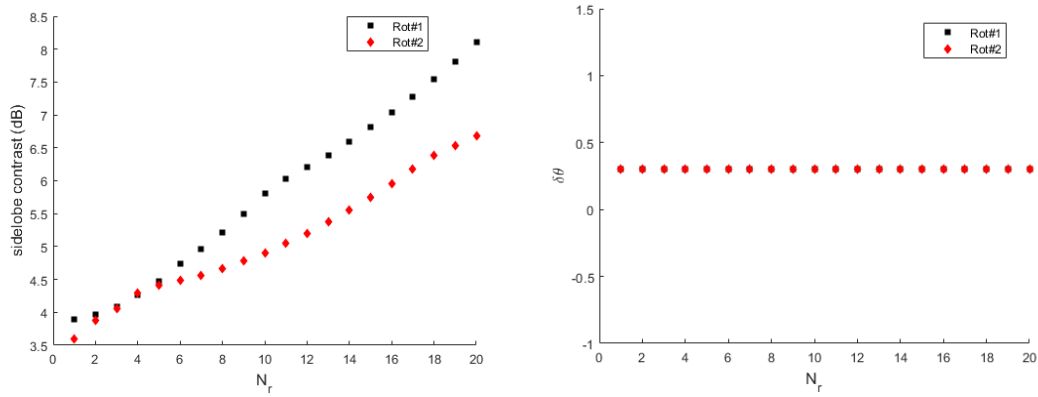


**Figure 5. 5: Impact of  $N_r$  on the SL contrast and BW**

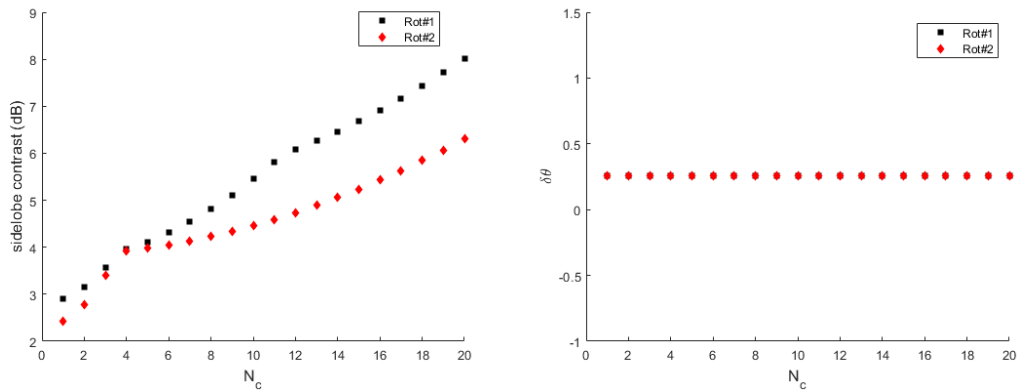


**Figure 5. 6: Impact of  $N_c$  on the SL contrast and BW**

The BW remains unchanged for every value of  $N_r$  and  $N_c$ . This is primarily due to the considerable impact increasing the radius,  $R_{SA}$ , has in decreasing the SL contrast and BW. The SA radius is quite large @  $R_{SA} = 75 \mu m$ , so the SAs are extremely far apart from each other which results in a very small BW. Any small change to the size of the unit cell here does not impact the BW since the radius is much larger. Fig. 5.7 demonstrates the large discrepancy between unit cell size and radius.

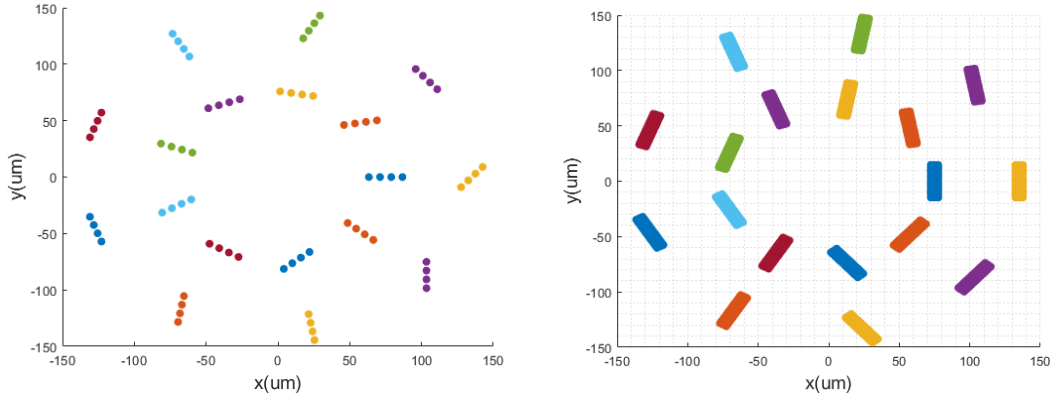


**Figure 5. 7: Array Structure for  $N_r = 1$  and  $20$  @  $R_{SA} = 75 \mu\text{m}$  and  $dr_{SA} = 60 \mu\text{m}$**

The next parameter of interest is  $N_{SA}$ . The impact on the SL contrast and BW is demonstrated in Fig. 5.8. There is a large increase in dB from  $N_{SA} = 1$  to 2 but the remaining part of the trend shows a small gradual change in dB. The reason for this small change is due to the value of  $M_{SA}$  chosen for this design. We choose  $M_{SA} = 7$  but if we increase this to a higher value, then we can see a larger increase in dB for an increasing  $N_{SA}$ . We depict this in Fig. 5.9 where we select  $M_{SA} = 15$  and increase  $N_{SA}$ . The improvement in dB is expected as the choice between the number of elements per ring and the number of concentric rings has been studied in the past for improving the SL contrast in circular arrays [47,48].

The BW does see a decrease as  $N_{SA}$  increases. This is primarily due to two reasons. The first reason is from the increase in total elements within the array. The second, and more impactful reason, is that the total size of the array increases. We know that increasing the number of rings increases the total size of the array, thus reducing the BW. We can see a difference between how many degrees the BW changes by in Fig. 5.8 and Fig. 5.9 which is due to the differences in  $R_{SA}$  from selecting  $M_{SA} = 9$  and 15.

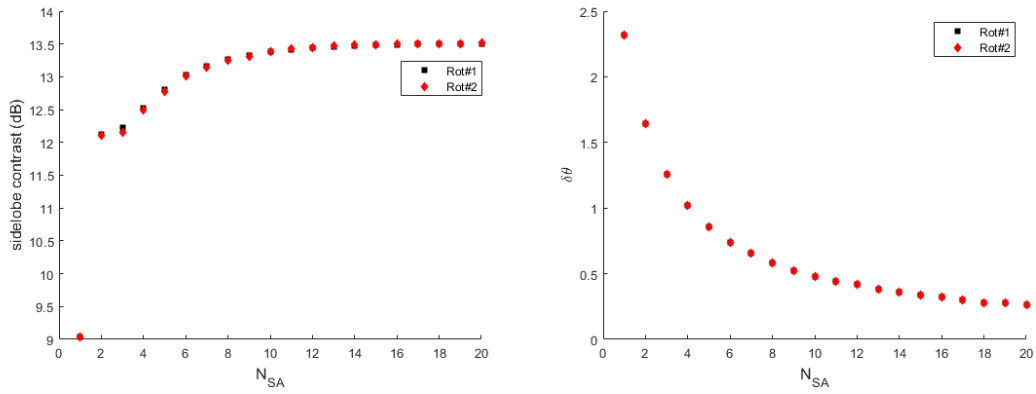


**Figure 5. 8: Impact of  $N_{SA}$  on the SL contrast and BW for  $M_{SA} = 9$**

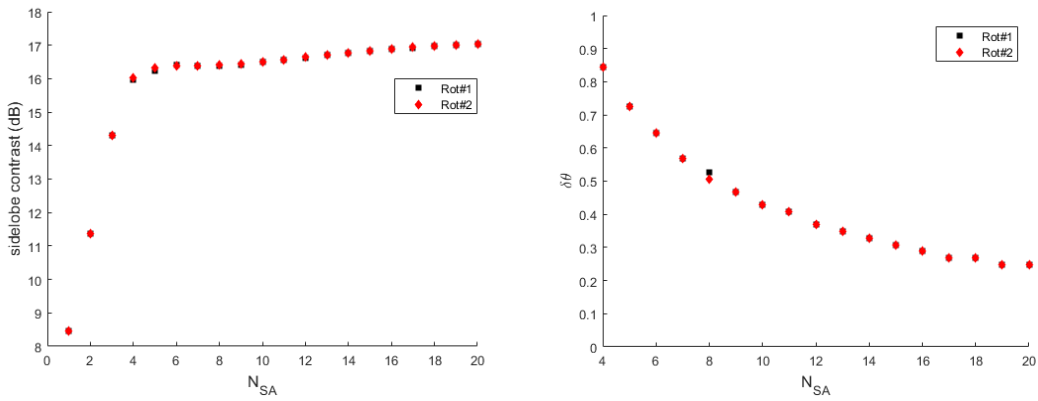


**Figure 5. 9: Impact of  $N_{SA}$  on the SL contrast and BW for  $M_{SA} = 15$**

The impact of  $M_{SA}$  is studied next. It can be seen in Fig. 5.10 that  $M_{SA}$  greatly increases the SL contrast. The SL contrast steadily increases until  $M_{SA} = 11$  where after this point the trend saturates. This gives good insight into optimizing the design as the trend signifies that a higher SL contrast is achieved when  $M_{SA}$  is larger.

The beamwidth is seen to have a negligible change. This can again be attributed to the selection for  $R_{SA}$  where  $R_{SA} = 30 \mu m$ .

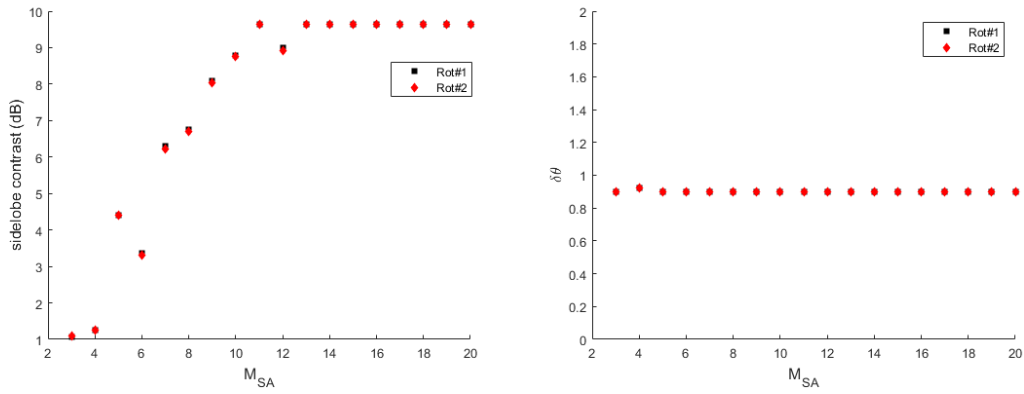


**Figure 5. 10: Impact of  $M_{SA}$  on the SL contrast and BW**

The next parameters of interest are  $d_x$  and  $d_y$ . It is seen in Fig 5.11 that increasing  $d_x$  and  $d_y$  greatly increase the SL contrast as both spacing's become larger in  $\mu m$ . This shows great promise because having a larger element spacing without sacrificing the SL contrast will ease the OPA design restrictions that are limited by the harsh spacing requirements.

The radius and incremental radius chosen here ( $R_{SA} = 110 \mu m$  and  $dr_{SA} = 90 \mu m$ ) were chosen to reflect the greatest  $d_x$  and  $d_y$  in the trend. This can explain why the BW sees little to no change over the whole range because of the stark contrast between unit cell spacing and the SA radius and incremental radius. Fig. 5.12 reflects the array structure change from  $d_x = 1.79 \mu m$  to  $d_x = 14.36 \mu m$ .

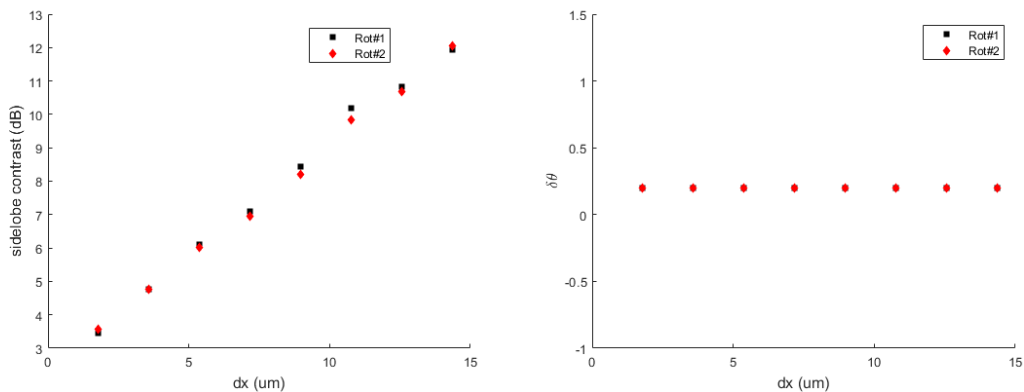


**Figure 5. 11: Impact of  $d_x$  and  $d_y$  on the SL contrast and BW**

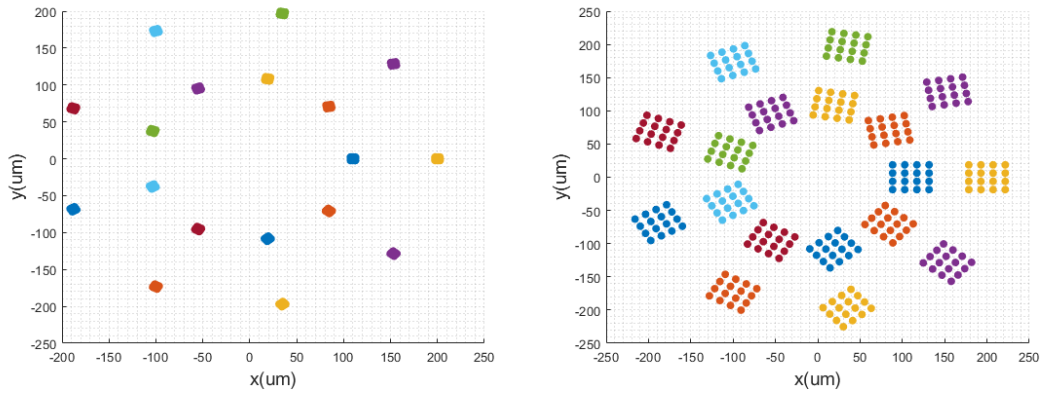


**Figure 5. 12: Array structure for  $R_{SA} = 110 \mu m$  and  $dr_{SA} = 90 \mu m$  when  $d_x = 1 * \frac{2}{\sqrt{3}} \lambda (1.79 \mu m)$  and  $d_x = 8 * \frac{2}{\sqrt{3}} \lambda (14.36 \mu m)$**

The next parameters of interest are the ring radius,  $R_{SA}$ , and the incremental ring radius,  $dr_{SA}$ . Starting with the former, increasing  $R_{SA}$  can be seen to have a large control in decreasing the SL contrast and BW. An exponential trend downwards is seen in Fig. 5.13 for both trends, emphasizing the impact  $R_{SA}$  has on the array's performance. Up until  $40 \mu m$ , the SL contrast decreases by 1 dB for every  $5 \mu m$  step increase.

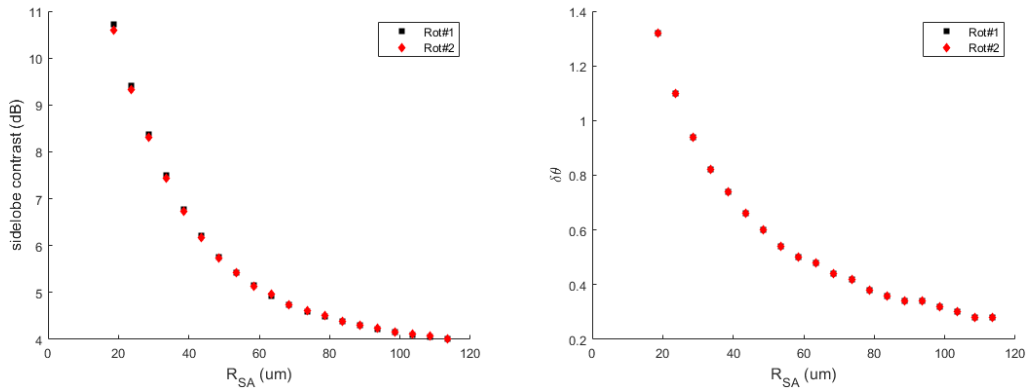


**Figure 5. 13: Impact of  $R_{SA}$  on the SL contrast and BW**

The beamwidth becoming smaller can be attributed to the larger spacing between SAs along each ring as seen in Fig 5.14.

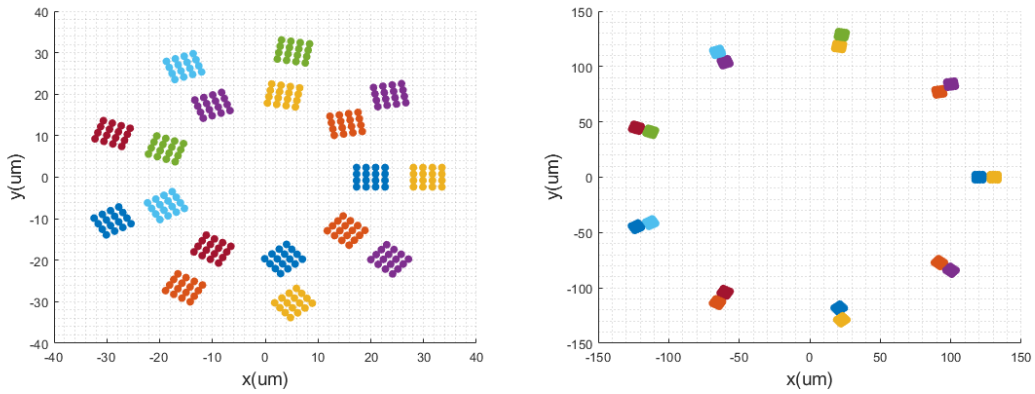


**Figure 5. 14: Larger SA spacing due to the increased ring radius,  $R_{SA}$**

The next parameter,  $dr_{SA}$ , is seen to have a similar impact on the SL contrast and BW compared to  $R_{SA}$ . An interesting trend is highlighted in Fig. 5.15., where a decrease in the SL contrast is apparent except for at one point near  $40 \mu m$ . The most probable cause for this increase can be obtained from understanding the effect that the incremental radius has on a single concentric ring array as seen in Fig. 5.16. In this case, when  $dr$  increases, an increasing exponential trend can be observed in the first few points. Then we see a periodic curve for the remaining portion of trend within Fig. 5.16 which is understood from the GL formation within the circular unit cell. Changing the incremental radius alters the position where the GL forms within the pattern, thus changing the SL contrast. A detailed investigation of GL formation within circular arrays is shown in [51].

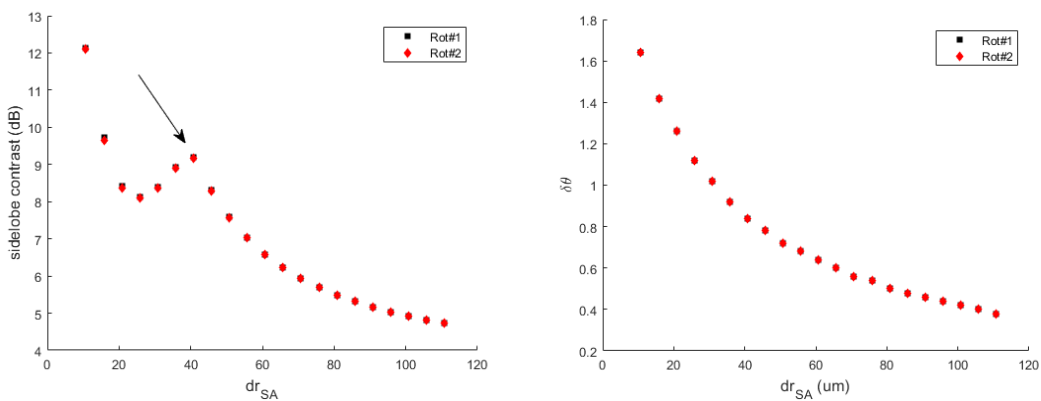


**Figure 5. 15: Impact of  $dr_{SA}$  on the SL contrast and BW**

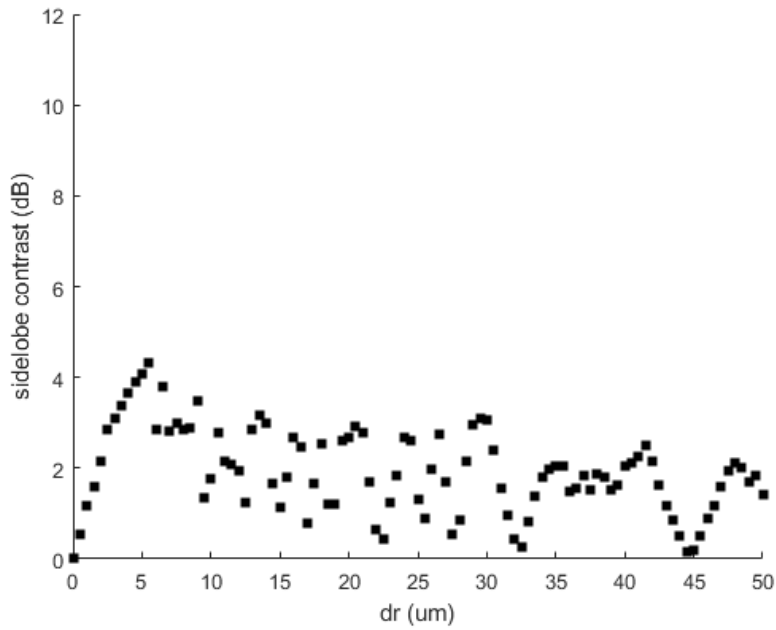


**Figure 5. 16: Impact of  $dr$  on a single circular unit cell**

The final parameter of interest is the rotation angle,  $\alpha$ . The rotation angle has a considerable effect on the sidelobe contrast. For the inter-element spacing chosen, it is apparent that there is significant power being radiated in four directions around the main lobe when  $\alpha = 0^\circ$  as seen in Fig. 5.17. This is expected when using rectangular arrays due to the introduction of GLs in the radiation pattern. We can also see in Fig. 5.17, the reduction of power in those four directions due to rotation when  $\alpha = 10^\circ$ .

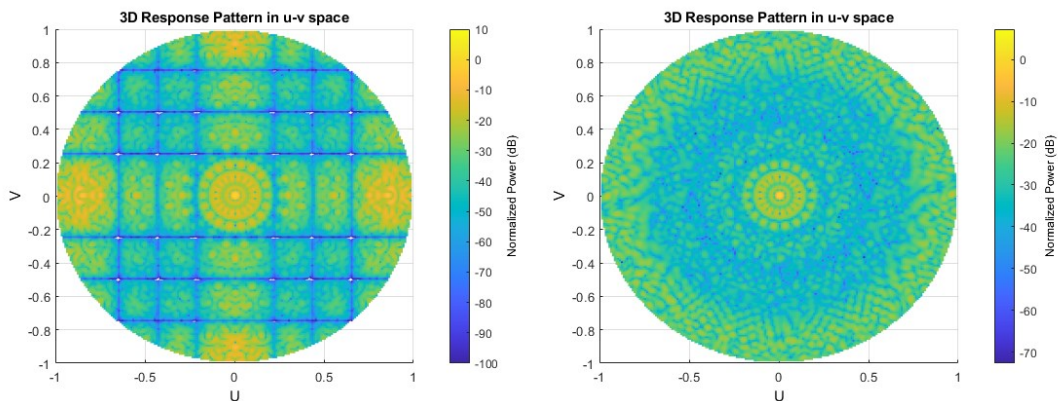


**Figure 5. 17: Radiation pattern when  $\alpha = 0^\circ$  and  $10^\circ$  respectively**

Once the rotation angle is increased beyond  $0^\circ$ , the SL contrast sees a considerable increase in dB as seen in Fig. 5.18. The rotation angle causes the redistribution of each unit cells GLs over the whole pattern region, effectively reducing the power radiated in

those four directions. For the whole range, the SL contrast remains consistent at around 12 dB for both rotation methods until near  $\alpha = 90^\circ$  where the SL contrast decreases due to the rotational symmetry of the rectangular unit cells.

The BW is not considered as the rotation angle has no effect on the BW.

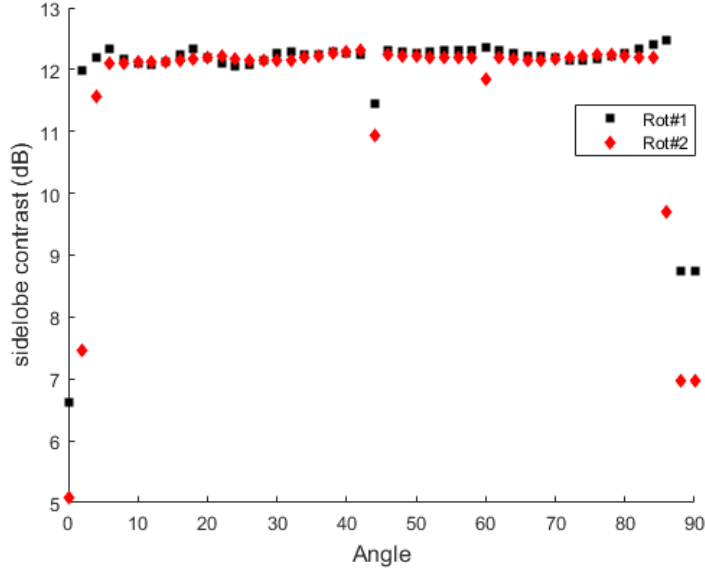


**Figure 5.18: Impact of  $\alpha$  on SL contrast**

The study of the design parameters responsible for the circular arrangement of rectangular unit cells demonstrates a few key trends that greatly impact the SL contrast. Increasing  $R_{SA}$  and  $dr_{SA}$  contributed to a large decrease in the SL contrast; it is clear that the relative distances between each unit cell along the circumference of each ring has the greatest effect in degrading the SL contrast and both  $R_{SA}$  and  $dr_{SA}$  affect this distance. In contrast to these parameters that decreased the SL contrast, both  $M_{SA}$  and  $N_{SA}$  were found to greatly increase the SL contrast. Therefore, emphasizing the choice in these parameters are key in designing an efficient structure.

The two rotation methods studied in this section can be seen to share a similar trend line in almost all figures. There are no discrepancies in the BW since the rotation angle has no effect on increasing the distances or sizes of the array. The main difference seen between the two rotation methods is highlighted in the impact of  $N_r$  and  $N_c$ . It was evident in Fig. 5.5 and Fig. 5.6 that the SL contrast was equivalent for both rotation methods up until the point where  $N_r = N_c = 4$ ; after this point is where the discrepancy emerges. Therefore, the SL contrast trends remained consistent between

the two rotation methods for all other parameters as the simulated design used a rectangular unit cell with  $N_r = N_c = 4$ .

The 2D UV map of the radiation pattern shown in Fig. 5.19 illustrates the differences between the two rotation methods. The radiation pattern is more evenly distributed for the first rotation method while there is more constructive interference along one direction for the second rotation method. The cause of this can be understood from the structure as  $N_r$  or  $N_c$  increases.

When  $N_r$  or  $N_c$  increases, the unit cells start to have a large extent of elements along one axis depending on if  $N_r$  or  $N_c$  increases. This is shown in Fig. 5.20 where both rotation methods are applied to a structure with  $N_r = 15$ . It's apparent that the extent of elements along one axis is amplified with the second rotation method. This causes there to be more constructive interference along one direction. The first rotation method does not experience this effect since each unit cell has its own unique orientation.

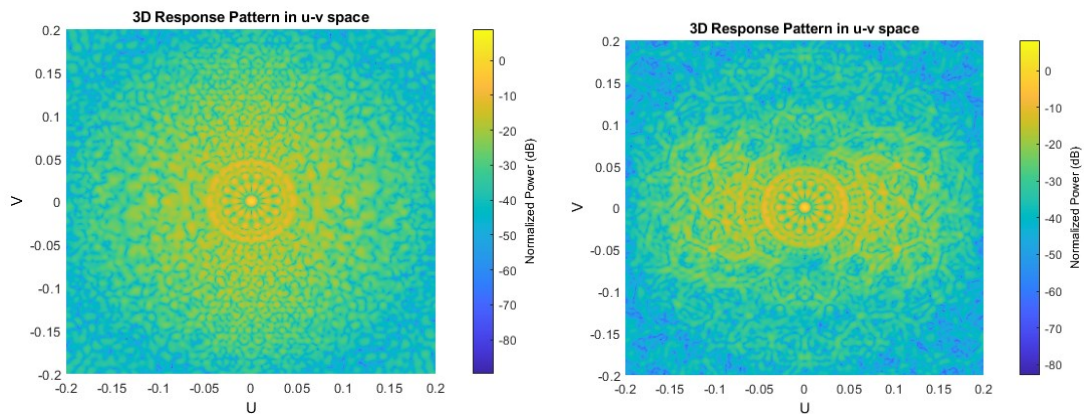


**Figure 5.19: 2D UV pattern for Rot #1 and #2 respectively for  $N_r = 15$**

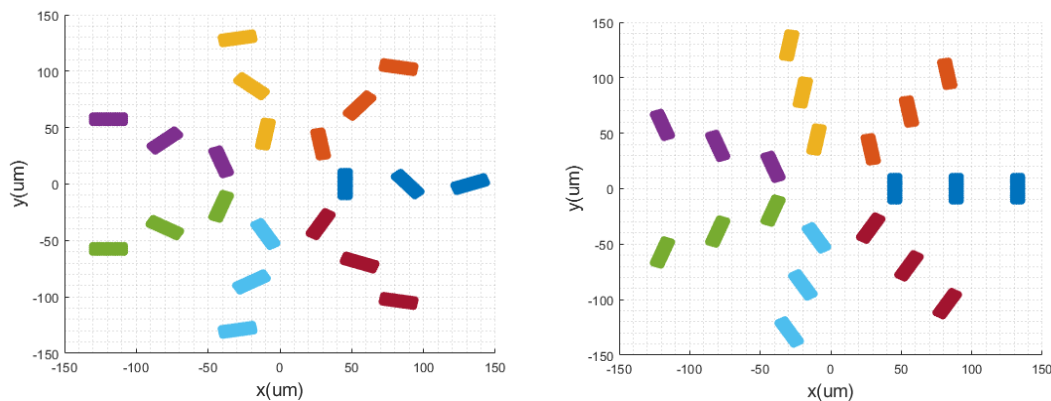


**Figure 5.20: Array structure for Rot #1 and #2 respectively for  $N_r = 15$**

The differences in the radiation pattern between increasing  $N_r$  and  $N_c$  is highlighted in Fig. 5.21. We can see how the constructive interference changes directions due to increasing either  $N_r$  or  $N_c$  respectively in Fig. 5.22.

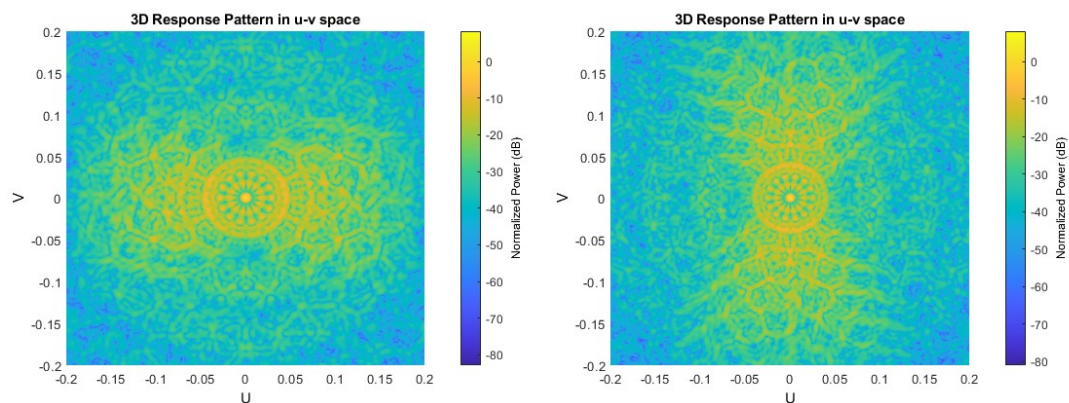


**Figure 5. 21: 2D UV pattern for Rot #2 when  $N_r = 15$  and  $N_c = 15$  respectively**

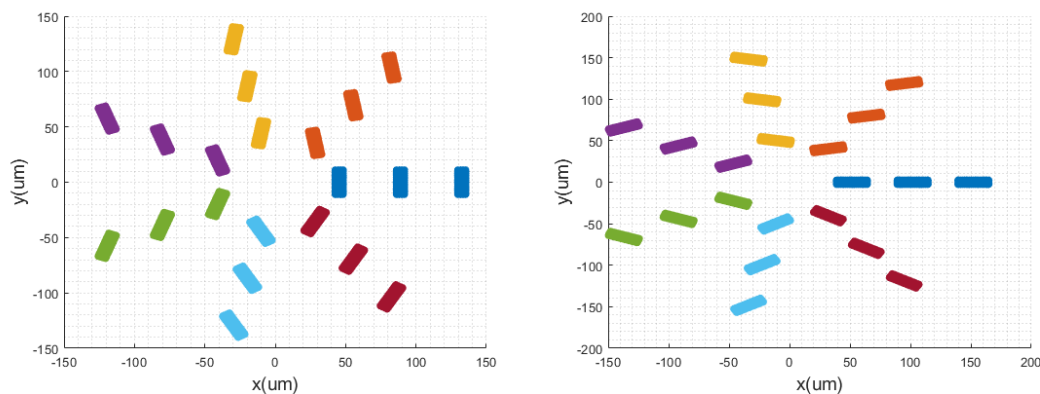


**Figure 5. 22: Array structure  $N_r = 15$  and  $N_c = 15$  respectively**

### 5.1.3 Optimizations using the Genetic Algorithm

In the previous section, we worked with a fixed design to better understand the implications each design parameter has on the array performance. It was seen that the choice in several parameters is critical in achieving an optimized design. Using larger values for  $M_{SA}$  and  $N_{SA}$  can greatly increase the SL contrast while minimizing  $R_{SA}$  and  $dr_{SA}$  is key to keep the SL contrast from degrading. Other parameters like the unit cell spacing must also be chosen carefully regarding OPA design to account for device spacing and routing.

The GA will be used to optimize the structural parameters of our unit cell and SA parameters. Due to the number of possible combinations of structures and the length of computational time an exhaustive search would require, we use the GA to find an optimized structure. Here we will mimic the genes of the GA as our unit cell rows/column parameters,  $N_r$  and  $N_c$ , our SA parameters,  $M_{SA}$  and  $N_{SA}$ , and finally our rotation angle  $\alpha$ . We also set the unit cell spacing to,  $d_x = 5\lambda$  ( $7.77 \mu\text{m}$ ) and  $d_y = 5\lambda$  ( $7.77 \mu\text{m}$ ) to demonstrate the practicality of the design in terms of the element spacing. For an OPA to work well, enough space must be accommodated to ensure minimal cross-talk. Therefore, we will have 5 genes per chromosome within our population. Once the chromosomes are defined, we will calculate the SL contrast for each chromosome and rank them from highest to lowest. Again, the SL contrast is represented as the cost function. The following ranges for each parameter will be used within each chromosome:

- $N_r = 1:6$
- $N_c = 1:6$
- $M_{SA} = 3:20$
- $N_{SA} = 1:10$
- $\alpha = 0^\circ:90^\circ$

We first impose an element threshold of around 500 elements for our optimization process. We start with 50 generations in our GA and see if and where convergence occurs. If convergence isn't clear, we then increase the number of generations by two to see if the GA converges. In the cross-over process, we utilize single-point crossover and set the crossover rate to 1. The mutation rate is set to 0.1 which will alter the genes of some chromosomes randomly to ensure diversity is present within the population. Starting with our first GA run, we can see the convergence trend plotted in Fig. 5.23. The top-ranking chromosome from each generation is plotted along the y-axis for each run. Throughout both runs, the GA gradually finds a better solution over each generation. We can see that the GA converges near 16.5 dB quite quickly and remains at this cost for the remaining generations. The structure that corresponds with this cost has the following parameters:  $N_r = 1$ ,  $N_c = 4$ ,  $M_{SA} = 15$ ,  $N_{SA} = 8$ , and  $\alpha = 17^\circ$ .

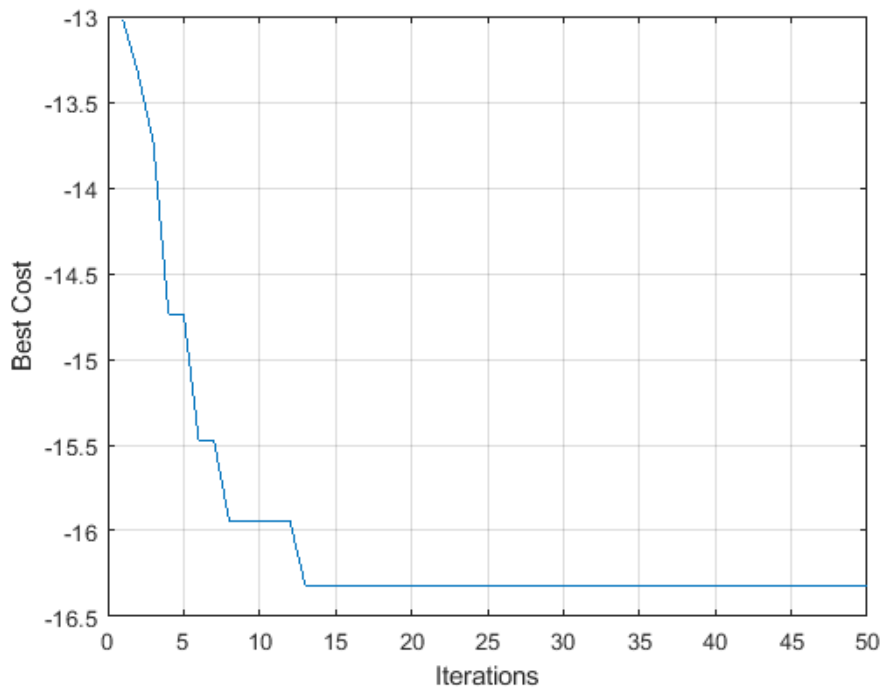


**Figure 5.23: Generation plot for Run 1**

To understand how consistent the optimal structure found by the GA is, we will increase the number of generations to 100. By increasing the number of generations by two, we can give the GA more time to determine if convergence is met at the best result. We can see the first generation plot in Fig. 5.24 that corresponds with these new changes. Now the convergence lies very close to 17 dB but we do see some small improvements near the 100<sup>th</sup> generation so we again increased the number of generations to 200 to better see where convergence occurs and how long it lasts. The second plot in Fig. 5.24 shows the generation plot when the number of generations is 200. We observe that the same point of convergence found prior is discovered earlier in the trend but there are no further improvements to the cost. The structure found has the following configuration:  $N_r = 2, N_c = 2, M_{SA} = 17, N_{SA} = 7$ , and  $\alpha = 68^\circ$ .

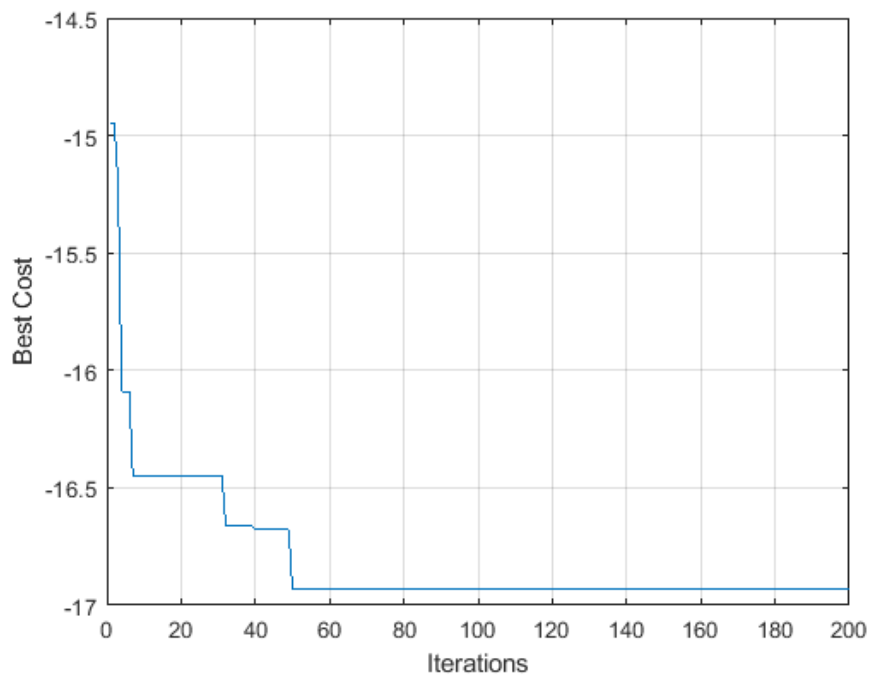
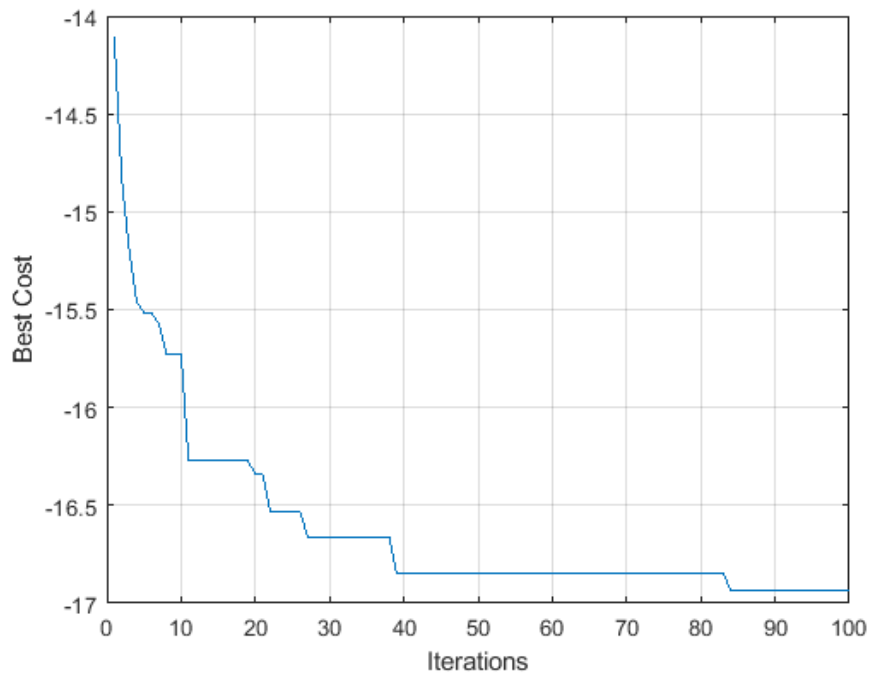


**Figure 5. 24: Generation plot for 100 generations and 200 generations**

Our next use of the GA involves the same processes, but we increase the element threshold to 1000. With the increased element threshold, we will also increase the ranges of the SA parameters,  $M_{SA}$  and  $N_{SA}$ , to 3:25 and 1:15 respectively. Plotted in Fig. 5.25 is the convergence trend over 50 generations. By increasing the element threshold and ranges, the GA was able to find structures that performed better than the previous limit of 500 elements. The GA converges near 19 dB which belongs to the structure with the following parameters:  $N_r = 2, N_c = 3, M_{SA} = 22, N_{SA} = 7$ , and  $\alpha = 39^\circ$ .

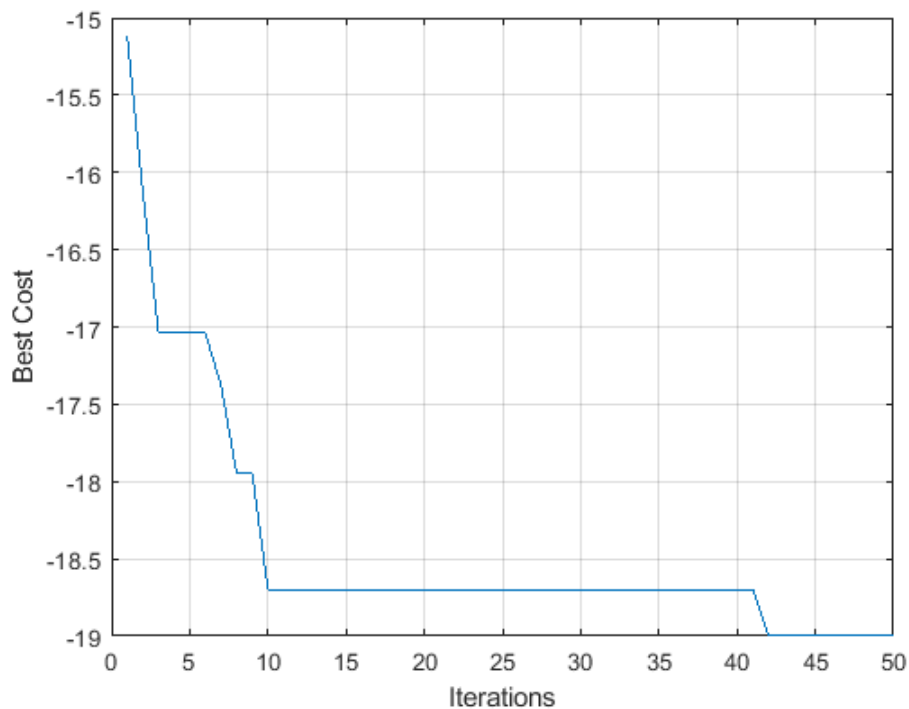


**Figure 5. 25: Generation plot for the 1000 element threshold**

To finish with the optimization process, we extend the length of the GA to 200 generations to see if convergence is met for a suitable amount of time near 19 dB. We choose 200 generations here due to the number of possible structures with the larger element threshold. The results of this run are plotted in Fig. 5.26. Convergence is met near 100 generations and no further improvements are found for the remaining generations. The best performing structure found had the following configuration:  $N_r = 1, N_c = 4, M_{SA} = 23, N_{SA} = 10$ , and  $\alpha = 62^\circ$ . We can conclude from this section that the performance of the circular SA structure is improved dramatically as both  $M_{SA}$  and  $N_{SA}$  are increased.

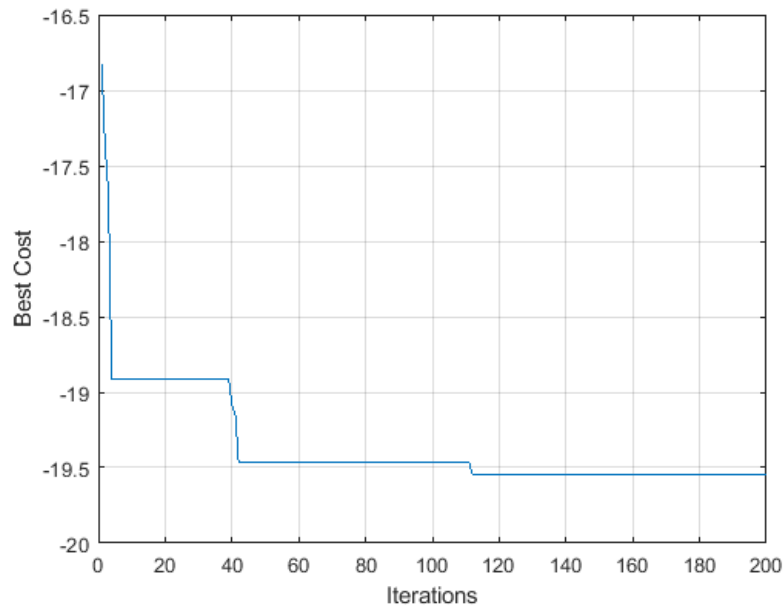


**Figure 5. 26: Generation plot for 200 generations (1000 element threshold)**

## 5.2 Circular unit cell

### 5.2.1 Design methodology

A circular array is selected as the unit cell lattice within this section as pictured in Fig. 5.27. The design parameters used to define the structure consists of  $M$ , the number of elements in one ring,  $N$ , the number of rings in each unit cell,  $R_{unit}$ , the radius of the first ring in each unit cell, and  $dr_{unit}$ , the incremental radius between each ring.

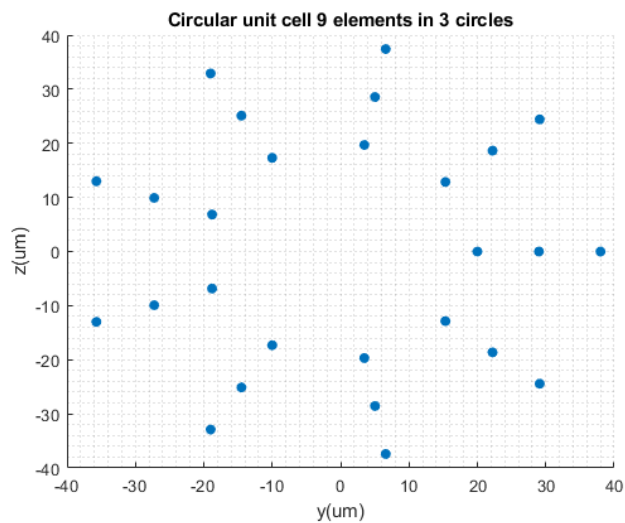


**Figure 5. 27: Circular unit cell lattice with  $M = 9, N = 3$**

Again, the circular SA lattice is considered, re-organizing each circular unit cell along a circumference defined by the circular SA radius. The same design parameters previously are used here: the radius of the SA ring ( $R_{SA}$ ), the number of unit cells in each SA ring ( $M_{SA}$ ), the number of SA rings ( $N_{SA}$ ), and the incremental radius between each SA ring ( $dr_{SA}$ ). The one difference between the design formulation is the definition of the SA ring radius and SA incremental radius,  $R_{SA}$  and  $dr_{SA}$  respectively. They are defined as:

$$R_{SA} = \frac{M_{SA} * R_{unit_n}}{2} \quad (5.3)$$

$$dr_{SA} = 2 * R_{unit_n} + dr_{unit} \quad (5.4)$$

where  $R_{unit_n}$  is the radius of the  $N^{th}$  unit cell ring. Once the SA design parameters are chosen, the array structure can be defined as seen in Fig. 5.28. Finally, either the first or second rotation method is chosen as shown in section 5.1.1.

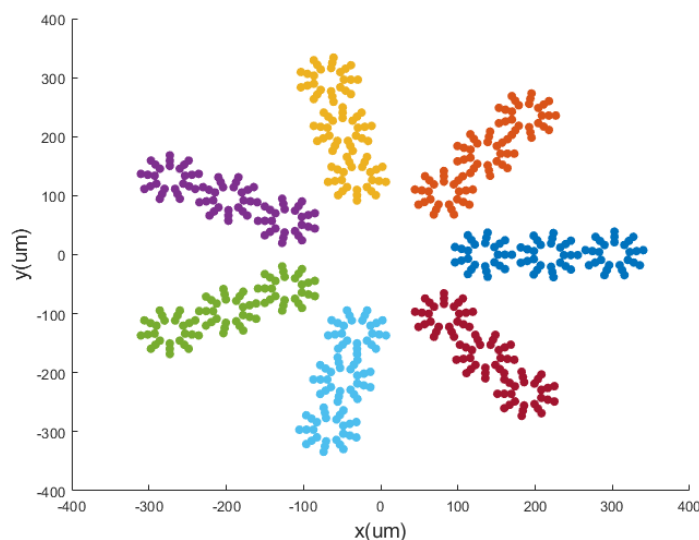


**Figure 5. 28: Circular SA lattice with  $M = 9$ ,  $N = 3$ ,  $M_{SA} = 7$  and  $N_{SA} = 3$**

## 5.2.2 Simulations

The elements considered in this section are identical to section 5.1.2. Like before, the main goal will be to study the circular unit cell array performance when rearranged into a circular SA. The angular BW and SL contrast will be used to judge the arrays performance for both rotation methods.

There are nine design parameters to consider. Four belong to the unit cell including  $M, N, R_{unit}$  and  $dr_{unit}$  while the other five belong to the SA including  $M_{SA}, N_{SA}, R_{SA}, dr_{SA}$  and  $\alpha$ .

The following design is selected for the study:

- $M, N = 5, 3$
- $M_{SA}, N_{SA} = 7, 3$
- $R_{unit} = 20 \mu m$
- $dr_{unit} = 9 \mu m$
- $\alpha = 10^\circ$

The last two parameters,  $R_{SA}, dr_{SA}$  are not fixed due to the definitions changing to reflect each design trend.

The first parameter of interest is  $M$ , representing the number of elements in each ring within the unit cell. It's apparent from Fig. 5.29 that increasing  $M$  has almost no change on both the SL contrast and BW. Two pattern cuts are shown in Fig. 5.30 and Fig. 5.31 which highlights the two SLs that are near 11 dB situated near the ML for  $M = 5$  and 7 respectively. The ML in the figure was filtered out due to the difficulty in seeing the two SLs. The SL contrast is seen to have a recurrent trend, where the peak usually remains near 10-11 dB. This will be explained and elaborated in a discussion at the end of this section.

Regarding the BW, we can see no change over the simulation range. This can again be attributed to the value of  $R_{SA}$  where  $R_{SA} = 133 \mu m$ .

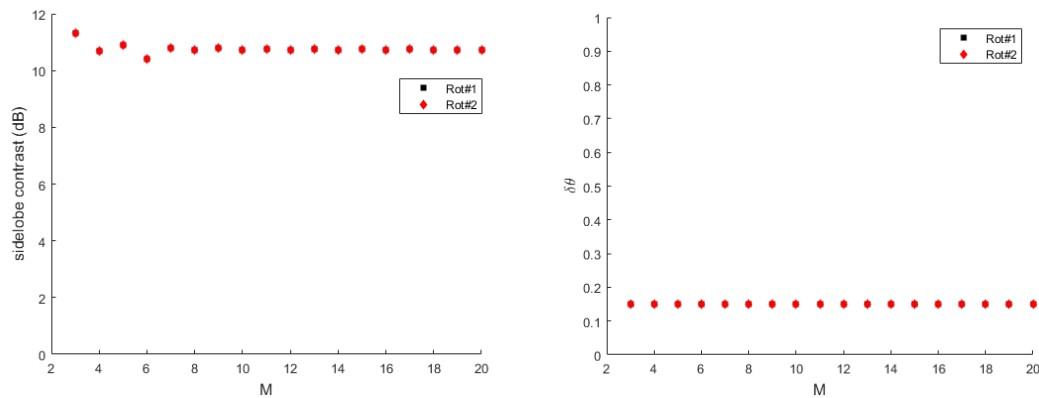


**Figure 5. 29: Impact of  $M$  on the SL contrast and BW**

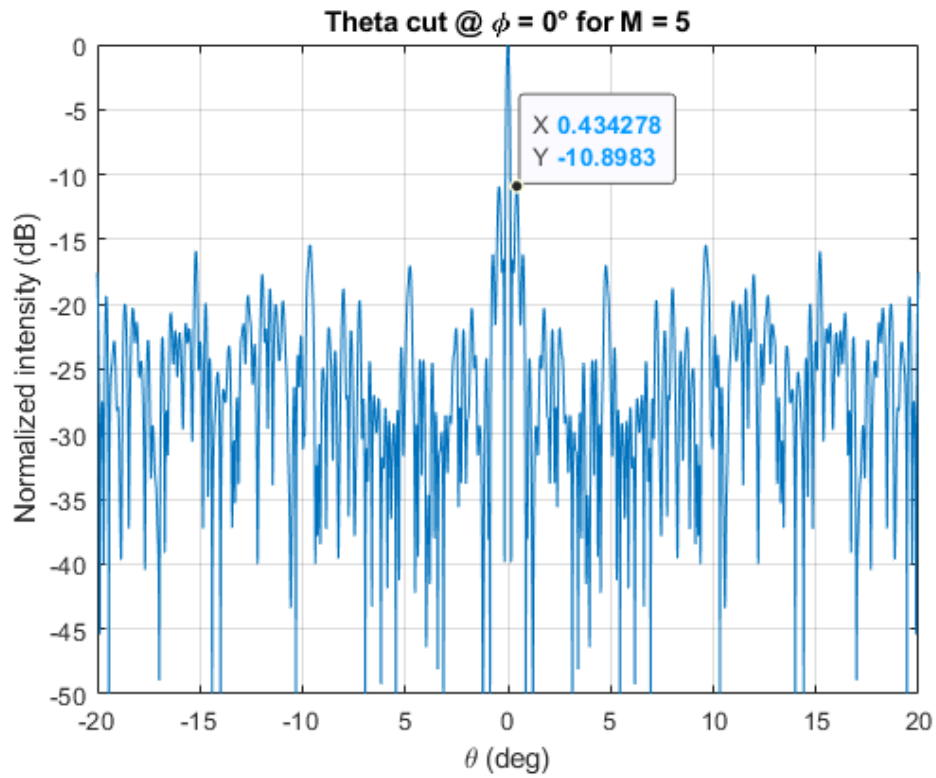


Figure 5. 30: Pattern cut for  $M = 5$

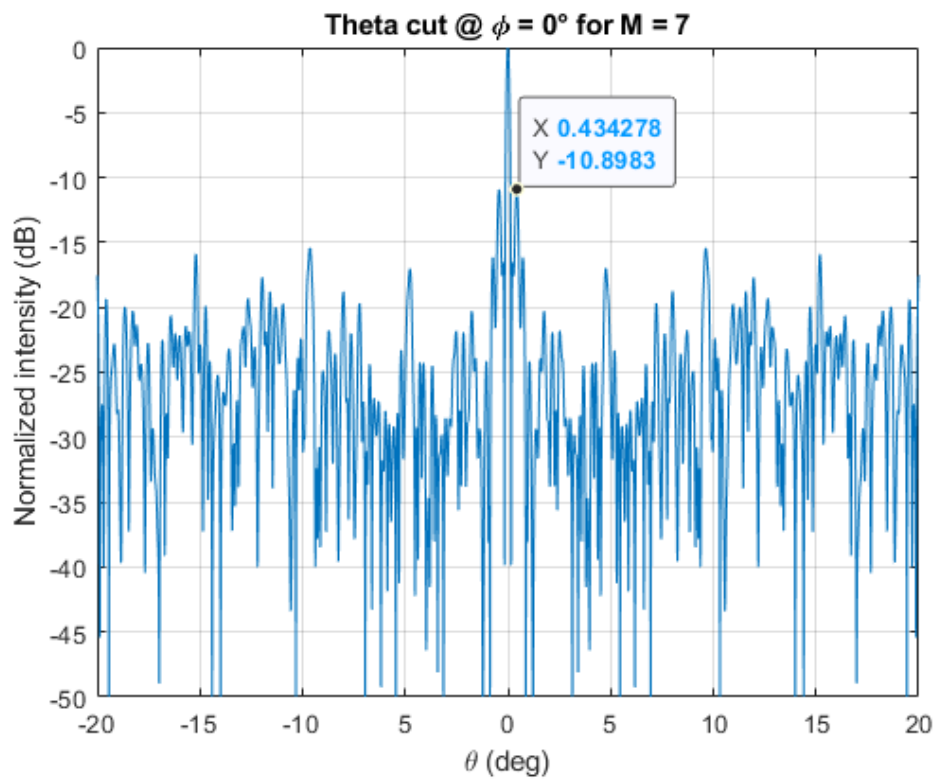
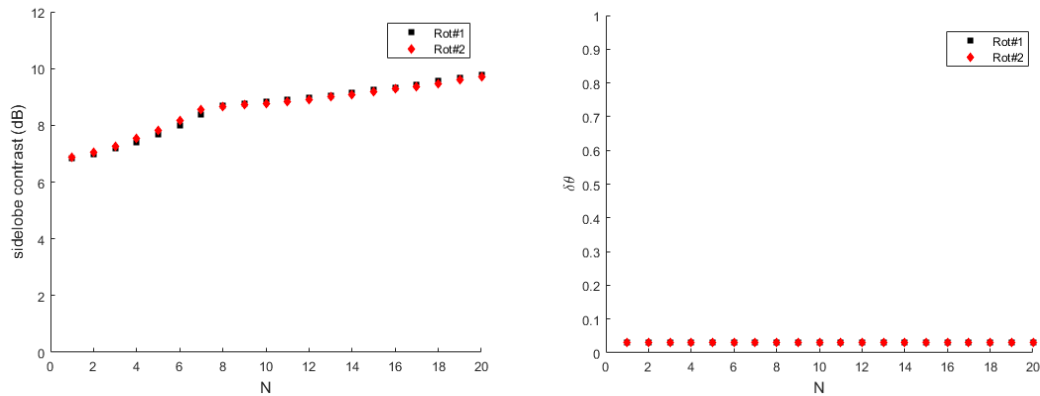


Figure 5. 31: Pattern cut for  $M = 7$

The next parameter of interest is  $N$ , which represents the number of rings within the unit cell. In this study of  $N$ ,  $R_{SA}$  and  $dr_{SA}$  are selected to be  $670 \mu\text{m}$  and  $390 \mu\text{m}$  respectively, which represent the size giving by their respective equations for  $N = 20$ . Increasing  $N$  is seen in Fig. 5.32 to gradually increase the SL contrast, from 7 dB to approximately 9.5 dB. However, increasing  $N$  will increase the number of elements by a factor of  $N$  which dramatically increases the element count. More insight will be given at the end of this section into the large role  $N$  plays in limiting the performance of this design.

The BW sees no change due to the large size of both  $R_{SA}$  and  $dr_{SA}$ .



**Figure 5. 32: Impact of  $N$  on the SL contrast and BW**

The next parameter of interest is  $M_{SA}$ , displayed in Fig. 5.33. Since  $R_{SA}$  depends on  $M_{SA}$ ,  $R_{SA}$  is selected to be  $380 \mu\text{m}$ . It is found that  $M_{SA}$  has a considerable impact on the SL contrast. Up until  $M_{SA} = 11$ , the SL contrast increases steadily where after this point, the trend saturates.

The BW sees no change over most of the simulation range due to  $R_{SA}$ .

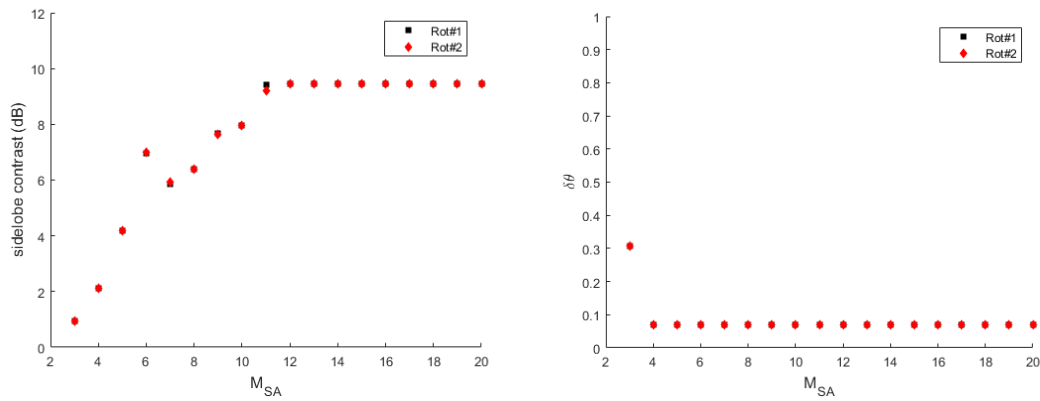


**Figure 5. 33: Impact of  $M_{SA}$  on the SL contrast and BW**

The next parameter of interest is  $N_{SA}$ .  $N_{SA}$  is seen to have a small effect on the SL contrast, only increasing by about 1 dB increase as seen in Fig. 5.34. Again, the small increase in dB can be attributed to the choice in  $M_{SA}$ . We now increase  $M_{SA}$  to 15 and observe the new trend depicted in Fig. 5.35. It can be seen now that the SL contrast sees a large increase over the simulation range due to the increase in  $M_{SA}$ .

The BW sees a little more change in comparison to the past trends which can be attributed to the overall SA radius increasing as the number of SA rings increases.

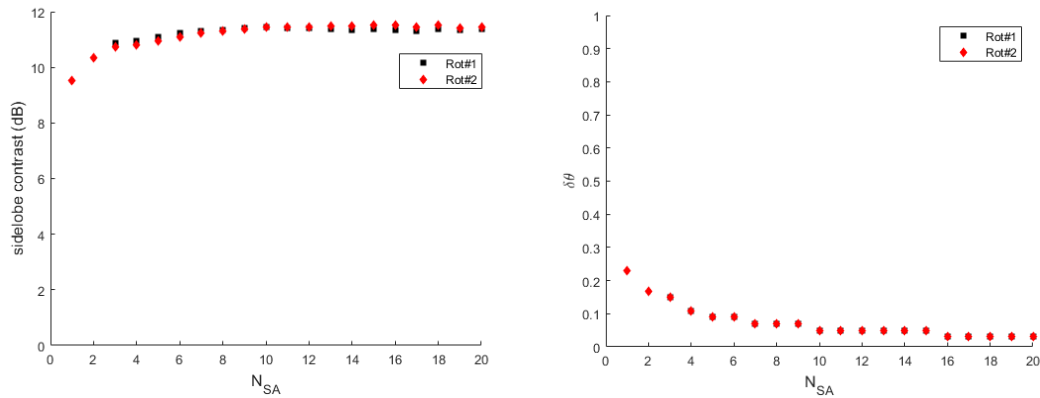


**Figure 5. 34: Impact of  $N_{SA}$  on the SL contrast and BW for  $M_{SA} = 7$**

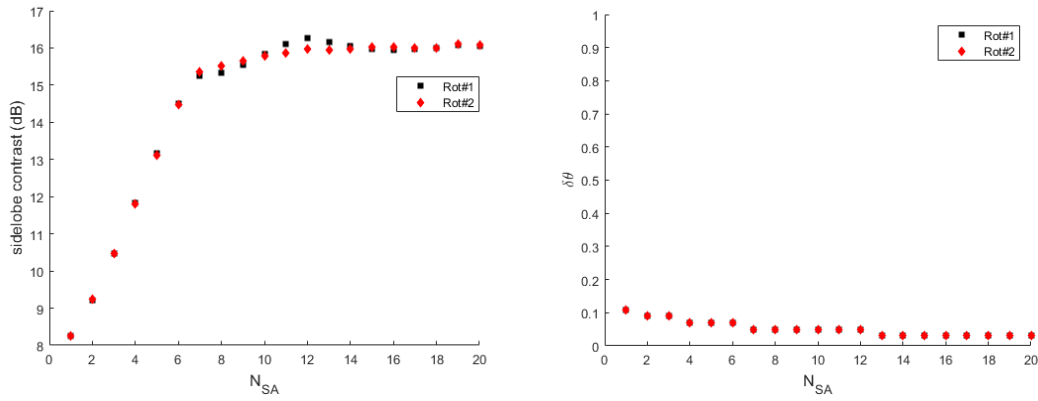


**Figure 5.35: Impact of  $N_{SA}$  on the SL contrast and BW for  $M_{SA} = 15$**

The next parameters of interest are  $R_{unit}$  and  $dr_{unit}$ , the unit cell radius and incremental radius respectively. The trend exhibited by increasing  $R_{unit}$  in Fig. 5.36 demonstrates the large impact imposed by  $R_{unit}$ . The values of  $R_{SA}$  and  $dr_{SA}$  are chosen to be  $415 \mu m$  and  $245 \mu m$ , which represent the size giving by Eq. (5.3) for a  $R_{unit} = 100 \mu m$ . The beamwidth again sees no change over the whole range.

For  $dr_{unit}$ , the trend gradually increases from  $dr_{unit} = 0.5 \mu m$  to  $10 \mu m$  but only by 1 dB as seen in Fig. 5.37. For the study of  $dr_{unit}$ ,  $R_{SA}$  and  $dr_{SA}$  are chosen to be  $140 \mu m$  and  $90 \mu m$ , calculated by making  $dr_{unit} = 10 \mu m$ . Comparing the calculated  $R_{SA}$  and  $dr_{SA}$  between  $R_{unit}$  and  $dr_{unit}$ , it is apparent that the sizes are drastically different ( $415 \mu m$  and  $245 \mu m$  vs.  $140 \mu m$  and  $90 \mu m$ ). This helps demonstrate why the change in  $dr_{unit}$  is less impactful to  $R_{unit}$  and further emphasizes the large control  $R_{SA}$  and  $dr_{SA}$  both have on the SL contrast. And it can be seen again that the beamwidth sees no change over the whole range.

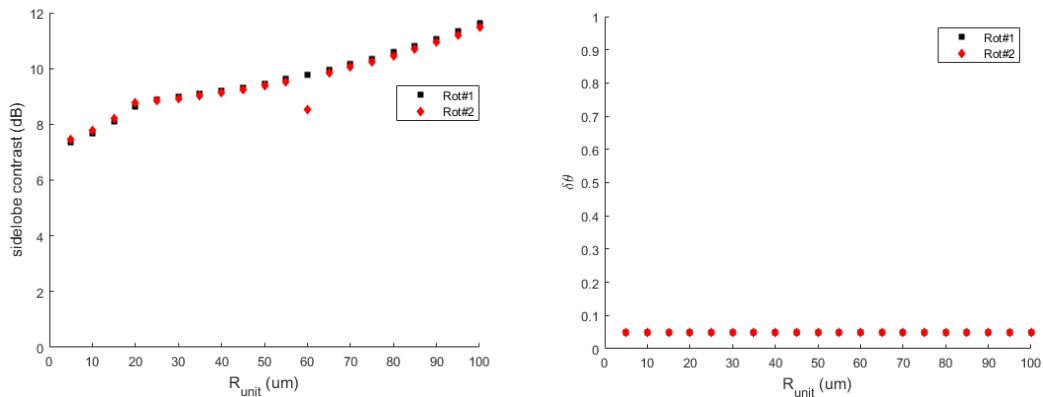


**Figure 5.36: Impact of  $R_{unit}$  on the SL contrast and BW**

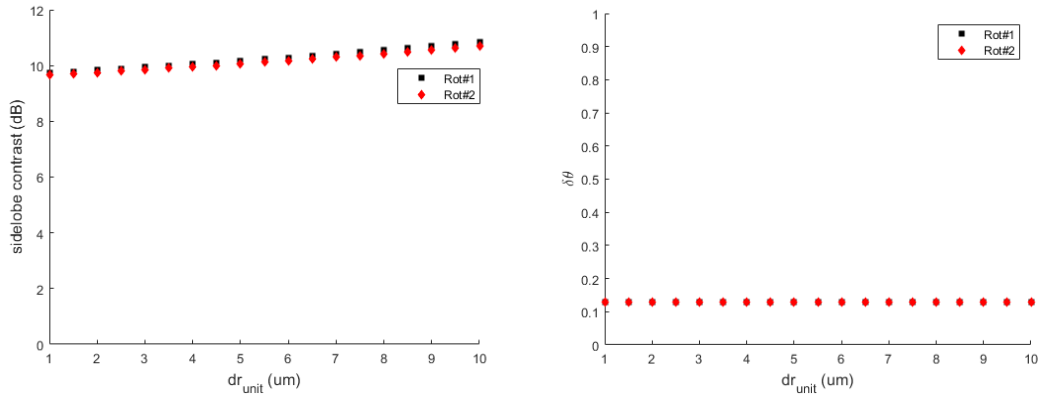


**Figure 5. 37: Impact of  $dr_{unit}$  on the SL contrast and BW**

The last two parameters pertaining to the SA design are  $R_{SA}$  and  $dr_{SA}$ . To start, the trend demonstrated by increasing  $R_{SA}$  is shown in Fig. 5.38. It is immediately understood that the SL contrasts decreases as the size of  $R_{SA}$  increases, which emphasizes the stark contrast between  $R_{SA}$  and all other past design parameters. Understanding the effect of  $R_{SA}$  and any parameters that may have an impact on its size (like  $R_{unit}$  and  $dr_{unit}$  or  $N$ ) should be considered when designing an optimized structure. In the last section, a detailed example explaining the effect of  $R_{SA}$  on the SL contrast will be included.

The beamwidth is seen to have little change over the whole range.

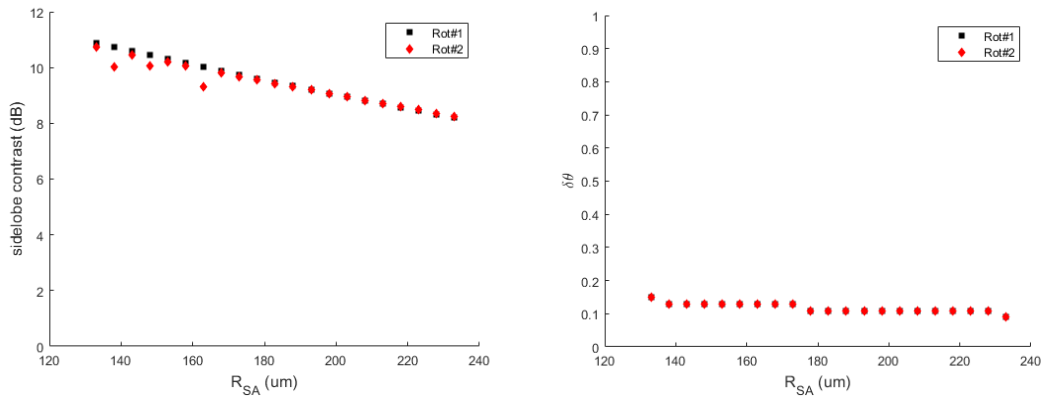


**Figure 5. 38: Impact of  $R_{SA}$  on the SL contrast and BW**

The next parameter of interest is  $dr_{SA}$  where the trends are shown in Fig. 5.39. The SL contrast sees little change until about the half-way point where the trend starts to

decrease. The point where the decrease starts is approximately equal to  $R_{SA}$  at  $130 \mu m$ . Like before in section 5.1.2 in the discussion about  $dr_{SA}$ , we can understand this trend from understanding the effect that the incremental radius has on a single concentric ring array. A similar effect is shared between  $dr_{SA}$  and  $dr$  of the single circular array where the SL contrasts increases until a certain point where after this the SL contrast decreases. However, the additional design parameters introduced with the SA design will create some differences between the effect of  $dr_{SA}$  and  $dr$  in the single circular unit cell and the circular SA structures respectively. We can also see the differences between the impact of  $dr_{SA}$  for the rectangular and circular unit cells where the decrease in dB is more significant for the rectangular unit cell due to the GL distribution with the rectangular unit cell. The properties of the circular array like no GLs greatly differ to the rectangular unit cell which explains the differences.

Little change is seen in the beamwidth over most of the simulation range.

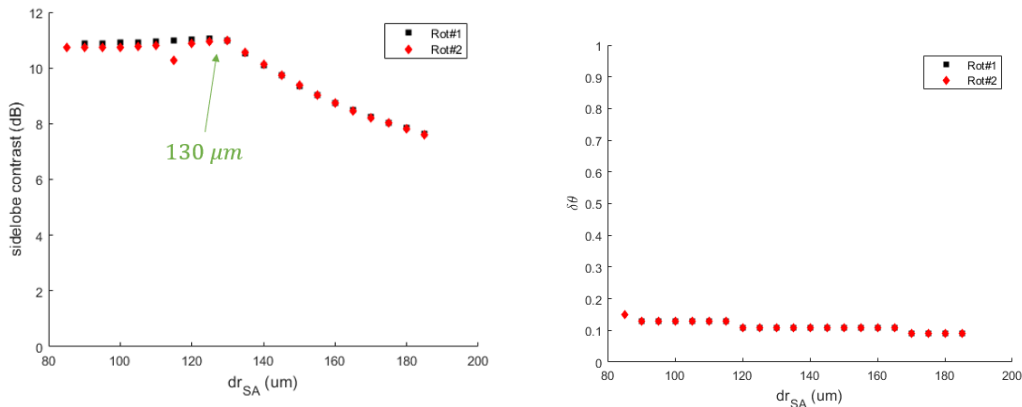


**Figure 5.39: Impact of  $dr_{SA}$  on the SL contrast and BW**

The final parameter of interest is the rotation angle,  $\alpha$ . The trend shows us that the rotation angle largely remains unchanged between  $\alpha = 0^\circ: 90^\circ$ . The affect that  $\alpha$  has on the SL contrast is a lot different with the use of a circular unit cell, largely due to the unique properties like the absence of any GLs. It was very apparent in past designs that utilized rectangular unit and SA lattices that the SL contrast always saw an increase after rotation, due to the elimination of the GLs. But the SL contrast trend shown in Fig. 5.40 demonstrates that  $\alpha$  doesn't have a large role in impacting the SL contrast with a circular unit cell.

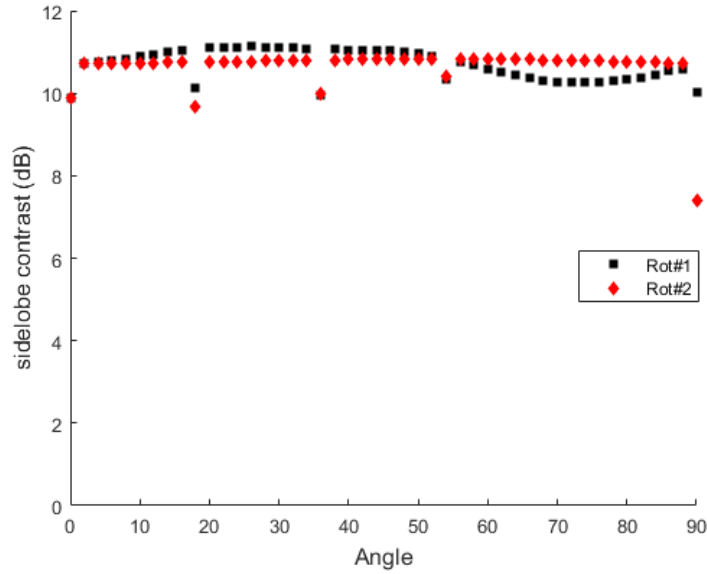


**Figure 5.40: Impact of  $\alpha$  on the SL contrast**

To study the effect of  $\alpha$  further, three values for  $N$  are selected to see if the trend shown in Fig. 5.40 will remain. The selection and variance of  $N$  is chosen primarily for its effect on increasing both  $R_{SA}$  and  $dr_{SA}$ , which have shown to decrease the SL contrast. The rest of the parameters are kept consistent with the previous design introduced at the start of the section. It will be seen that the effect of the rotation angle on the SL contrast drastically changes as  $N$  increases.

Three different graphs are shown in Fig. 5.41, each corresponding to a different value of  $N$ . Graphs a), b) and c) correspond to  $N = 1, 2$  and 3 respectively. Increasing the value of  $N$  drastically changes the affect that the rotation angle has on the SL contrast. Within graph a), the SL contrast fluctuates across the whole spectrum while the other two graphs show a more consistent trend, especially when  $N = 3$ . It is apparent in graph a) that the lowest SL contrast occurs at  $\alpha = 0^\circ$  which is expected from past experiences. The other points across the spectrum for  $N = 1$  can largely be attributed to the circular symmetry possessed by circular unit cells. From the definition of a circular array, the elements are uniformly distributed along the circumference by the following definition

$$\frac{360^\circ}{M} \quad (5.4)$$

So, when the value of  $\alpha = \frac{360^\circ}{M}$ , the circular unit cell will exhibit an identical orientation to that of a unit cell with a  $\alpha = 0^\circ$  rotation angle. In Fig. 5.42, two unit cells are

juxtaposed to demonstrate their identical orientations since the second unit cell has an orientation of  $\alpha = \frac{360^\circ}{M} = \frac{360^\circ}{5} = 72^\circ$ . We can see in graph a) that at  $\alpha = 72^\circ$ , the SL contrast is of the lowest across the whole trend. This can also be seen at angles like  $\alpha = 36^\circ$  where every second unit cell will have an orientation equal to a unit cell with a  $\alpha = 0^\circ$  rotation angle. Unit cells that do not have identical rotations fair a lot better in their performance.

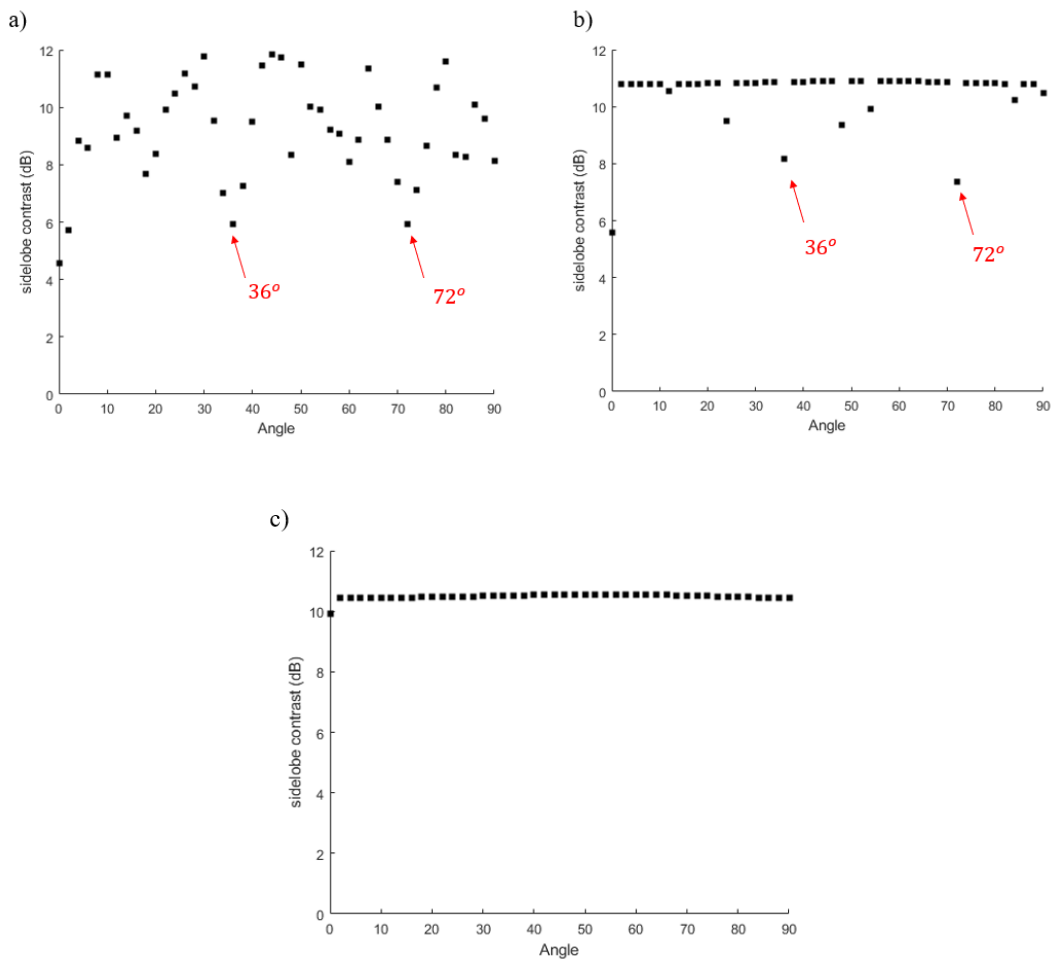


**Figure 5. 41: Impact of  $\alpha$  and  $N$  on the SL contrast where  $N = 1, 2$  and  $3$**

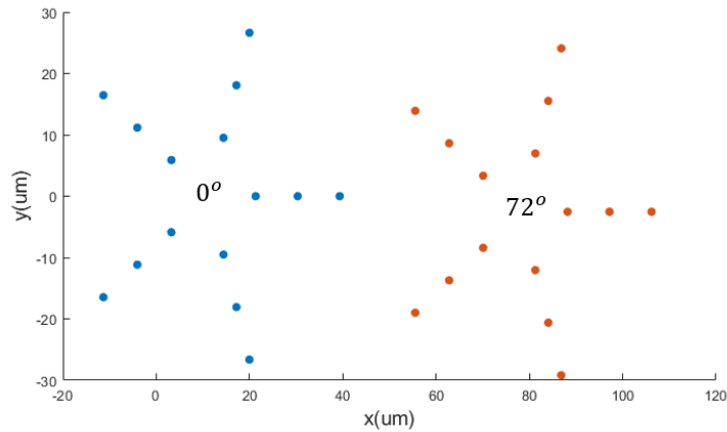


**Figure 5. 42: Identical orientations with  $\alpha = 0^\circ$  and  $72^\circ$**

This trend can still be seen in graph b) at  $\alpha = 36^\circ$  or  $72^\circ$  but the trend largely remains constant near 11 dB. This is especially seen in graph c) where the SL contrast remains constant outside of the first point where  $\alpha = 0^\circ$ . To understand why the trend remains constant, an in depth look at the pattern cuts is done for  $N = 3$  in Fig. 5.43 to 5.45. It is apparent in the pattern cuts that the SL peaks near the ML are unaffected by the rotation angle.

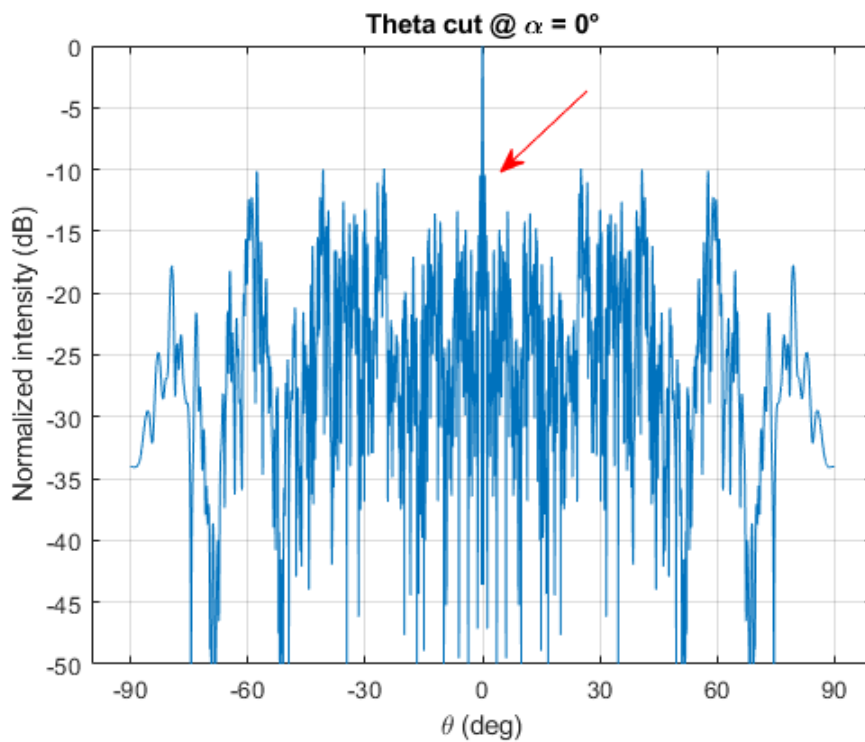


**Figure 5. 43: Pattern cuts for  $N = 3$  @  $\alpha = 0^\circ$**

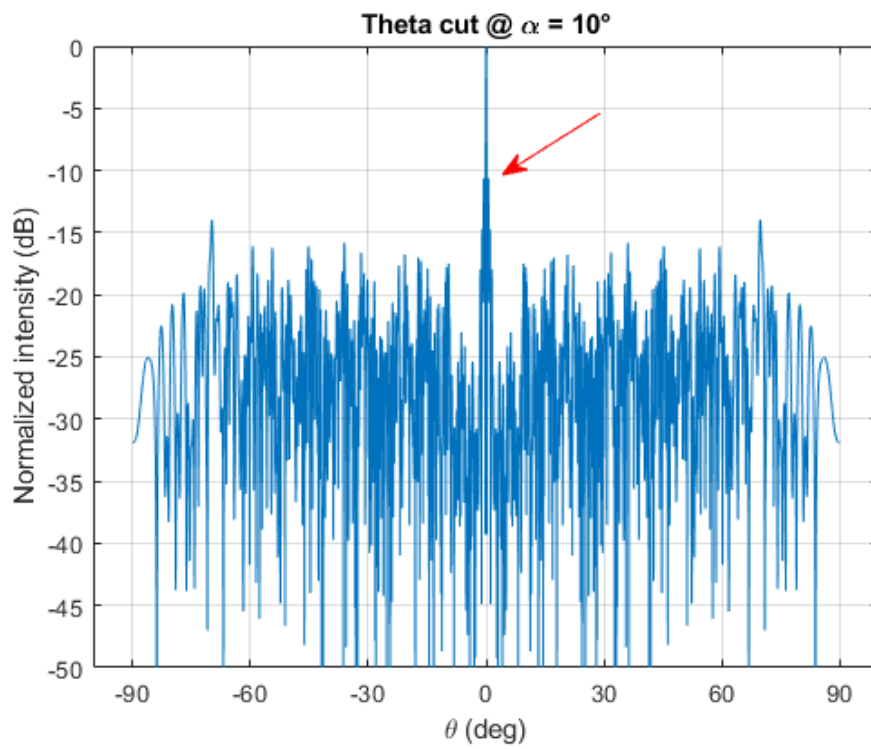


Figure 5. 44: Pattern cuts for  $N = 3 @ \alpha = 10^\circ$

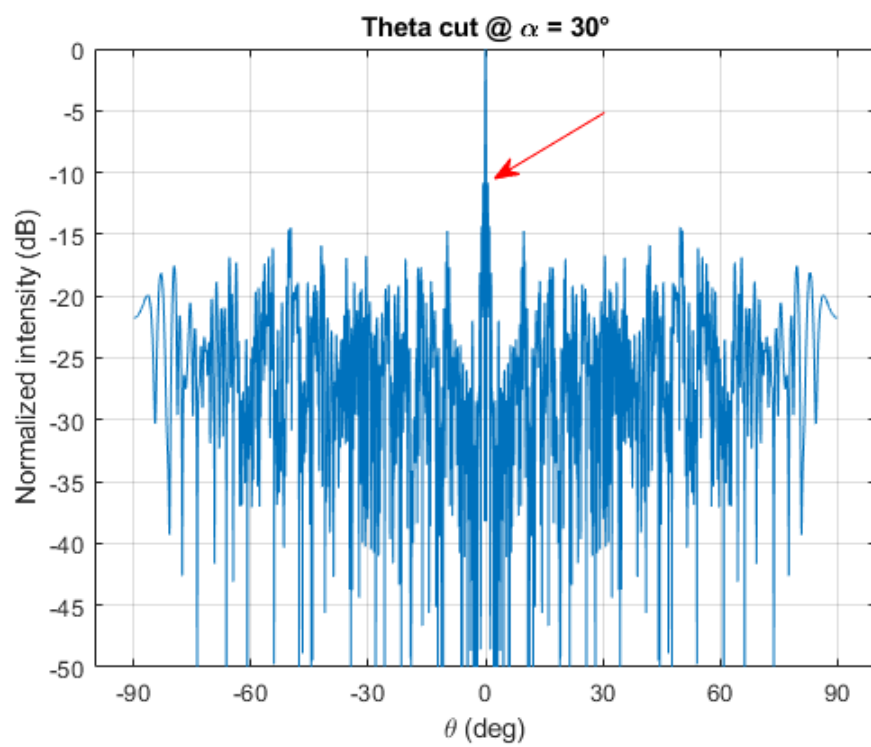
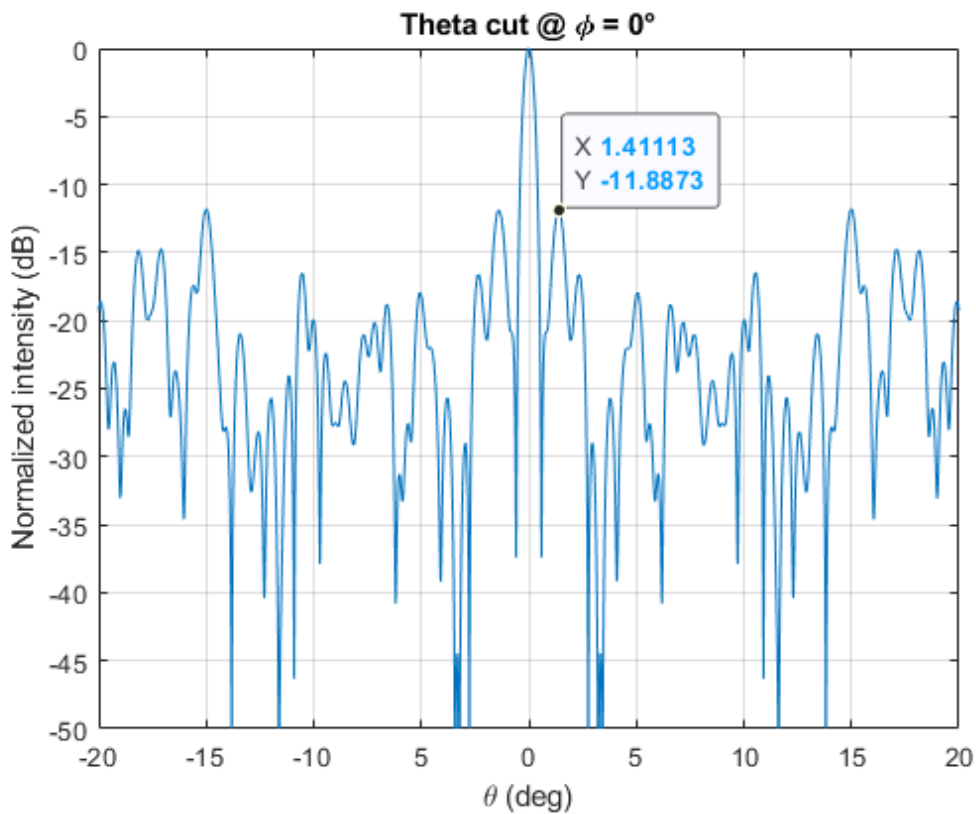
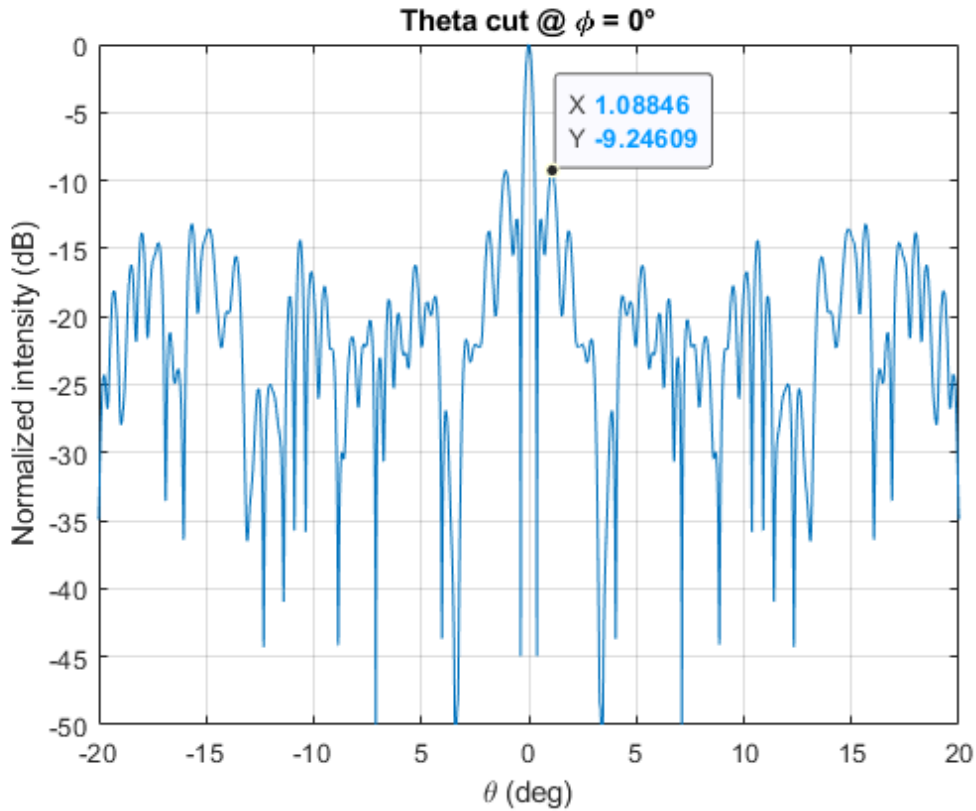


Figure 5. 45: Pattern cuts for  $N = 3 @ \alpha = 30^\circ$

An interesting phenomenon occurs which can be used to explain the cause of these SLs near the ML by demonstrating the relationship between  $N$  and the SA parameters,  $R_{SA}$  and  $dr_{SA}$ .  $R_{SA}$  and  $dr_{SA}$  were shown to decrease the SL contrast as they grew and from the definition in Eq. (5.3) for  $R_{SA}$  and  $dr_{SA}$ , they are dependent on  $N$ . So as  $N$  increases,  $R_{SA}$  and  $dr_{SA}$  must become larger to accompany the larger unit cells to ensure no overlap.  $N$  will always increase the total radius of the structure which poses a design constraint on larger values of  $N$  as it has been shown that  $R_{SA}$  and  $dr_{SA}$  have a larger impact on decreasing the SL contrast. It can be seen in Fig 5.46 and 5.47 how increasing  $R_{SA}$  raises the two SLs near the ML by about 2 dB.



**Figure 5. 46: Pattern cuts for  $R_{SA} = 35 \mu m$**



**Figure 5. 47: Pattern cuts for  $R_{SA} = 65 \mu m$**

The effect of increasing  $R_{SA}$  is similar in principle to a single uniform circular array with an increasing radius. Here, a single ring with an element count of  $M = 11$  is simulated to understand the impact of  $R$ . A trend line depicting the effect on the SL contrast by increasing  $R$  is shown in Fig 5.48. We can see a similar affect shared with the circular unit cell and the circular SA lattices where increasing  $R$  decreases the SL contrast. This effect can be understood from many past studies on the properties of circular arrays [49, 52].

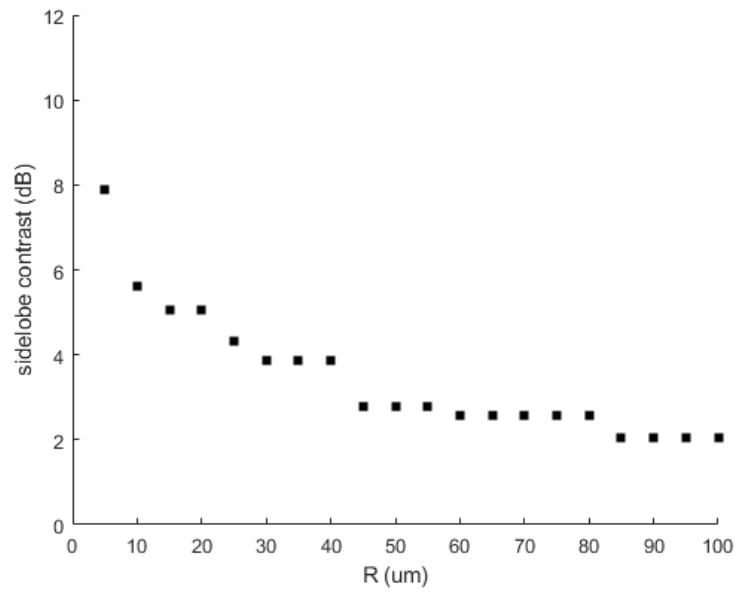


**Figure 5.48: Impact of  $R$  on SL contrast for a single ring array**

This effect can be explained by understanding the principles behind the array factor of a circular array. If we recall from Ch.3, the AF of a uniform circular array was expressed in Eq. (2.18) where the argument of the Bessel function contained  $kR$  ( $J_{nM}(kR)$ ). This means that the beam profile and surrounding radiation pattern is controlled by the radius of the array and not the number of elements. Increasing  $R$  decreases the beamwidth but causes more constructive interference between the principal term ( $n = 0$ ) and the residual terms of the AF, hence why the SL contrasts decreases.

### 5.2.3 Optimizations using the Genetic Algorithm

In the same fashion and for similar reasons as section 5.1.3, we will use the GA to optimize the current structure. This time, we will mimic the chromosomes of the GA now as the circular unit cell parameters,  $M, N, R_{unit}, dr_{unit}$ , the circular SA parameters,  $M_{SA}$  and  $N_{SA}$ , and the rotation angle  $\alpha$ . Now, we will have seven genes for each chromosome within our population. The cost function again will be the calculated SL contrast of the structure using the AF equation. The following ranges for each parameter will be used as a possible choice within each chromosome:

- $M = 3:20$
- $N = 1:10$
- $R_{unit} = 10 \mu m: 30 \mu m$
- $dr_{unit} = 5:15 \mu m$
- $M_{SA} = 3:20$
- $N_{SA} = 1:10$
- $\alpha = 0^\circ:120^\circ$

We keep the unit cell size variation smaller than the SA variation due to our understanding from the simulation results where larger SA parameters improved the SL contrast. The sizes of  $R_{unit}$  and  $dr_{unit}$  start at  $10 \mu m$  and  $5 \mu m$  to ensure there is enough space in a practical device where the element spacing, and routing need to be considered. Finally, the rotation angle varies from  $0:120^\circ$  to reflect the largest possible angle where identical symmetry can be replicated at  $\frac{360^\circ}{M} = \frac{360^\circ}{3} = 120^\circ$ .

We again start with 50 generations for our first run. The cross-over rate is equal to 1 while the mutation rate is equal to 0.1, similarly to before. We also impose a limit to the number of elements per chromosome at 500 elements before starting to calculate the SL contrast of each chromosome. Now we run the GA and see where the convergence lies after 50 generations. We can see in Fig. 5.49 the convergence of the GA lies near 16 dB at the 50<sup>th</sup> generation. This structure that gives this SL contrast has the following configuration:  $M = 3, N = 1, M_{SA} = 15, N_{SA} = 10, R_{unit} = 16 \mu m, dr_{unit} = 8 \mu m$ , and  $\alpha = 26^\circ$ .

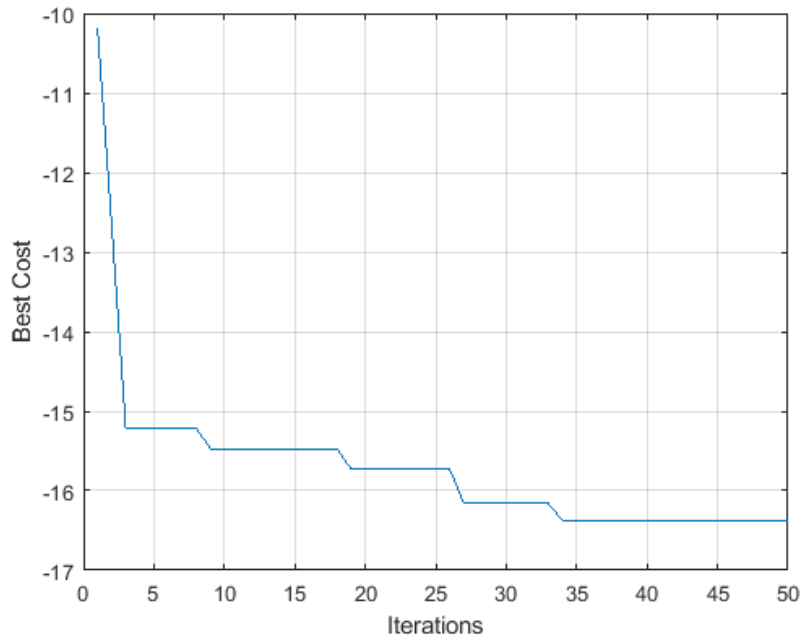


**Figure 5.49: Generation plot for Run 1**

We can already see that the structure with better performance contains a unit cell with  $N = 1$ , matching what we observed within the previous simulation section. However, we do not know if this is the optimal structure within our constraints, so we extend the number of generations to 100. We now simulate the GA with these new changes and observe the convergence results within Fig. 5.50. It is now evident that the convergence lies a little past 17 dB and is met near 50 generations. The structure found has the following configuration:  $M = 3, N = 1, M_{SA} = 19, N_{SA} = 8, R_{unit} = 14 \mu m, dr_{unit} = 13 \mu m$ , and  $\alpha = 79^\circ$ . No improvements in the cost are found after this point which indicate the optimal structure is found.

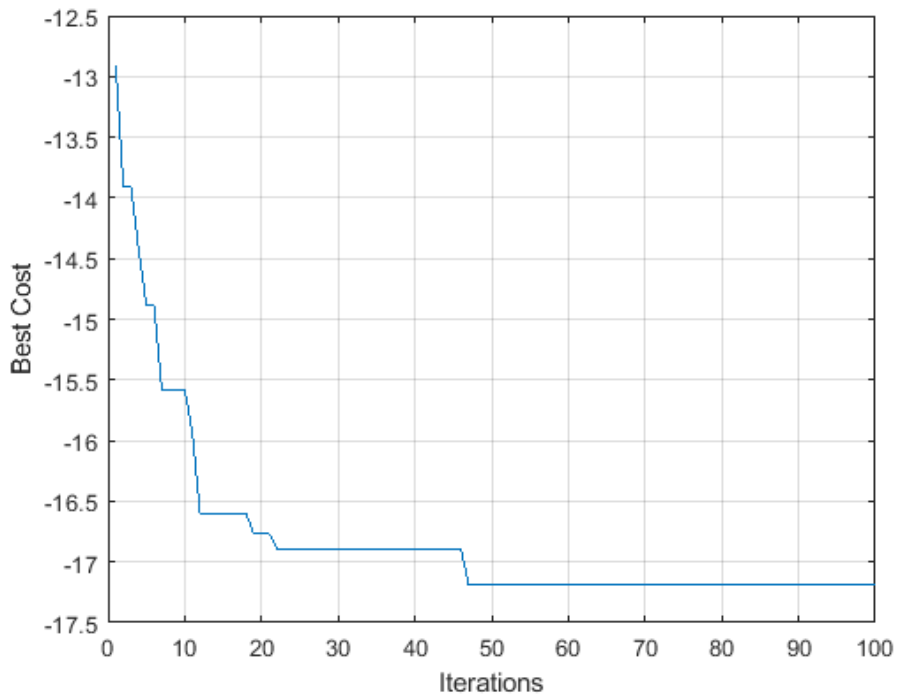


**Figure 5. 50: Second GA run with 100 generations**

We now extend the element threshold to 1000 elements and repeat the same processes as before. The main change we implement is increasing the ranges of the SA parameters  $M_{SA}$  and  $N_{SA}$  to 3:25 and 1:15 respectively in accordance with the larger element threshold. Plotted in Fig. 5.51 is the GAs convergence results for the 1000 element threshold. Increasing the element threshold did allow the GA to find solutions near 19 dB. The structure that reflects this result has the following parameters:  $M = 4, N = 1, M_{SA} = 18, N_{SA} = 11, R_{unit} = 16 \mu m, dr_{unit} = 8 \mu m,$  and  $\alpha = 71^\circ$ .

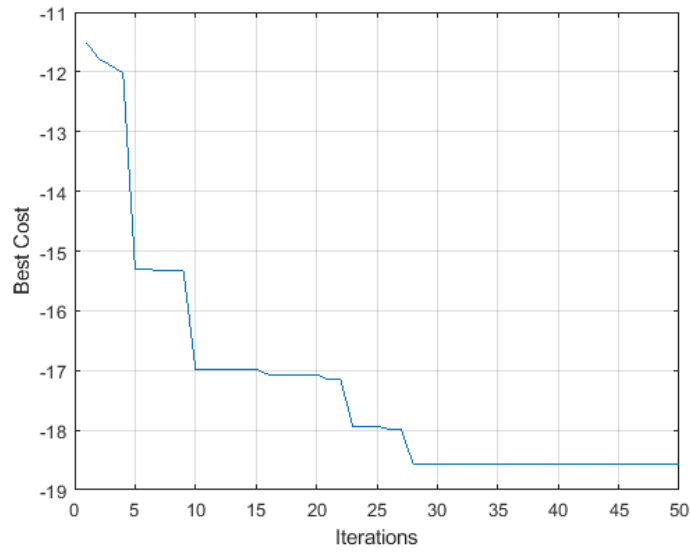


**Figure 5. 51: 1000 element threshold with 50 generations**

The structure previously found may not reflect the best solution yet. Extending the number GA generations to 200 this time can give a better reflection where convergence is met and for how long. The results of these changes are plotted in Fig. 5.52. We can see the best cost is found near 80 generations where no further changes are found for the remaining generations. The structure that gave the best cost has the following parameters:  $M = 3, N = 1, M_{SA} = 22, N_{SA} = 15, R_{unit} = 22 \mu m, dr_{unit} = 14 \mu m,$  and  $\alpha = 53^\circ$ .

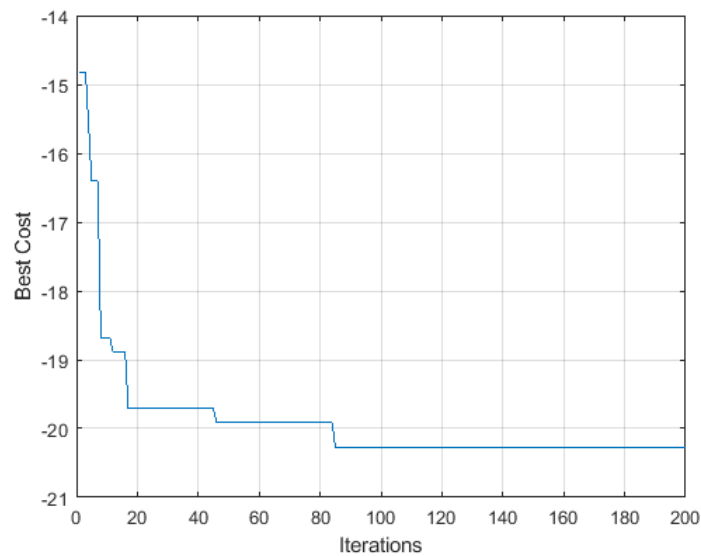


**Figure 5. 52: 1000 element threshold with 100 generations and 50 independent runs**

Yet again, we see that better performing structures contain a unit cell with  $N = 1$ . We can conclude from the optimization process that for this design, a well performing structure should keep  $N = 1$  to not increase  $R_{SA}$  and  $dr_{SA}$ . Likewise, the SA structural parameters  $M_{SA}$  and  $N_{SA}$  should be enlarged since they have the greatest impact on improving the SL contrast as was seen in each structure found at the maximum number of generations.

## 5.3 Optimized structures

### 5.3.1 Rectangular unit cell & Circular SA

Here we demonstrate one of the structures found in the optimization process. We choose the following structure with  $N_r = N_c = 2, M_{SA} = 15, N_{SA} = 8, d_x$  and  $d_y = 7.77 \mu\text{m}$  and  $7.77 \mu\text{m}$ . We can see the array factor plotted in Fig 5.53 within  $uv$  space where  $u = \sin \theta \cos \phi$  and  $v = \sin \theta \sin \phi$  respectively.

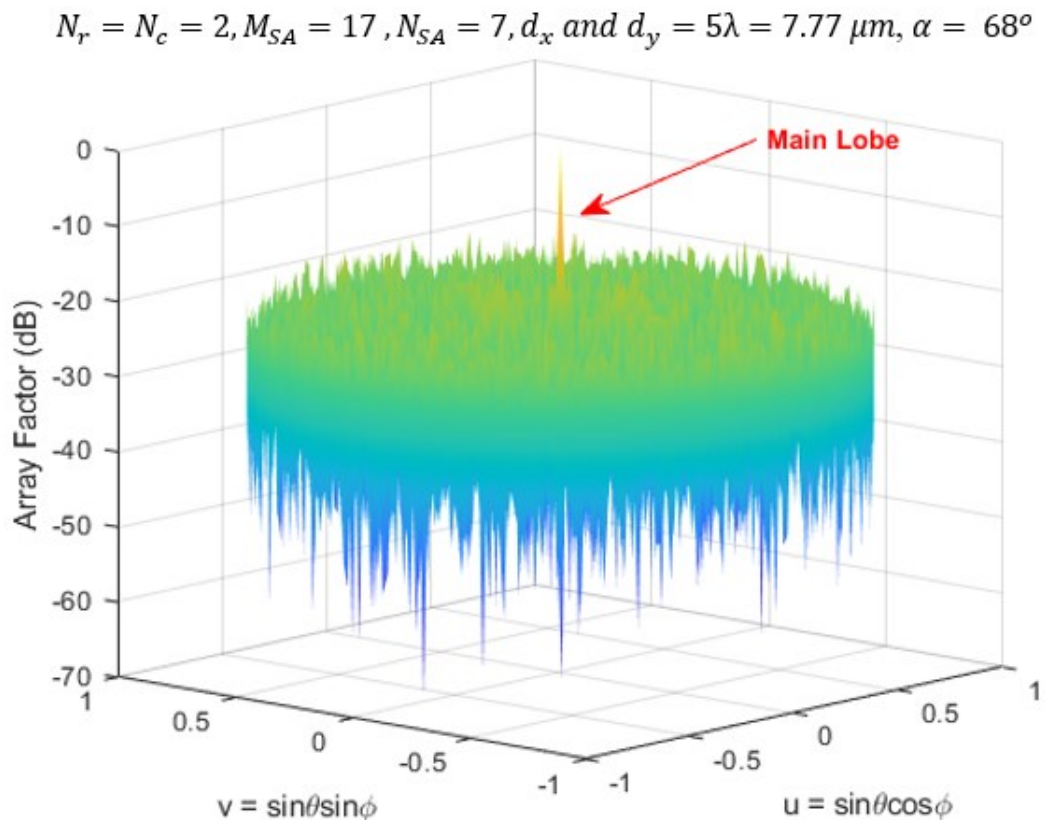


**Figure 5. 53: 3D radiation pattern plotted in  $uv$  space (Rectangular unit cell)**

A robust phased array must demonstrate high resolution beam scanning so we must determine the arrays performance as the beam is steered around the FOV. To understand the beam steering capabilities, we assess the SL contrast and BW as the array is steered. Plotted in Fig. 5.54 are the pattern cuts at various angles of  $\theta$  and we record the results in Table 5.1.

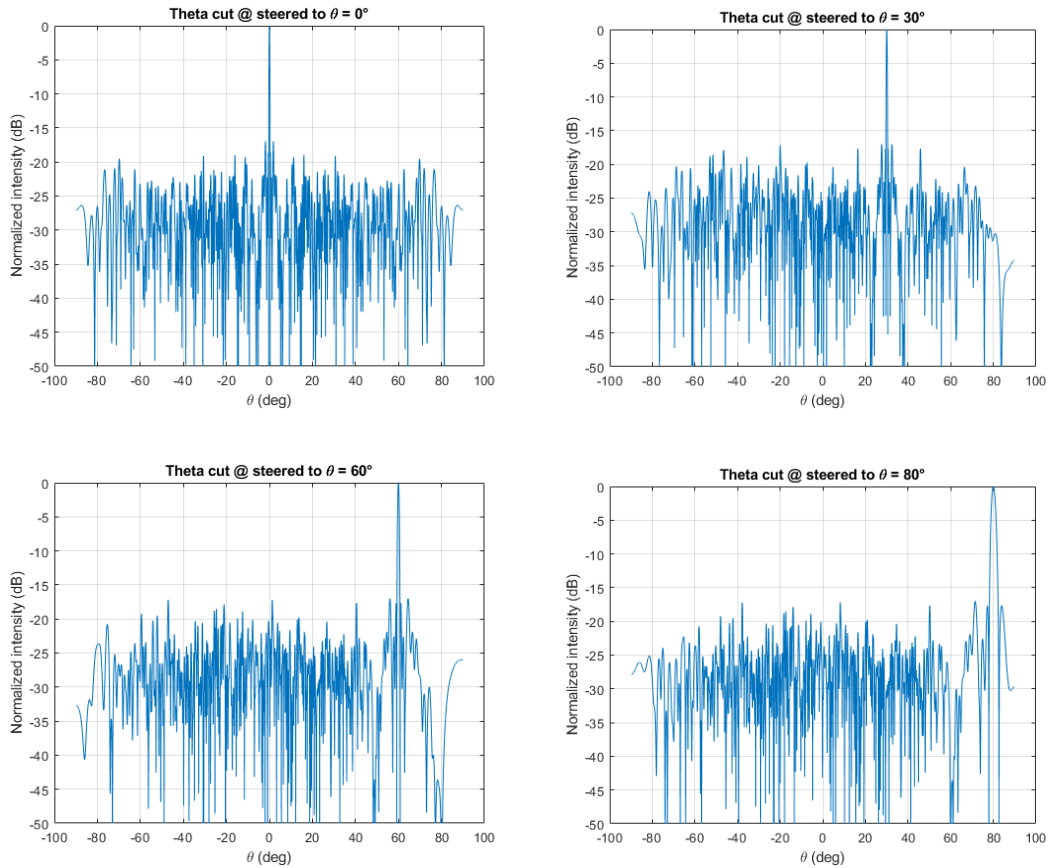


**Figure 5. 54: 2D pattern cuts for  $\theta_0 = 0^\circ, 30^\circ, 60^\circ$  and  $80^\circ$  (Rectangular unit cell)**

**Table 5. 1: Measured SL contrast and BW for varying angles of  $\theta_0$  (Rectangular unit cell)**

$\theta_0$	SL contrast (dB)	BW
$0^\circ$	16.99	$0.34^\circ$
$30^\circ$	16.99	$0.40^\circ$
$60^\circ$	16.99	$0.68^\circ$
$80^\circ$	16.99	$1.94^\circ$

We can see in Table 5.1 that the both the arrays SL contrast and BW is maintained throughout most of the steering range simulated. The ML is still clearly visible with no aliasing occurring over the whole FOV. The BW does see an increase as the steering angle is increased but this can be reduced by increasing the total amount of elements through any of the design parameters or by increasing the unit cell spacing.

### 5.3.2 Circular unit cell & Circular SA

Now we demonstrate one of the structures found in the circular unit cell optimization process. We choose the following structure with  $M = 3, N = 1, M_{SA} = 19, N_{SA} = 8, R_{unit} = 14 \mu m, dr_{unit} = 13 \mu m,$  and  $\alpha = 79^\circ$ . We can see in Fig. 5.55 the simulated array factor belonging to this structure plotted in log scale in the  $uv$  space.

$M = 3, N = 1, M_{SA} = 19, N_{SA} = 8, R_{unit} = 14 \mu m, dr_{unit} = 13 \mu m,$  and  $\alpha = 79^\circ$

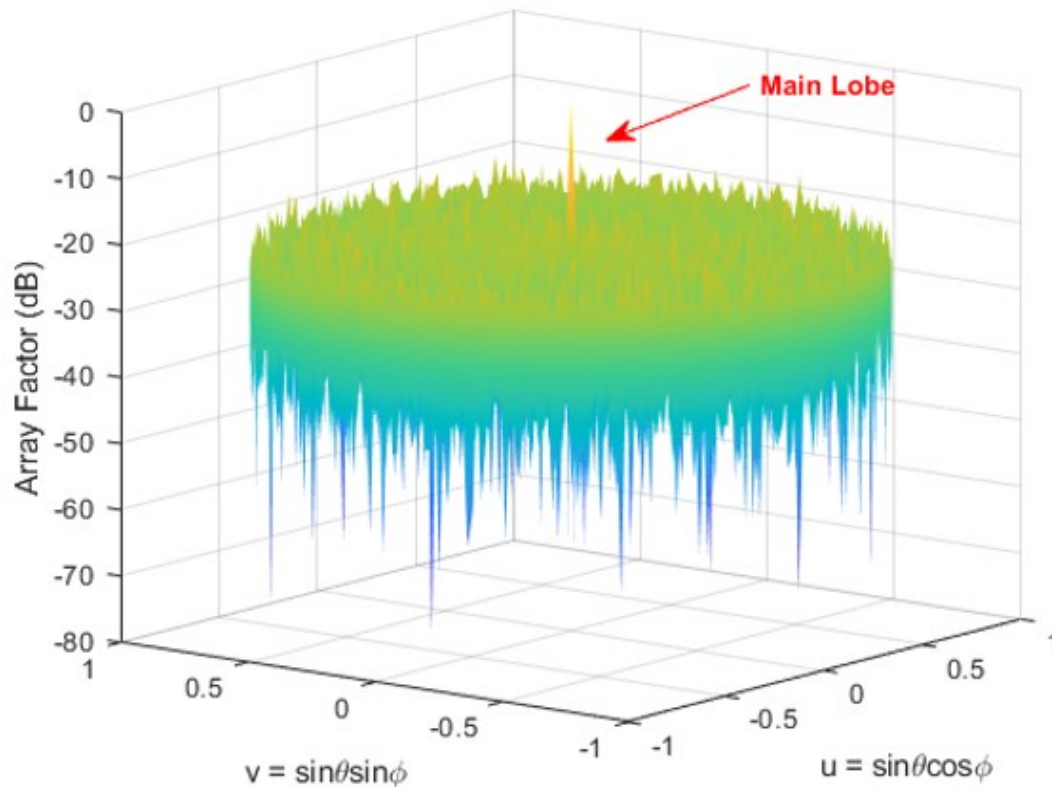
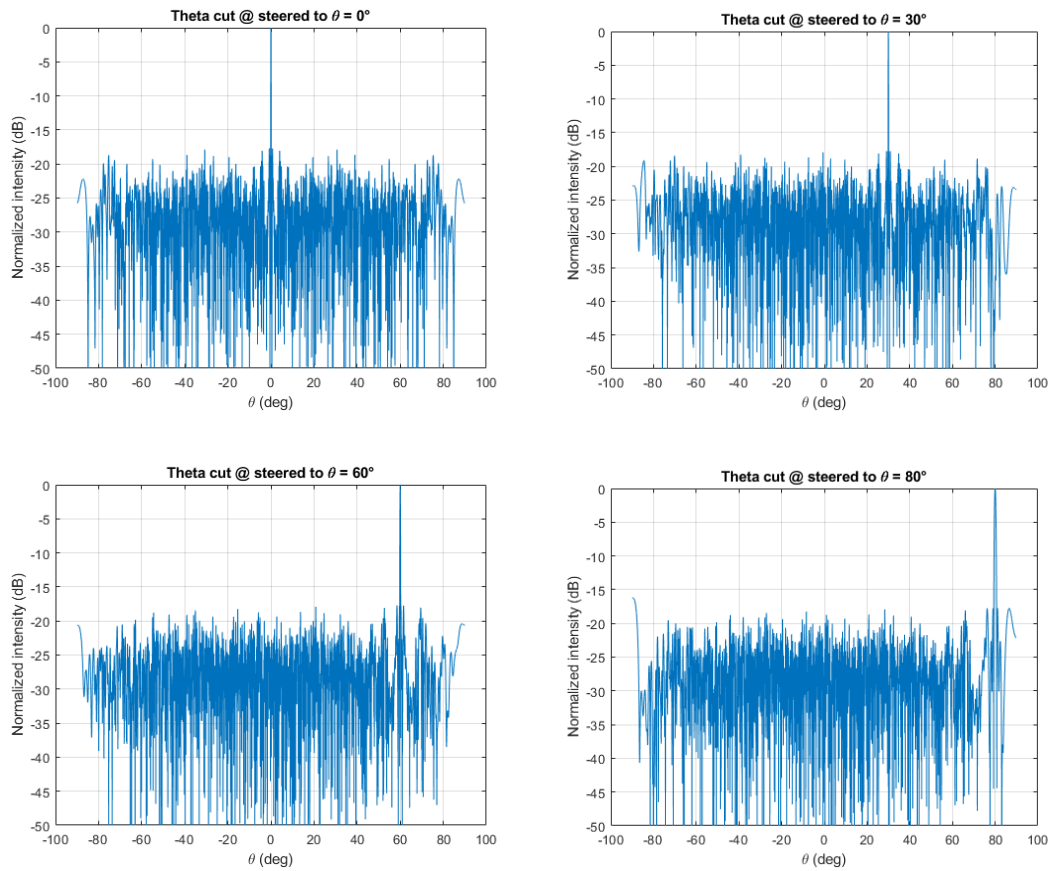


Figure 5. 55: 3D radiation pattern plotted in  $uv$  space (Rectangular unit cell)



**Figure 5. 56: 2D pattern cuts for  $\theta_0 = 0^\circ, 30^\circ, 60^\circ$  and  $80^\circ$  (Circular unit cell)**

We perform the same beam steering tests as before and see how the circular unit cell performs at various angles of  $\theta$ . It's clear from Fig. 5.56 that the beam profile is maintained throughout the whole steering range with no aliasing occurring. The SL contrast is consistent at approximately 17 dB for most angles. We do see a change at  $\theta_0 = 80^\circ$  where the SL contrast = 16.18 dB which is due to the SL emerging near  $\theta_0 = -90^\circ$ . The BW sees no change for each scan angle. This is slightly different than what we saw with the rectangular unit cell which experienced small increases as the ML is steered throughout theta. This is the main difference between the two unit cells is the symmetry possessed by the circular unit cell which allows for angular symmetry along the plane [52]. All the results recorded are within Table 5.2.

**Table 5. 2: Measured SL contrast and BW for varying angles of  $\theta_0$  (Circular unit cell)**

$\theta_0$	SL contrast (dB)	BW
$0^\circ$	17.73	$0.12^\circ$
$30^\circ$	17.75	$0.12^\circ$
$60^\circ$	17.75	$0.12^\circ$
$80^\circ$	16.18	$0.12^\circ$

## 5.4 Uniform Circular Array and Circular SA comparison

We present a comparison between a single circular unit cell and a circular SA design to contrast the performances of each structure. The circular unit cell was detailed within [53] while the circular SA was found using the GA optimization process. The comparison involves both structures having close to 100 elements.

The single circular unit cell has the following configuration:

- $M = 11$
- $N = 10$
- $R_{unit} = 20 \mu m$
- $dr_{unit} = 9 \mu m$

The circular unit cell and circular SA has the following configuration:

- $M = 3$
- $N = 1$
- $M_{SA} = 13$
- $N_{SA} = 3$
- $R_{unit} = 15 \mu m$
- $dr_{unit} = 25 \mu m$
- $\alpha = 38^\circ$

We first start with observing the pattern cuts of each structure and comparing their respective SL contrast and BW. Within Fig. 5.57 are both structures, each with their respective pattern cut. The SL contrast between the two structures are almost the same where the circular unit cell achieved a SL contrast = 11 dB while the circular SA achieved a SL contrast = 12.6 dB. Also, it is apparent that the BW of the circular SA

structure is narrower from the pattern. This occurs as the size of the total structure is larger than the single circular unit cell. The total number of elements is almost equivalent between the two structures so there is not a large discrepancy there (110 elements vs. 117 elements for the circular unit cell and circular SA respectively).

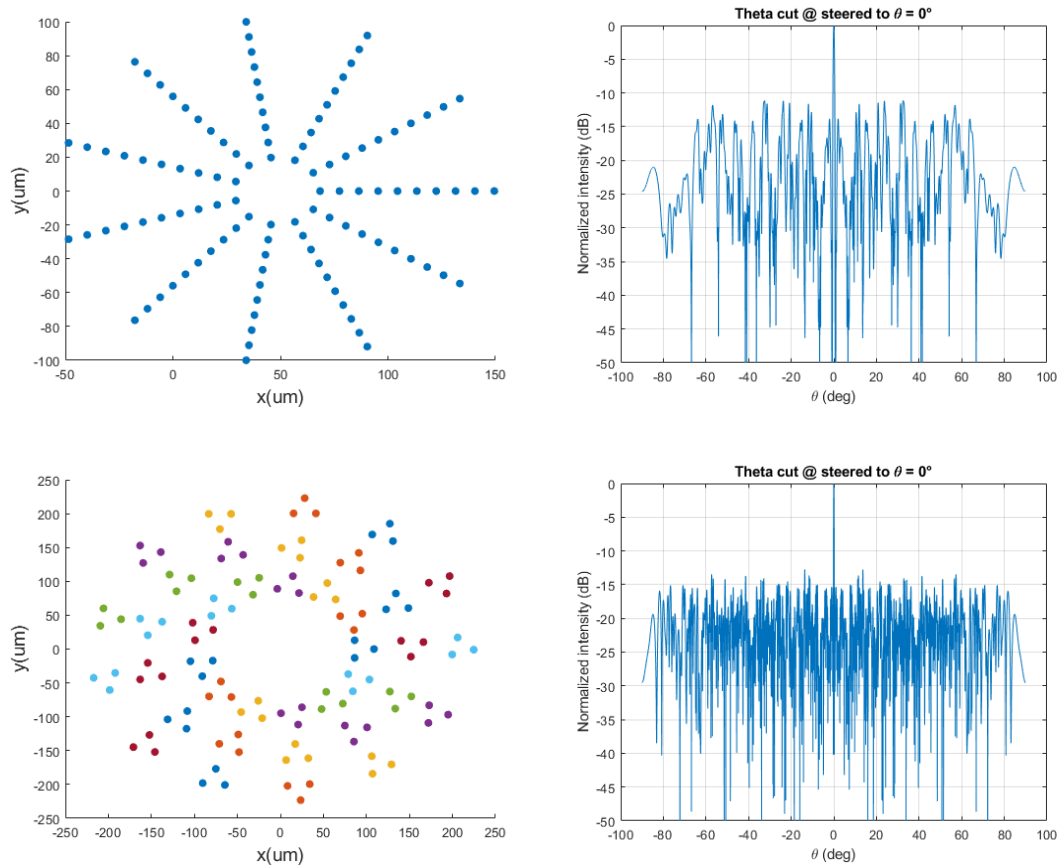


**Figure 5.57: Circular unit and Circular SA with respective pattern cut**

To better compare the performance of each structure, we record the SL contrast and BW while steering the ML. We can see in Table 5.3 that the SL contrast at  $\theta_0 = 0^\circ$  are very close but as we increase  $\theta_0$ , the SL contrast decreases almost by half for the circular unit cell while the circular SA sees little to no change over the whole steering range. We can see how the pattern cuts compare in Fig. 5.58 when the ML is steered to  $\theta_0 = 30^\circ$ . It's clear that the pattern of the circular SA in Fig. 5.58 remains very close to the one we see in Fig. 5.57, but this cannot be said for the circular unit cell. Observing the recorded BW in Table 5.3, we can see that the circular SA BW is more than half the size of the circular unit cell BW which will give the array a much better resolution.

**Table 5. 3: SL contrast and BW performance for circular unit cell and circular SA designs**

$\theta_0$	Circular unit cell		Circular SA	
	SL contrast (dB)	BW	SL contrast (dB)	BW
$0^\circ$	11.1	$0.5^\circ$	12.6	$0.22^\circ$
$30^\circ$	6.6	$0.5^\circ$	12.6	$0.22^\circ$
$60^\circ$	6.4	$0.5^\circ$	12.1	$0.22^\circ$
$80^\circ$	6.4	$0.5^\circ$	12.1	$0.22^\circ$

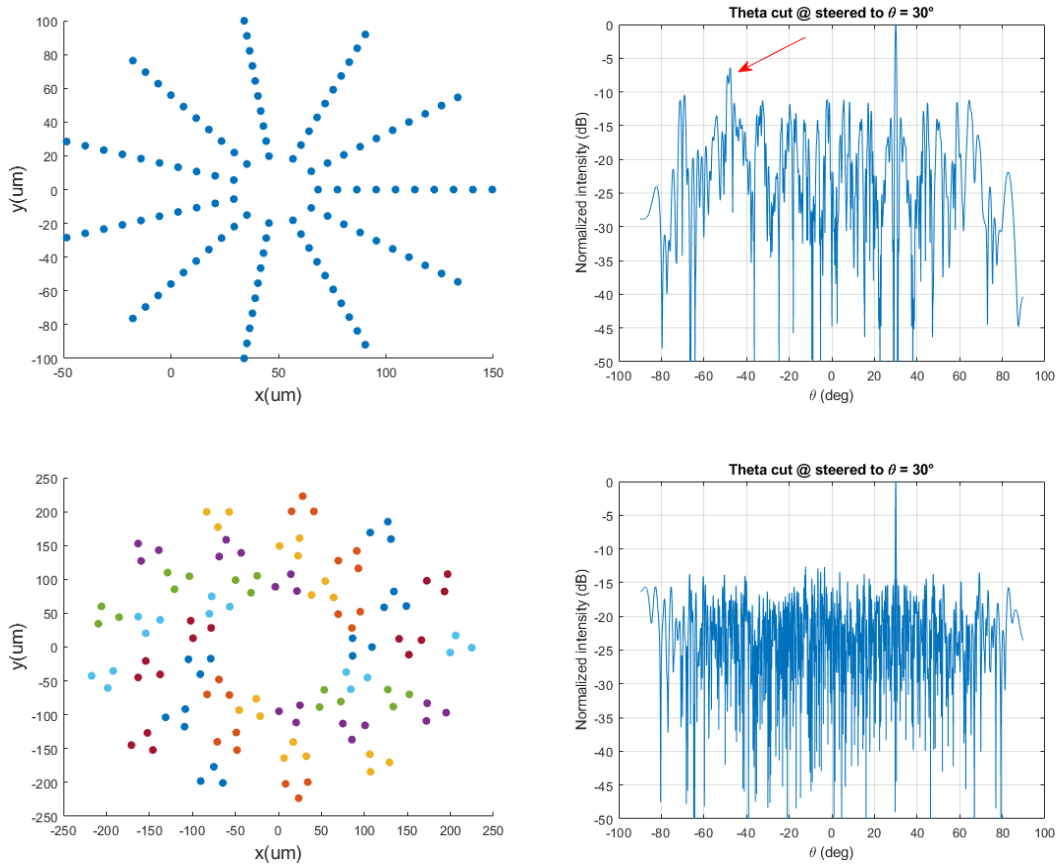


**Figure 5. 58: Pattern cut at  $\theta_0 = 30^\circ$  for circular unit cell and circular SA respectively**

## 5.5 Summary

Within this chapter, we presented two new array arrangements that re-organized the selected unit cell into a circular SA arrangement. We studied the design parameters pertaining to each unit cell/SA combination and understood the effects that increasing each parameter had on the array's performance. We followed this study with the implementation of the GA to optimize the structural parameters of each design, finding where the best solution lies for a 500 element and 1000 element threshold. Both circular SA arrangements achieved a SL suppression close to 17 dB with less than 500 elements. Both arrays also achieved a high angular resolution which can be further improved by increasing the element count or by changing design parameters like the unit cell spacing or the unit cell radius. Finally, we compared a circular unit cell and circular SA by measuring the performance of both structures. We observed that the steering capabilities and BW of the circular SA outperform the circular unit cell while having almost the same number of elements.

## Chapter 6 Conclusions and Future Works

Optical phased arrays are often constricted by spacing constraints which limits the overall performance of the array due to aliasing. This problem has inspired us to look into new methods in array design to improve the performance of the system. In this work, we study new array design methods that can be applicable for OPA designs, particularly to improve the resolution and beam steering capabilities. Meeting higher resolution requirements is crucial for the scanner to recognize objects at longer distances. Two main array designs involving planar arrays and circular arrays were considered for this work. It was shown that larger element spacing's with minimal aliasing can be achieved by reorganizing the array lattice into SAs and applying an appropriate angle of rotation to each SA. Furthermore, even though we are working with a non-uniform array, the design maintains simplicity by keeping the unit cell periodicity intact.

The first array design considered was the planar SA lattice which reorganizes the unit cell of choice along a rectangular or triangular grid. Once the SA lattice is formed, the described rotation method is applied to each unit cell. Both the rectangular and triangular unit cells were considered for comparison discussions. The array performance was examined by changing each design parameter individually to understand the effect each parameter imposes. We saw that large control lies in controlling the parameter's pertaining to the SA to improve performance. We've also seen that larger inter-element spacing's can be achieved without introducing aliasing. The effect on performance while steering was demonstrated to show no aliasing at even large angles of  $\theta$ . We only observed a small change in the BW of the main beam which can be accommodated by elongating the size of the array or introducing more elements. In comparing the two SA lattices, we saw that the triangular SA lattice performed slightly better due to how the lattice impacts the radiation pattern.

The other main work of this thesis was comprised in studying circular SA lattice. We utilized two unit cells in this part, one consisting of a rectangular array and one circular array. Once the unit cell is selected, the circular SA lattice is formed. We also introduced a new method of rotation to contrast with the previous method. When studying the effects of each design parameter of the structure, we discovered that the SA parameters had a much larger impact on the SL contrast and BW. The SA radius and ring radius

both had the largest effect on decreasing the SL contrast so minimizing both while maintaining no overlap is key in achieving better results. The main difference seen between the two unit cells is the effect that the rotation angle had on performance. It is understandable that the rotation angle would have a considerable effect on increasing the SL contrast for a rectangular unit cell by redistributing the GLs over the whole radiation pattern. However, the results we saw from the circular unit cell were very different in contrast to the rectangular unit cell. Due to the symmetrical properties inherent to circular arrays, rotating subsequent unit cells by angles that share identical orientations with previous unit cells lowers the overall SL contrast due to constructive interference. We also saw that incorporating more rings in each unit cell lowers performance due to the increase in the SA radii's which have a much larger impact on performance. The final part of the study again consisted of measuring the performance while steering the main lobe. Both unit cells demonstrated no instance of aliasing while steering. The key difference between the two when steering was noted in the BW. The rectangular unit cell saw a small change over the whole range while the circular unit cell saw no change due to the symmetrical properties of the circular ring.

Comparing the planar and circular SA design, the circular SA was able to achieve both a higher SL contrast and BW with a similar number of elements. This is largely due to the nature of the circular array where GLs are not present due to the symmetrical properties of the circular array. The GLs present in the radiation pattern of the planar array must be re-distributed within the pattern which raises the overall SL contrast. They cannot be eliminated without distributing the periodicity of the SAs. However, introducing non-uniformities to the SA structure will raise the complexity even further.

## 6.1 Future Work

There are things we can build onto the work presented in this thesis. Different approaches can be taken on the planar SA design which can improve the resolution metrics, particularly the SL contrast. In terms of the overall configuration of the structure, we could implement non-uniform spacing within each unit cell and between each SA. We could also use array thinning within each unit cells or even try thinning SAs to achieve lower SLs. We kept the periodicity intact throughout the thesis, but this should be explored to improve performance. However, using these methods will raise the overall complexity of the system which is a comprise if implemented. We could also test using an optimization process if there exists a rotation sequence for all SAs that

improves performance. With regards to array synthesis, there are many techniques that can be implemented to achieve lower SLs. Within our optimization sections, we only considered the use of amplitude tapers but applying a phase taper is another approach to lower SLs. Phase tapers are also simpler to implement because there only needs to be adjustments made to the phase shifters. Finally, we could also attempt null synthesis to cancel the GLs within the array factor of the SA. We relied on the array factor of the unit cells to lower the overall GL power of the SA array factor but taking a more sophisticated approach could lead to better results. Element weights that are purposefully designed to place nulls on the GLs could be a successful method to achieve lower SLs in the final array pattern.

Regarding the circular SA lattice, different optimization schemes can be applied that exploit the symmetry of the array. Optimizing the ring spacing along each SA ring or even the number of unit cells along each ring could improve performance. We could also implement both simultaneously for even larger benefits. This could also be implemented within each unit cell if we use a circular unit cell. And as discussed before, we could implement array thinning within the circular SA by using the genetic algorithm.

Throughout the thesis, the unit cell of choice was kept uniform throughout the whole structure. Rather than keeping the same unit cell, we could use different types of unit cells within the SA lattice such as using rectangular and triangular lattices simultaneously or any planar unit cell with a circular unit cell to see how performance is affected.

## References

- [1] M. Bruel, "Silicon on insulator material technology", *Electron. Lett.* 31 (14), 1201 (1995),
- [2] R. Fatemi, A. Khachaturian and A. Hajimiri, "A Nonuniform Sparse 2-D Large-FOV Optical Phased Array With a Low-Power PWM Drive," in *IEEE Journal of Solid-State Circuits*, vol. 54, no. 5, pp. 1200-1215, May 2019
- [3] Yamada.K.,et.al., "High-performance silicon photonics technology for telecommunications applications", *Science and Technology of Advanced Materials*, vol. 15, no.2, 2014
- [4] Westerveld, W.J., Mahmud-Ul-Hasan, M., Shnaiderman, R. *et al.* Sensitive, small, broadband and scalable optomechanical ultrasound sensor in silicon photonics. *Nat. Photonics* **15**, 341–345 (2021).
- [5] L. R. Chen, et.al., "Recent advances in all-optical signal processing in silicon photonics," in OSA Technical Digest, 2017
- [6] K. V. Acoleyen, W. Bogaerts, J. Jágerská, N. L. Thomas, R. Houdré, and R. Baets, "Off-chip beam steering with a one-dimensional optical phased array on silicon-on-insulator," *Opt. Lett.* 34, 1477–1479 (2009).
- [7] Y. Lin, J. Hyypä and A. Jaakkola, "Mini-UAV-Borne LIDAR for Fine-Scale Mapping," in *IEEE Geoscience and Remote Sensing Letters*, vol. 8, no. 3, pp. 426-430, May 2011
- [8] B. Schwarz, "Lidar: Mapping the world in 3D," *Nat. Photonics*, vol. 4, no. 7, pp. 429–430, 2010
- [9] O.Arteaga, et al., "Initial Investigation of a Low-Cost Automotive LIDAR System", *ISPRS*, vol. 4217, pp. 233–240, 2019.
- [10] B. Behroozpour, P. A. M. Sandborn, M. C. Wu and B. E. Boser, "Lidar System Architectures and Circuits," in *IEEE Communications Magazine*, vol. 55, no. 10, pp.

135-142, Oct. 2017

- [11] G. Fields, "Phased Array Radar At the Intersection of Military and Commercial Innovation," *Microwave J*, vol. 57, (1), pp. 42-42,44, 2014.
- [12] R. A. Meyer, "Optical Beam Steering Using a Multichannel Lithium Tantalate Crystal," *Appl. Opt.* 11, 613-616 (1972)
- [13] Y. Ninomiya, "Ultrahigh resolving electrooptic prism array light deflectors," *IEEE J. Quant. Electron.*, vol. 9, pp. 791-795, Aug. 1973.
- [14] R. M. Matic, "Blazed phase liquid crystal beam steering," *Laser Beam Propagat. and Contr.: Proc. Soc. Photo Opt. Instrum. Eng.*, vol. 2120, pp. 194-205, 1994.
- [15] F. Vasey, F. K. Reinhart, R. Houdr6, and J. M. Stauffer, "Spatial optical beam steering with an AlGaAs integrated phased array," *Appl. Opt.*, vol. 32, pp. 3220-3232, June 1993.
- [16] C. H. Bulmer, W. K. Burns, and T. G. Giallorenzi, "Performance criteria and limitations of electro-optic waveguide array deflectors," *Appl. Opt.* 18, 3282-3295 (1979).
- [17] T. Kim *et al.*, "A Single-Chip Optical Phased Array in a Wafer-Scale Silicon Photonics/CMOS 3D-Integration Platform," in *IEEE Journal of Solid-State Circuits*, vol. 54, no. 11, pp. 3061-3074, Nov. 2019
- [18] Q.Wang, Shuxiao Wang, Lianxi Jia, Yan Cai, Wencheng Yue, and Mingbin Yu, "Increasing wavelength-controlled steering range of an optical phased array by using two subarrays," *Appl. Opt.* 60, 5424-5429 (2021)
- [19] F. Alan et al., "The development of phased-array radar technology," *Lincoln Laboratory J*, 12(2), 320-40, (2000).
- [20] H. Unz, "Linear Arrays with arbitrarily distributed elements," in *IRE Transactions on Antennas and Propagation*, vol. 8, no. 2, pp. 222-223, March 1960

- [21] D.King et.al, "Unequally-spaced, broad-band antenna arrays," in *IRE Transactions on Antennas and Propagation*, vol. 8, no. 4, pp. 380-384, July 1960
- [22] R. Harrington, "Sidelobe reduction by nonuniform element spacing," in *IRE Transactions on Antennas and Propagation*, vol. 9, no. 2, pp. 187-192, March 1961
- [23] M. Andreasen, "Linear arrays with variable interelement spacings," in *IRE Transactions on Antennas and Propagation*, vol. 10, no. 2, pp. 137-143, March 1962
- [24] V. D. Agrawal, "Grating-lobe suppression in phased arrays by subarray rotation," in *Proceedings of the IEEE*, vol. 66, no. 3, pp. 347-349, March 1978
- [25] A. Alshammary, S. Weiss and S. Almorqi, "Grating Lobe Suppression in Rotationally Tiled Arrays," *2017 11th European Conference on Antennas and Propagation (EUCAP)*, 2017
- [26] P. Rocca et.al, "GA-Based Optimization of Irregular Subarray Layouts for Wideband Phased Arrays Design," in *IEEE Antennas and Wireless Propagation Letters*, vol. 14, pp. 131-134, 2015
- [27] Hall et.al, "Sequentially rotated arrays with reduced sidelobe levels", *Electronics Letters*, vol. 28, no. 18, pp. 1761–1763, 1992.
- [28] Y. V. Krivosheev et.al, "Grating lobe suppression in phased arrays composed of identical or similar subarrays," *2010 IEEE International Symposium on Phased Array Systems and Technology*, 2010, pp. 724-730
- [29] Y. V. Krivosheev, A. V. Shishlov and V. V. Denisenko, "Grating Lobe Suppression in Aperiodic Phased Array Antennas Composed of Periodic Subarrays with Large Element Spacing," in *IEEE Antennas and Propagation Magazine*, vol. 57, no. 1, pp. 76-85, Feb. 2015
- [30] K. V. Acoleyen, et.al., "Two-dimensional optical phased array antenna on silicon-on-insulator," *Opt. Express* 18, 13655-13660 (2010)
- [31] J. Sun *et al.*, "Large-Scale Silicon Photonic Circuits for Optical Phased Arrays,"

in *IEEE Journal of Selected Topics in Quantum Electronics*, vol. 20, no. 4, pp. 264-278, July-Aug. 2014, Art no. 8201115, doi: 10.1109/JSTQE.2013.2293316.

[32] Kwong, D., Hosseini, A., Zhang, Y. and Chen, R. T., "1 x 12 unequally spaced waveguide array for actively tuned optical phased array on a silicon nanomembrane." *Appl. Phys. Lett.* 99, 051104 (2011).

[33] David N. Hutchison, Jie Sun, Jonathan K. Doylend, Ranjeet Kumar, John Heck, Woosung Kim, Christopher T. Phare, Avi Feshali, and Haisheng Rong, "High-resolution aliasing-free optical beam steering," *Optica* 3, 887-890 (2016)

[34] Ami Yaacobi, Jie Sun, Michele Moresco, Gerald Leake, Douglas Coolbaugh, and Michael R. Watts, "Integrated phased array for wide-angle beam steering," *Opt. Lett.* 39, 4575-4578 (2014)

[35] Firooz Aflatouni, Behrooz Abiri, Angad Rekhi, and Ali Hajimiri, "Nanophotonic projection system," *Opt. Express* 23, 21012-21022 (2015)

[36] R. Fatemi, A. Khachaturian and A. Hajimiri, "A Nonuniform Sparse 2-D Large-FOV Optical Phased Array With a Low-Power PWM Drive," in *IEEE Journal of Solid-State Circuits*, vol. 54, no. 5, pp. 1200-1215, May 2019

[37] Balanis, C. A. (2005). *Antenna theory: Analysis and design* (3rd ed.). John Wiley.

[38] Hansen, R.C. (1998). *Phased Array Antennas* (2<sup>nd</sup> ed.). John Wiley.

[39] A.J. Zaman, E. Rho, R.Q. Lee, M.L. Zimmerman, "Grating lobe characteristics of a hexagonal array of subarrays", *Antennas and Propagation Society International Symposium 1991. AP-S. Digest*, pp. 1140-1143 vol.2, 1991.

[40] Wei-Yi Xing, Shi-Wei Qu, Shi-Wen Yang, "A Wideband Phased Antenna Array Based on Tapered Cavities in Triangular Lattice Arrangement", *Computational Electromagnetics (ICCEM) 2018 IEEE International Conference on*, pp. 1-3, 2018.

[41] Wen-Man Zou, Shi-Wei Qu, Shiwen Yang, "Wideband Wide-Scanning Phased Array in Triangular Lattice With Electromagnetic Bandgap Structures", *Antennas and*

*Wireless Propagation Letters IEEE*, vol. 18, no. 3, pp. 422-426, 2019.

[42] Ma, M. T. and Walters, Lillie C., (1968), Synthesis of Concentric Ring Antenna Arrays Yielding Approximately Equal Side Lobes, *Radio Science*, 3

[43] R. DuHamel, et al., "Pattern Synthesis for Antenna Arrays on Circular, Elliptical and Spherical Surfaces", 1952

[44] L. Josefsson and P. Persson, *Conformal Array Antenna Theory and Design*. 2006.

[45] J.Wild, "Circular aerial arrays for radio astronomy", *Proc. R. Soc. Lond. A* 262 84–99. 1961

[46] M. T. Ma, *Theory and Application of Antenna Arrays*, Wiley, 1974, Chapter 3, pp. 191– 202.

[47] C. Stearns and A. Stewart, "An investigation of concentric ring antennas with low sidelobes," in *IEEE Transactions on Antennas and Propagation*, vol. 13, no. 6, pp. 856-863, November 1965

[48] Ma, M. T. and L. C. Walters. Synthesis of concentric ring antenna arrays yielding approximately equal sidelobes, *Radio Sci.*, Vol. 3, No.5, pp. 465-470, May, 1968.

[49] Ta-Shing Chu, "On the use of uniform circular arrays to obtain omnidirectional patterns," in *IRE Transactions on Antennas and Propagation*, vol. 7, no. 4, pp. 436-438, October 1959

[50] Bach, H. and J. E. Hansen. Uniformly spaced arrays, Chap. 5 in *Antenna Theory, Part I*, edited by R. E. Collin and Francis J. Zucker, McGraw-Hill Book Company, New York, 1969.

[51] V. Manohar and Y. Rahmat-Samii, "Revisiting the Appearance of Grating Lobes for Antennas With Circular Periodicity," in *IEEE Transactions on Antennas and Propagation*, vol. 67, no. 8, pp. 5723-5728, Aug. 2019

[52] H. L. Knudsen, "The necessary number of elements in a directional ring aerial," *J. Appl. Phys.*, vol. 22, no. 11, pp. 1299–1306, Nov. 1951.

[53] Q. Liu, T. Smy, A. Atieh, P. Cheben and W. N. Ye, "Integrated circular optical phased array with large steering range and high resolution," submitted to *IEEE JSTQE*, Jun 2021.